

DEVELOPMENT OF THREE WAY CATALYTIC CONVERTERS FOR
ELIMINATION OF HYDROCARBONS, CARBON MONOXIDE AND NITRIC
OXIDE IN AUTOMOTIVE EXHAUST

A THESIS SUBMITTED TO
THE GRADUATE SCHOOL OF NATURE AND APPLIED SCIENCES
OF
MIDDLE EAST TECHNICAL UNIVERSITY

BY

AYLİN CİVAN

IN PARTIAL FULFILLMENT OF THE REQUIREMENTS
FOR
THE DEGREE OF MASTER OF SCIENCE
IN
CHEMICAL ENGINEERING

AUGUST 2014

Approval of the Thesis:

**DEVELOPMENT OF THREE WAY CATALYTIC CONVERTERS FOR
ELIMINATION OF HYDROCARBONS, CARBON MONOXIDE AND NITRIC
OXIDE IN AUTOMOTIVE EXHAUST**

submitted by **AYLİN CİVAN** in partial fulfillment of the requirements for the degree of **Master of Science in Chemical Engineering Department, Middle East Technical University** by,

Prof. Dr. Canan Özgen
Dean, Graduate School of **Natural and Applied Sciences**

Prof. Dr. Halil Kalıpçılar
Head of Department, **Chemical Engineering**

Prof. Dr. Işık Önal
Supervisor, **Chemical Engineering Dept, METU**

Examining Committee Members

Prof. Dr. İnci Eroğlu
Chemical Engineering Department, METU

Prof. Dr. Işık Önal
Chemical Engineering Department, METU

Assoc. Prof. Dr. Naime Aslı Sezgi
Chemical Engineering Department, METU

Assoc. Prof. Dr. Erhan Bat
Chemical Engineering Department, METU

Dr. Derya Düzenli
Engineer, General Directorate of Mineral Res.and Explor.

Date : 29.08.2014

I hereby declare that all information in this document has been obtained and presented in accordance with academic rules, and ethical conduct. I also declare that, as required by these rules and conduct, I have fully cited and referenced all material and results that are not original to this work.

Name, Last Name : AYLİN CİVAN

Signature :

ABSTRACT

DEVELOPMENT OF THREE WAY CATALYTIC CONVERTERS FOR ELIMINATION OF HYDROCARBONS, CARBON MONOXIDE AND NITRIC OXIDE IN AUTOMOTIVE EXHAUST

Civan, Aylin

M.Sc., Department of Chemical Engineering

Supervisor: Prof. Dr. Işık Önal

August 2014, 158 pages

In this study, catalytic performances of Three Way Catalysts (TWC) are investigated via Density Functional Theory (DFT) methods and catalytic activity tests in a dynamic test system simulating the exhaust conditions of automobiles. DFT techniques are implemented by Vienna Ab Initio Simulation Package (VASP) and effect of manganese doping in TWC compositions are evaluated with computations on manganese, palladium and rhodium substituted ceria-zirconia mixed oxide (CZO) surface models. Carbon monoxide oxidation mechanisms and energetics are investigated on the model surfaces. Oxygen Storage Capacity (OSC) of CZO is remarkably enhanced by the synergistic effect of Pd and Mn doping. Accordingly, relative energy profile of CO oxidation mechanism on Pd-Mn substituted surface is found to be energetically most favored. Such an efficient collaboration is not observed with Rh and Mn doped CZO. In the

experimental studies, TWC catalysts with varying compositions of Pd, Mn and Rh are synthesized via impregnation and solution combustion methods. Powder catalysts are then mixed with gamma alumina and washcoated on laboratory scale cordierite monoliths. Catalytic activity tests of the monolithic catalysts are carried out in a dynamic activity test system. Online data are simultaneously collected by a Mass Spectrometer (MS) and a CO analyzer coupled to the test system. Performance of the catalysts are evaluated by means of light-off temperatures. Activity results of 28 tests are examined in terms of thermal aging and SO₂ exposure. In compliance with the findings of the computational studies, catalytic performance is improved when Pd is coupled with Mn in catalyst compositions in both synthesis techniques.

Keywords: Three Way Catalyst, Density Functional Theory, Catalytic Activity, Ceria Zirconia Mixed Oxide, Manganese

ÖZ

OTOMOBİL EGSOZUNDAKİ HİDROKARBON, KARBON MONOKSİT VE AZOT OKSİT BİLEŞİKLERİNİN GİDERİLMESİ İÇİN ÜÇ YOLLU KATALİTİK KONVERTERLER GELİŞTİRİLMESİ

Civan, Aylin

Yüksek Lisans, Kimya Mühendisliği Bölümü

Tez Yöneticisi: Prof. Dr. Işık Önal

Ağustos 2014, 158 sayfa

Bu çalışmada, Üç Yollu Katalizörlerin katalitik performansları Yoğunluk Fonksiyoneli Teorisi (DFT) Metodları ve otomobil egsoz koşullarını simüle eden dinamik test sisteminde gerçekleştirilen katalitik aktivite testleri ile incelenmiştir. DFT hesaplamaları Vienna Ab Initio Simulation Package (VASP) yazılımı ile gerçekleştirilmiştir. Üç yollu katalizör kompozisyonlarında mangan metalinin doping etkisini incelemek üzere mangan, paladyum ve rodyum metallerinin atomik olarak seryum-zirkonyum oksit (CZO) yapısına yerleştirilmesiyle model yüzeyler hazırlanmıştır. Bu model yüzeyler üzerinde karbon monoksit oksidasyon mekanizmaları ve enerjileri incelenmiştir. Hesaplamalar sonucu, CZO'nun oksijen depolama kapasitesinin Pd ve Mn metalleri arasındaki sinerjik bir etkileşim sonucu oldukça arttığı gözlemlenmiştir. Bu doğrultuda, Pd-Mn yerleştirilmiş CZO yüzeyi üzerinde gerçekleştirilen CO oksidasyonuna ait rölatif

enerji profili, mekanizmanın enerjetik bakımdan en avantajlı olduđu görülmüştür. Bu denli etkin bir işbirliđi Rh ve Mn yerleştireilmiş yüzeyde gözlemlenmemiştir. Çalışmanın deneysel kısmında, farklı kompozisyonlara sahip Pd, Mn ve Rh içeren katalizörler emdirme ve çözelti yanma sentez yöntemleri kullanılarak sentezlenmiştir. Toz formdaki katalizörler gamma alüminyum oksit ile karıştırılarak kaplama çamuru elde edilmiş ve laboratuvar ölçekli kordierit monolitlere kaplanmıştır. Monolitik katalizörlerin katalitik aktivite testleri dinamik aktivite test sisteminde gerçekleştirilmiştir. Test esnasında çevrimiçi veriler simultane bir biçimde kütle spektrometresi ve CO analizörü tarafından toplanmaktadır. Katalizörlerin performansları termal yaşlandırma ve SO₂ etkisi ile değerlendirilmiştir. Toplam 28 adet teste ait aktivite sonuçları termal yaşlandırma ve SO₂ etkisi ile incelenmiştir. Teorik çalışmalar sonucu elde edilen sonuçlara uyumlu bir şekilde, katalitik performansın, Pd ve Mn metallerini birlikte bulunduran katalizör kompozisyonlarında arttığı iki farklı sentez yöntemiyle sentezlenen katalizörlere ait aktivite sonuçlarıyla görülmüştür.

Anahtar Kelimeler: Üç Yollu Katalizör, Yoğunluk Fonksiyoneli Teorisi, Katalitik Aktivite, Seryum Zirkonyum Karışık Oksit, Mangan

To My Parents

ACKNOWLEDGEMENTS

First of all, I would like to express my most sincere gratitude and appreciation to my supervisor Prof. Dr. Işık Önal for his guidance and encouragements throughout this thesis work.

I would like to thank my former colleague Duygu Gerçeker for sharing her invaluable experience and for all the joyful times we spent together. I am also thankful to İlker Tezsevin for his gracious help and friendship. Also, I would like to thank the past and present members of our research group, Özgen Yalçın, Yasemin Kaya, Miray Gülbiter, Özlem Yönder and Elif Kocaman.

It gives me pleasure to thank Müberra Ayazoğlu, Melike Nur Özbay, Zeynep Çakır, Lütfiye Abanoz and Elif Sızlı for their precious friendship, support and understanding. I would also express my deepest gratitude to Betül Kıran and Dekant Kıran who have always been there for me, not only as my friends but also as the sister and brother that I never had.

My special gratitude goes to Ali Rıza Erdoğan who have always been loving, caring and patient with me. Without him standing by my side, I would not be able to handle the hard times at all.

My parents Sema Civan and Sefer Civan deserve more than I can ever give in return for their all kinds of supports. I owe them so much.

The Scientific and Technological Research Council of Turkey (TÜBİTAK) is also acknowledged for providing financial support to this study with the project 111M777.

TABLE OF CONTENTS

ABSTRACT	v
ÖZ.....	vii
ACKNOWLEDGEMENTS	xi
TABLE OF CONTENTS	xii
LIST OF TABLES	xvi
LIST OF FIGURES.....	xx
LIST OF SYMBOLS	xxv
LIST OF ABBREVIATIONS	xxvi
CHAPTERS	
1. INTRODUCTION.....	1
1.1. Exhaust Emissions	1
1.2. Standards for Exhaust Gas Emissions	2
1.3. Three Way Catalytic Converters.....	3
1.4. Structure and Components of Three Way Catalytic Converters.....	6
1.5. Light-Off Temperature	7
1.6. Deactivation of Three Way Catalysts	8
1.7. Promotion Noble Metal by Base Metals.....	8
1.8. Computational Chemistry.....	8
1.8.1. Density Functional Theory	9
1.9. Objective of the Study	12
2. LITERATURE SURVEY	15
2.1. Three Way Catalyst Preparation.....	15
2.2. Catalytic Activity	17
2.3. Density Functional Studies	19
3. EXPERIMENTAL AND COMPUTATIONAL METHODOLOGY	23
3.1. Experimental Method	23

3.2. Catalyst Preparation.....	23
3.2.1. Catalyst Preparation by Impregnation Method.....	23
3.2.1.1. Preparation of Ceria-Zirconia Support	24
3.2.1.2. Impregnation of Metals on Ceria-Zirconia Support	24
3.4.1. Dynamic Activity Test System.....	28
3.4.2. Catalytic Activity Test Procedure.....	31
3.4.3. Calibrations of Mass Spectrometer.....	32
3.5. Computational Method.....	33
3.5.1. Vienna Ab Initio Simulation Package (VASP)	33
3.2.1. Computational Modelling Procedure	34
4. MODELLING THREE WAY CATALYSTS WITH DFT METHODS	37
4.1. Bulk Structure Optimization.....	37
4.2. Surface Slab Optimization.....	38
4.3. Metal Substitution on Ce _{0.75} Zr _{0.25} O ₂ (110) Surface.....	38
4.4. Modelling of CO Oxidation Mechanism	39
4.4.1. CO Oxidation on (A)-Mn/Ce _{0.75} Zr _{0.25} O ₂ Surface	40
4.4.2. CO Oxidation on (B)-Pd+Mn/Ce _{0.75} Zr _{0.25} O ₂ Surface.....	43
4.4.3. CO Oxidation on (C)-Rh+Mn/Ce _{0.75} Zr _{0.25} O ₂ Surface	48
5. CATALYTIC ACTIVITY TEST RESULTS	53
5.1. Catalysts Synthesized via Impregnation Method	54
5.1.1. Catalytic Activity Tests of IMP1 Catalyst	54
5.1.2. Catalytic Activity Tests of IMP2 Catalyst	57
5.1.3. Catalytic Activity Tests of IMP3 Catalyst	59
5.1.4. Catalytic Activity Tests of IMP4 Catalyst	65
5.1.5. Catalytic Activity Tests of IMP5 Catalyst	69
5.2. Catalysts Synthesized via Solution Combustion Method.....	73
5.2.1. Catalytic Activity Tests of SC1 Catalyst.....	73
5.2.2. Catalytic Activity Tests of SC2 Catalyst.....	76
5.2.3. Catalytic Activity Tests of SC3 Catalyst.....	80
6. CATALYST CHARACTERIZATIONS	87

6.1. ICP-MS Studies	886
6.2. X-ray Diffraction Studies	88
6.3. TEM Characterizations	94
6.4. BET Characterizations	98
7. CONCLUSIONS	99
REFERENCES	103
APPENDICES	
A. SAMPLE VASP SCRIPTS	111
A1. Sample VASP Codes for Bulk Relaxation	111
A1.1. INCAR File.....	111
A1.2. KPOINTS File	112
A1.3. POSCAR File.....	112
A2. Sample VASP Codes for Surface Optimizations.....	113
A2.1. INCAR File.....	113
A2.2. KPOINTS File	113
A2.3. POSCAR File.....	114
A3. Sample VASP Codes for CI-NEB Calculations	116
A3.1. INCAR File.....	116
A3.2. KPOINTS File	117
A4. Sample VASP Codes For Transition State Calculations	117
A4.1. INCAR File.....	117
A4.2. KPOINTS File	117
B. CATALYST PREPARATION	119
B1. Impregnation Method.....	119
B1.1. Preparation of Ceria-Zirconia Mixed Oxide (CZO)	119
B1.2. Impregnation of Metals.....	119
B2. Solution Combustion Method.....	120
B3. Preparation of the Wascoating Slurry	121
B4. Preparation of Pseudoboehmite	122
C. CALCULATIONS FOR CATALYTIC ACTIVITY TEST	123

C.1. Calculation of Total Gas Flow Rate	123
C.2. Simulated Exhaust Gas Composition	123
C.3. Water Content of Simulated Exhaust Gas	127
C.4. Analysis of MAS-SOFT data.....	127
D. CALIBRATIONS FOR MASS SPECTROMETER.....	129
E. CONVERSION VERSUS TEMPERATURE PLOTS OF ACTIVITY	
TESTS.....	137
F. X-RAY DIFFRACTOGRAMS & PARTICLE SIZE ESTIMIZATION	153
F1. XRD Patterns of the Catalysts Synthesized via Impregnation Method	
153	
F2. XRD Patterns of the Catalysts Synthesized via Solution Combustion	
Method.....	156
F3. Particle Size Estimation Using XRD	157

LIST OF TABLES

TABLES

Table 1 Composition of exhaust emissions for diesel and gasoline engines (Martinez-Arias, et al., 2012)	2
Table 2 Emission Standards of California (CARB) since 1993 (Twigg, 2011).....	3
Table 3 Reactions occurring in a Three Way Catalytic Converter (Kaspar, et al., 2003)..	4
Table 4 Labels and compositions of the catalysts synthesized via impregnation method	25
Table 5 Labels and compositions of the catalysts synthesized via solution combustion method.....	26
Table 6 Composition of simulated exhaust gas mixture feed with SO ₂	31
Table 7 Composition of simulated exhaust gas mixture feed without SO ₂	32
Table 8 Change of energies due to atomic substitution on surfaces	39
Table 9 Reaction scheme and relative energies of CO oxidation steps on the surface (A)-Mn/Ce _{0.75} Zr _{0.25} O ₂	40
Table 10 Reaction scheme and relative energies of CO oxidation steps on the surface (B)-Pd+Mn/Ce _{0.75} Zr _{0.25} O ₂	44
Table 11 Reaction scheme and relative energies of CO oxidation steps on the surface (C)-Rh+Mn/Ce _{0.75} Zr _{0.25} O ₂	48
Table 12 Catalytic activity data of IMP1-M2 monolithic catalyst in Test 1 without SO ₂ (Fresh Monolith)	54
Table 13 Catalytic activity data of IMP1-M1 monolithic catalyst in Test 2 without SO ₂ (Monolith aged at 900°C).....	55
Table 14 Catalytic activity data of IMP1-M2 monolithic catalyst in Test 1 with SO ₂ (Fresh Monolith)	56

Table 15 Catalytic activity data of IMP1-M2 monolithic catalyst in Test 2 with SO ₂ (Monolith aged at 900°C)	56
Table 16 Catalytic activity data of IMP2-M1 monolithic catalyst in Test 1 without SO ₂ (Fresh Monolith)	58
Table 17 Catalytic activity data of IMP2-M1 monolithic catalyst in Test 2 without SO ₂ (Monolith Aged at 900°C).....	58
Table 18 Catalytic activity data of IMP3-M1 monolithic catalyst in Test 1 without SO ₂ (Fresh Monolith)	60
Table 19 Catalytic activity data of IMP3-M1 monolithic catalyst in Test 2 without SO ₂ (Monolith Aged 900°C)	61
Table 20 Catalytic activity data of IMP3-M2 monolithic catalyst in Test 1 with SO ₂ (Fresh Monolith)	63
Table 21 Catalytic activity data of IMP3-M2 monolithic catalyst in Test 2 with SO ₂ (Monolith Aged at 900°C).....	63
Table 22 Catalytic activity data of IMP4-M1 monolithic catalyst in Test 1 without SO ₂ (Fresh Monolith)	66
Table 23 Catalytic activity data of IMP4-M1 monolithic catalyst in Test 2 without SO ₂ (Monolith Aged 900°C)	66
Table 24 Catalytic activity data of IMP4-M2 monolithic catalyst in Test 1 with SO ₂ (Fresh Monolith)	68
Table 25 Catalytic activity data of IMP4-M2 monolithic catalyst in Test 2 with SO ₂ (Monolith Aged 900°C)	68
Table 26 Catalytic activity data of IMP5-M1 monolithic catalyst in Test 1 without SO ₂ (Fresh Monolith)	70
Table 27 Catalytic activity data of IMP5-M1 monolithic catalyst in Test 2 without SO ₂ (Monolith Aged at 900°C)	71
Table 28 Catalytic activity data of SC1-M1 monolithic catalyst in Test 1 without SO ₂ (Fresh Monolith)	73
Table 29 Catalytic activity data of SC1-M1 monolithic catalyst in Test 2 without SO ₂ (Monolith aged at 900°C)	74

Table 30 Catalytic activity data of SC1-M2 monolithic catalyst in Test 1 without SO ₂	.75
Table 31 Catalytic activity data of SC1-M2 monolithic catalyst in Test 2 with SO ₂75
Table 32 Catalytic activity data of SC2-M2 monolithic catalyst in Test 1 without SO ₂ (Fresh Monolith)77
Table 33 Catalytic activity data of SC2-M2 monolithic catalyst in Test 2 without SO ₂ (Monolith aged at 900°C)77
Table 34 Catalytic activity data of SC2-M2 monolithic catalyst in Test 1 without SO ₂	.79
Table 35 Catalytic activity data of SC2-M2 monolithic catalyst in Test 2 with SO ₂79
Table 36 Catalytic activity data of SC3-M1 monolithic catalyst in Test 1 without SO ₂ (Fresh Monolith)81
Table 37 Catalytic activity data of SC3-M1 monolithic catalyst in Test 2 without SO ₂ (Monolith aged at 900°C)81
Table 38 Catalytic activity data of SC3-M2 monolithic catalyst in Test 1 without SO ₂	.84
Table 39 Catalytic activity data of SC3-M2 monolithic catalyst in Test 2 with SO ₂84
Table 40 ICP-MS analysis for metal contents of IMP catalysts87
Table 41 ICP-MS analysis for metal contents of SC catalysts88
Table 42 Particle sizes of the fresh and aged catalyst samples calculated based on the cubic ceria peak in XRD patterns94
Table 43 Surface areas of IMP3 and SC3 catalysts for fresh and aged samples98
Table 44 Simulated exhaust gas mixture composition124
Table 45 Compositions of gas cylinders125
Table 46 Gas cylinder flow rates for reducing, stoichiometric and oxidizing conditions126
Table 47 Compositions of simulated exhaust gas mixture for reducing, stoichiometric and oxidizing conditions126
Table 48 MS calibration data for H ₂129
Table 49 MS calibration data for C ₃ H ₆130
Table 50 MS calibration data for C ₃ H ₈131
Table 51 MS calibration data for NO132
Table 52 MS calibration data for SO ₂133

Table 53 MS calibration data for O₂ 134

LIST OF FIGURES

FIGURES

Figure 1 Effect of A/F ratio on conversion of pollutants in three way catalytic converter (Farrauto & Heck, 1999)	5
Figure 2 Control loop of TWC-Engine-Oxygen sensor (Kaspar, et al., 2003)	5
Figure 3 (a) Catalytic converter components (b) Honeycomb structure in a metallic monolith (Kaspar, et al., 2003).....	6
Figure 4 Dynamic activity test system	30
Figure 5 a) Bulk CeO ₂ unit cell b) Periodically repeated CeO ₂ bulk unit cell.....	34
Figure 6 Relaxed bulk unit cells of (a) CeO ₂ (b) Ce _{0.75} Zr _{0.25} O ₂	37
Figure 7 (a) Top and (b) Side view of Ce _{0.75} Zr _{0.25} O ₂ (110) surface	38
Figure 8 Top views of doped surfaces (a) Mn/Ce _{0.75} Zr _{0.25} O ₂ , (b) Mn+Pd/Ce _{0.75} Zr _{0.25} O ₂ and (c) Mn+Rh/Ce _{0.75} Zr _{0.25} O ₂	39
Figure 9 (a) A1 - CO molecule in the gas phase (b) A2 - Adsorbed CO molecule (c) A3 - CO ₂ desorption and creation of an oxygen vacancy	41
Figure 10 (a) A4 - CO ₂ molecule in the gas phase (b) A5 - Approaching gas phase O ₂ molecule (c) A6 - Adsorption of O ₂ on the vacant site	42
Figure 11 (a) A7 - Gas phase CO molecule approaching the surface (b) A8 - CO ₂ desorption from the surface (c) A9 - CO ₂ molecule in the gas phase	42
Figure 12 Relative energy profile of CO oxidation mechanism on (A)-Mn/Ce _{0.75} Zr _{0.25} O ₂ surface	43
Figure 13 (a) B1 - Gas phase CO molecule approaching the surface (b) B2 - CO ₂ desorption from the surface and creation of oxygen defect (c) B3 - CO ₂ molecule in the gas phase	45
Figure 14 (a) B4 - Gas phase O ₂ molecule approaching the surface (b) B5 - Adsorption of O ₂ molecule on the vacant site.....	46

Figure 15 (a) B6 - Gas phase CO molecule approaching the surface (b) B7 - Desorption of CO ₂ molecule from the surface (c) B8 - CO ₂ molecule in the gas phase	46
Figure 16 Relative energy profile of CO oxidation mechanism on (B)-Pd+Mn/Ce _{0.75} Zr _{0.25} O ₂ surface	47
Figure 17 (a) C1 - CO molecule in the gas phase (b) C2 - Adsorbed CO molecule (c) C3 - CO ₂ desorption and creation of an oxygen vacancy	49
Figure 18 (a) C4 - CO ₂ molecule in the gas phase (b) C5 - Gas phase O ₂ molecule approaching the surface (c) C6 - Adsorption of O ₂ molecule on the vacant site	49
Figure 19 (a) C7 - Gas phase CO molecule approaching the surface (b) C8 - Desorption of CO ₂ molecule from the surface (c) C9 - CO ₂ molecule in the gas phase	50
Figure 20 Relative energy profile of CO oxidation mechanism on (C)-Rh+Mn/Ce _{0.75} Zr _{0.25} O ₂ surface	51
Figure 21 Comparison of the CO oxidation mechanisms on (A)-Mn/CZO, (B)-Pd+Mn/CZO and (C)-Rh+Mn/CZO.....	52
Figure 22 Change in T50 values for IMP1-M1 monolithic catalyst upon Thermal Aging (Tests with no SO ₂).....	55
Figure 23 Change in T50 values for IMP1-M1 monolithic catalyst upon Thermal Aging (Tests with SO ₂)	57
Figure 24 Change in T50 values for IMP2-M1 monolithic catalyst upon Thermal Aging (Tests with no SO ₂).....	59
Figure 25 Change in T50 values for IMP3-M1 monolithic catalyst upon Thermal Aging (Tests with no SO ₂).....	61
Figure 26 Comparison of T50 values of IMP1 and IMP3 monolithic catalysts with thermal aging effect (Tests with no SO ₂).....	62
Figure 27 Change in T50 values for IMP3-M2 monolithic catalyst upon Thermal Aging (Tests with SO ₂)	64
Figure 28 Comparison of T50 values of IMP1 and IMP3 monolithic catalysts with thermal aging effect (Tests with SO ₂).....	65
Figure 29 Change in T50 values for IMP4-M1 monolithic catalyst upon Thermal Aging (Tests with no SO ₂).....	67

Figure 30 Change in T50 values for IMP4-M2 monolithic catalyst upon Thermal Aging (Tests with SO ₂)	69
Figure 31 Change in T50 values for IMP5-M1 monolithic catalyst upon Thermal Aging (Tests with no SO ₂)	71
Figure 32 Comparison of T50 values of IMP4 and IMP5 monolithic catalysts with thermal aging effect (Tests with no SO ₂)	72
Figure 33 Change in T50 values for SC1-M1 monolithic catalyst upon Thermal Aging	74
Figure 34 Change in T50 values for SC1-M2 monolithic catalyst upon SO ₂ exposure...	76
Figure 35 Change in T50 values for SC1-M1 monolithic catalyst upon Thermal Aging	78
Figure 36 Change in T50 values for SC2-M2 monolithic catalyst upon SO ₂ exposure...	80
Figure 37 Change in T50 values for SC3-M1 monolithic catalyst upon Thermal Aging	82
Figure 38 Comparison of T50 values of SC1 and SC3 monolithic catalysts with thermal aging effect (Tests with no SO ₂)	83
Figure 39 Change in T50 values for SC3-M2 monolithic catalyst upon SO ₂ exposure...	84
Figure 40 Comparison of T50 values of SC1 and SC3 monolithic catalysts with the effect of SO ₂ exposure.....	85
Figure 41 X-ray diffractogram of the fresh Ce _{0.8} Zr _{0.2} O ₂ powder.....	89
Figure 42 XRD of a) Ce _{0.8} Zr _{0.2} O ₂ fresh powder b) Catalyst IMP1 fresh powder	90
Figure 43 XRD of a) Ce _{0.8} Zr _{0.2} O ₂ fresh powder b) Catalyst IMP2 fresh powder	91
Figure 44 XRD of a) Ce _{0.8} Zr _{0.2} O ₂ fresh powder b) Catalyst SC1 fresh powder	92
Figure 45 XRD of a) Fresh IMP1 powder b) IMP1 powder aged at 900°C	93
Figure 46 HRTEM images of the fresh IMP3 catalyst powder.....	95
Figure 47 HRTEM images of the fresh SC3 catalyst powder.....	96
Figure 48 EDX analysis of different regions on SC3 catalyst sample	97
Figure 63 MS calibration plot for H ₂	130
Figure 64 MS calibration plot for C ₃ H ₆	131
Figure 65 MS calibration plot for C ₃ H ₆	132
Figure 66 MS calibration plot for NO.....	133
Figure 67 MS calibration plot for SO ₂	134
Figure 68 MS calibration plot for O ₂	135

Figure 49 Conversion versus temperature curves of IMP1-M1 in thermal aging (no SO ₂)	138
Figure 50 Conversion versus temperature curves of IMP1-M2 in thermal aging (with SO ₂)	139
Figure 51 Conversion versus temperature curves of IMP2-M1 in thermal aging (no SO ₂)	140
Figure 52 Conversion versus temperature curves of IMP3-M1 in thermal aging (no SO ₂)	141
Figure 53 Conversion versus temperature curves of IMP3-M2 in thermal aging (with SO ₂)	142
Figure 54 Conversion versus temperature curves of IMP4-M1 in thermal aging (no SO ₂)	143
Figure 55 Conversion versus temperature curves of IMP4-M2 in thermal aging (with SO ₂)	144
Figure 56 Conversion versus temperature curves of IMP5-M1 in thermal aging (no SO ₂)	145
Figure 57 Conversion versus temperature curves of SC1-M1 in thermal aging (no SO ₂)	146
Figure 58 Conversion versus temperature curves of SC1-M2 in SO ₂ exposure	147
Figure 59 Conversion versus temperature curves of SC2-M1 in thermal aging (no SO ₂)	148
Figure 60 Conversion versus temperature curves of SC2-M2 in SO ₂ exposure	149
Figure 61 Conversion versus temperature curves of SC3-M1 in thermal aging (no SO ₂)	150
Figure 62 Conversion versus temperature curves of SC3-M2 in SO ₂ exposure	151
Figure 69 XRD of a) Fresh IMP1 powder b) IMP1 powder aged at 900°C	153
Figure 70 XRD of a) Fresh IMP2 powder b) IMP2 powder aged at 900°C	154
Figure 71 XRD of a) Fresh IMP3 powder b) IMP3 powder aged at 900°C	154
Figure 72 XRD of a) Fresh IMP4 powder b) IMP4 powder aged at 900°C	155
Figure 73 XRD of a) Fresh IMP5 powder b) IMP5 powder aged at 900°C	155

Figure 74 XRD of a) Fresh SC1 powder b) SC1 powder aged at 900°C156
Figure 75 XRD of a) Fresh SC2 powder b) SC2 powder aged at 900°C156
Figure 76 XRD of a) Fresh SC3 powder b) SC3 powder aged at 900°C157

LIST OF SYMBOLS

Symbol	Definition	Units
A,B,C	Antoine Equation Constants	-
C_A	Instant Concentration	ppm
C_{A0}	Initial Concentration	%
p^{sat}	Saturation Pressure	Torr
S	Stoichiometric Number	ppm
T	Temperature	°C
T50	Light-off Temperature	°C
V_{eff}	Effective Volume	cm ³
v_o	Flow Rate	ml/min
Y	Gamma phase	-

LIST OF ABBREVIATIONS

A/F	Air to Fuel Ratio
AO	Aluminum Oxide
ATSB	Aluminum Tri Sec Butoxide
CZO	Cerium Zirconium Oxide
GHSV	Gas Hourly Space Velocity
HC	Hydrocarbon
HDPE	High Density Polyethylene
MFC	Mass Flow Controller
MS	Mass Spectrometer
NO _x	Nitrogen Oxides
OSC	Oxygen Storage Capacity
TWC	Three Way Catalyst

CHAPTER 1

INTRODUCTION

1.1. Exhaust Emissions

One of the major sources of atmospheric pollution are the emissions generated by transportation vehicles. These emissions are the consequence of incomplete combustion of fossil fuel and radical reactions of N and O at high temperatures (Martinez-Arias, et al., 2012). The main pollutants of the exhaust emissions are unburned or partially burned hydrocarbons (HCs), carbon monoxide (CO) and nitrogen oxides, mostly nitric oxide (NO) and catalytic technologies primarily focus on the elimination of these pollutants. Other compounds such as oxygen, hydrogen, nitrogen, water vapor, carbon dioxide and sulfur oxides (arising from the sulfur in fuel) are also present in the exhaust gas mixture. Even though sulfur oxides are polluting as well, they can only be eliminated by reducing to elemental sulfur which will lead to an accumulation in the system. Therefore, minimizing the amount of sulfur content in the fuel is a more effective solution for diminishing the sulfur containing emissions (Kaspar, et al., 2003). General composition of exhaust emissions for different types of engines are summarized in Table 1.

Table 1 Composition of exhaust emissions for diesel and gasoline engines (Martinez-Arias, et al., 2012)

Exhaust Component	Diesel Engine	Gasoline stoichiometric engine	Gasoline direct injection lean-burn engine
Hydrocarbons	10 - 330 ppm	400 - 5000 ppm	350 - 2300 ppm
Nitrogen oxides	200 - 1000 ppm	100 - 4000 ppm	800 - 2300 ppm
CO	150 - 1200 ppm	0.1 - 6 %	0.5 - 0.9 %
O ₂	5 - 15 %	0.2 - 2 %	0.6 - 7 %
H ₂ O	1 - 7 %	10 - 12 %	10 - 12 %
CO ₂	3 - 13 %	10 - 18 %	10 - 15 %
Sulfur oxides	10 - 100 ppm	15 - 60 ppm	10 - 50 ppm
Particulates	50 - 400 mg m ⁻³	-	-

1.2. Standards for Exhaust Gas Emissions

In late 1960's, depletion of air quality in large cities such as Los Angeles in USA and Tokyo in Japan had become such a serious concern that first environmental legislations regulating exhaust emissions were introduced. In 1970, emission standards were defined by California Clean Air Act in terms of six main pollutants; carbon monoxide, nitrogen oxides, hydrocarbons, photochemical oxidants, sulfur oxides and particulate matter. As a consequence, catalytic converters for removal of pollutant exhaust emissions began developing. Air quality problems were more severe in California, therefore starting from 1977, California Air Resources Board (CARB) legislated lower emission limits than the rest of the USA (Twigg, 2011). USA's measures were followed by other countries such as Japan, Switzerland and Australia. Later on, European Union announced strict emission limits for passenger cars in 1985 which was followed by the legislations of South Korea in 1987 and Brazil in 1988 (Ertl, et al., 1999). A historical overview upon emission standards of California is given in Table 2.

Table 2 Emission Standards of California (CARB) since 1993 (Twigg, 2011)

Year	Category	Emissions (g/mile)		
		HC	CO	NO _x
1993		0.25	3.40	0.40
1994	Tier 1	0.25	3.40	0.40
2003	Tier 1	0.25	3.40	0.40
2004	TLEV	0.125	3.40	0.40
	LEV	0.075	3.40	0.05
2005	LEV	0.075	3.40	0.40
	ULEV	0.040	1.70	0.05
2006	ULEV	0.040	1.70	0.20
	SULEV	0.010	1.00	0.02

LEV: Low Emission Vehicles, SULEV: Super Low Emission Vehicles

Today, emission limits have become much more stringent as the number of cars have been rapidly increasing all over the world. Automobile manufacturers are seeking solutions to improve the performance of their catalysts in order to meet the limits demanding as low as 99% conversion of the exhaust gases (Matsumoto, 2004).

1.3. Three Way Catalytic Converters

Three way catalytic converters (TWC) are dictated by the need of simultaneous conversion of the polluting compounds; HCs, CO and NO_x into relatively less harmful compounds; CO₂, N₂ and H₂O (Lassi, 2003). Exhaust gas mixture is a very complex media with a variety of compounds and numerous reactions taking place. Main reactions involved in a TWC are oxidation and reduction reactions as well as water – gas shift and steam reforming reactions. These simultaneous reactions are listed in Table 3.

Table 3 Reactions occurring in a Three Way Catalytic Converter (Kaspar, et al., 2003)

<i>Oxidation</i>	$2\text{CO} + \text{O}_2 \rightarrow 2\text{CO}_2$
	$\text{HC} + \text{O}_2 \rightarrow \text{CO}_2 + \text{H}_2\text{O}^{\text{a}}$
<i>Reduction</i>	$2\text{CO} + 2\text{NO} \rightarrow 2\text{CO}_2 + \text{N}_2$
	$\text{HC} + \text{NO} \rightarrow \text{CO}_2 + \text{H}_2\text{O} + \text{N}_2^{\text{a}}$
	$2\text{H}_2 + 2\text{NO} \rightarrow 2\text{H}_2\text{O} + \text{N}_2$
<i>Water Gas Shift</i>	$\text{CO} + \text{H}_2\text{O} \rightarrow \text{CO}_2 + \text{H}_2$
<i>Steam reforming</i>	$\text{HC} + \text{H}_2\text{O} \rightarrow \text{CO}_2 + \text{H}_2^{\text{a}}$

^a Unbalanced reaction

Extent of these reactions depend on a critical parameter defined as Air-to-Fuel ratio (A/F). Only at the stoichiometric A/F point 14.7, appropriate amounts of oxidizing and reducing agents present in the exhaust mixture and complete conversion of pollutants can take place (Kaspar, et al., 2003). When the engine operates with excess fuel (rich condition), A/F is below the stoichiometric ratio and the exhaust gas composition contains more reducing compounds such as HCs and CO than oxidizing compounds such as O₂ and NO_x. Conversely, if the engine operates over the stoichiometric point with excess air (lean condition), amount of oxidizing reactants will be higher than the amount of reducing reactants in the exhaust mixture (Ertl, et al., 1999). Effect of A/F ratio on the efficiency of HC, CO and NO_x conversions is shown in Figure 1.

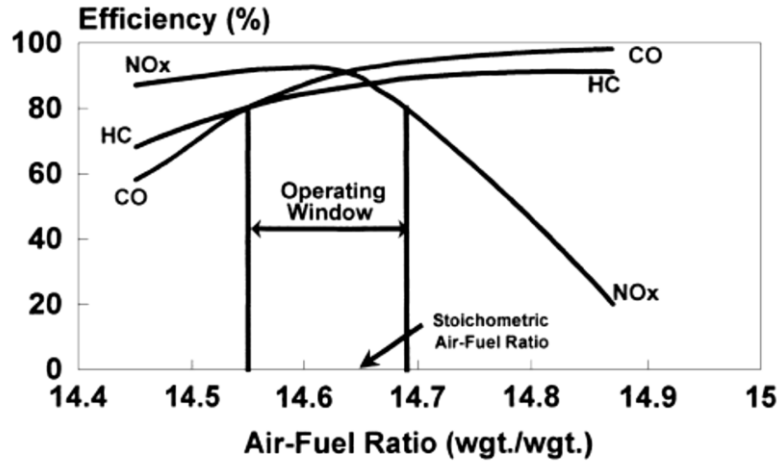


Figure 1 Effect of A/F ratio on conversion of pollutants in three way catalytic converter (Farrauto & Heck, 1999)

Simultaneous maximum conversions of HCs, CO and NO_x are achieved in a very narrow operating window which is approximately ± 0.05 around the stoichiometric A/F point (Farrauto & Heck, 1999). In order to maintain the A/F ratio as close as possible to the stoichiometric point, O₂ or lambda sensors are employed. The sensor measures the oxygen level at the inlet of the catalytic converter and provides feedback to the fuel injection control mechanism (Kaspar, et al., 2003). Diagram of a modern engine exhaust control system is shown in Figure 2.

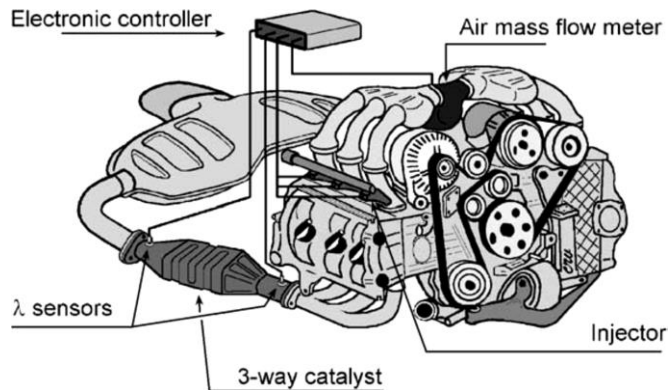


Figure 2 Control loop of TWC-Engine-Oxygen sensor (Kaspar, et al., 2003)

1.4. Structure and Components of Three Way Catalytic Converters

A typical structure of a three way catalytic converter consists of a honeycomb-like monolith placed inside a stainless steel container as shown in the Figure 3. Catalyst is loaded on the monolith with washcoating process. The monolith is either made of metallic (stainless steel) or ceramic (mostly cordierite) material (Lassi, 2003). The major advantage of metallic monoliths is that they possess higher surface to volume ratio with lower wall thicknesses (Pratt & Cairns, 1977). However, loading of catalyst on metallic monoliths can be poor, due to low adhesion capability of metals. On the other hand, washcoating process with ceramic monoliths are much more efficient by virtue of their porous structure. Also, ceramic monoliths are more economically feasible. Therefore, cordierite ($2\text{MgO} \cdot 2\text{Al}_2\text{O}_3 \cdot 5\text{SiO}_2$) monoliths are extensively employed in TWCs (Kaspar, et al., 2003).

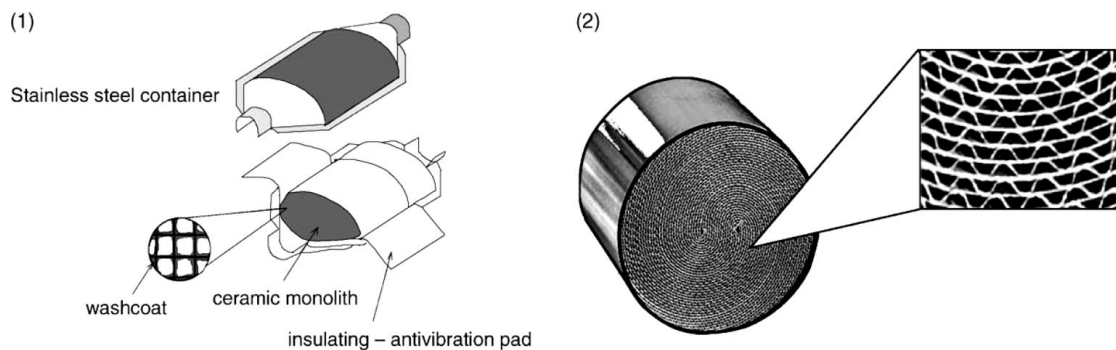


Figure 3 (a) Catalytic converter components (b) Honeycomb structure in a metallic monolith (Kaspar, et al., 2003)

Washcoating process is carried out by dipping the monolith into a slurry (washcoat) containing catalyst precursors. Excess slurry is blown out of the monolith by air and a calcination process is applied in order to fix the catalyst (Kaspar, et al., 2003).

The washcoat consists of several components for different purposes. Noble metals such as platinum, rhodium and palladium are the key components of a three way catalyst as they are the active phases for catalytic reactions. Pt and Pd are chosen for their good

performance in HC and CO oxidation (Armor, 1992) whereas Rh is efficient in NO_x reduction (Taylor, 1993). In particular, Pd has been extensively used in TWC compositions due to its relatively good intrinsic activity for CO conversion (Bunluesin, et al., 1996), ability to promote HC conversions (Trovarelli, 1996), higher resistance to thermal sintering (Summers, et al., 1988) and lower market price than that of Rh and Pt (Kaspar, et al., 2003).

Another vital component of a TWC is CeO₂-ZrO₂ mixed oxide. Among other contributions, oxygen storage capacity (OSC) of ceria is definitely the most important one. At cycling lean and rich conditions, ceria has the ability to store and release oxygen, respectively. OSC property of ceria provides promotion on CO and HC oxidations by virtue of the use of lattice oxygen. Zirconia is added to ceria since it substantially enhances the OSC and also thermal stability (Kaspar, 2003; Lassi, 2003)

Surface area of the honeycomb monoliths are insufficient for a high dispersion of the catalyst. Therefore, alumina is employed due to its high surface area and also its good thermal stability (Kaspar, et al., 2003). Mostly, γ -alumina is preferred for its higher surface area among other transitional aluminas (Anderson, 1975). However, at temperatures above 1000°C, stabilization of alumina is necessary to prevent the surface area loss by transition to α -alumina. For this purpose, stabilizing agents such as lanthanum or barium oxides are added to the washcoat, as well (Kaspar, et al., 2003).

1.5. Light-Off Temperature

Performance of a three way catalyst is evaluated by a parameter called “Light-off Temperature” which is defined as the temperature at which 50 % conversion of a specific reactant is attained. TWCs shows typical light-off type behavior on conversion vs. temperature curves as a steady increase from 0 % to 100 % conversion. Lower light-off temperatures indicate better catalytic performance. Most of the emissions are released during the cold-start period of an engine and therefore, TWCs with lower light-off temperatures are needed for the abatement of cold start emissions (Ertl, 1999; Kaspar 2003).

1.6. Deactivation of Three Way Catalysts

There are several reasons that are accountable for catalytic activity loss of a TWC. Thermal aging is the major pathway for deactivation. Exposure to high temperatures results in sintering of the oxygen storage component and loss of its redox property (Fornasiero, et al., 2000). Thermal aging also leads to other deactivation mechanisms such as metal losses, sintering and alloying of noble metals and metal support interactions (Granados, et al., 2005). Additionally, active sites of the catalyst can be poisoned or inhibited by some foreign elements such as Pb, S, Zn, and P present in the fuel (Lambrou, et al., 2005).

1.7. Promotion Noble Metal by Base Metals

Although the technologies for TWCs are well-established, further improvement of catalytic performance is always in demand with stringent emission regulations (Li, et al., 2011). In recent years, introduction of transition metals into TWC compositions has started to draw attention, especially in Pd-based TWCs. A second cheaper metal would not only offer promotion in catalytic performance but is also desired in an economical point of view. Resulting bimetallic catalyst display some special properties not anticipated by a simple interpolation of the reactivity of the two components. For instance, introduction of a second component might create a new interface with Pd to the reactants and generate new surface active sites for reaction. This behavior is altered due to redox capability of the second metal, as in the case of Cr, Ni, Mo, Fe, and Mn (Martinez-Arias, et al., 2012). A detailed discussion for introduction of base metals into TWC compositions is given Literature Survey section.

1.8. Computational Chemistry

Computational chemistry is a sophisticated conjunction of mathematical techniques and fundamental physical laws for investigation of chemistry-related problems with utilization of computers (Jensen, 2007). Chemistry defines the question, physics defines the laws behind that chemical system and a numerical representation of the question is formulated by mathematics. Eventually, computers are utilized to solve the

mathematical model and yield numbers that contain physical significance (McDouall, 2013). Commonly investigated questions are;

- Molecular geometry such as shapes of molecules, bond lengths and angles
- Energy of molecules and transition states
- Stability of chemical structures
- Chemical reactivity of molecules and revelation of reaction pathways
- Surface intermediates in reactions that cannot be observed by experimental methods
- Physical and chemical properties of substances before synthesis process (Heine, 2009; Lewars, 2003; McDouall, 2013)

Depending on the objective of the study, many methods are applicable. The main tools belonging to five broad classes are *Molecular mechanics*, *Ab initio calculations*, *Semi empirical methods*, *Molecular dynamics* and *Density functional methods* (Lewars, 2003).

In this study, only Density Functional Theory (DFT) is viewed in detail.

1.8.1. Density Functional Theory

Density Functional Theory is a practical and accurate technique that has become very popular in recent years. The basic principle behind DFT is that the energy of a molecule is determined with the electron density rather than wave function in the solution of Schrödinger equation (Young, 2001). The theory proposes that electrons are uniformly distributed in the six-dimensional phase space for the motion of an electron at the rate of two for each h^3 of volume and using nuclear charge and electron distribution, effective potential field can be found (Parr & Yang, 1994). DFT method is developed according to two important theorems constructed by Hohenberg and Kohn. The first theorem states that the ground-state energy of the Schrödinger equation is a unique function of the electron density. Second theorem proposes that the true electron density corresponding to the full solution of the Schrödinger equation also minimizes the energy of the overall functional (Sholl & Steckel, 2009).

Formulation of Density Functional Theory starts with Schrödinger equation by electron density functional. Starting with Schrödinger equation: (Seminario, 1995)

$$\hat{H}\Psi = E\Psi \quad (1.1)$$

Where \hat{H} represents the Hamiltonian operator for a molecular system with M nuclei and Ψ represents wave function. Hamiltonian operator is extended with external potential \hat{u}_{ext} kinetic energy operator \hat{T} and electron repulsion operator \hat{V}_{ee}

$$\hat{H} = \hat{T} + \hat{u}_{\text{ext}} + \hat{V}_{ee} \quad (1.2)$$

Where

$$\hat{T} = -\frac{1}{2}\sum_{i=1}^N \nabla_i^2 \quad (1.3)$$

$$\hat{u}_{\text{ext}} = \sum_{i=1}^N \vartheta(\vec{r}_i) = -\sum_{i=1}^N \sum_{A=1}^M \frac{Z_A}{r_{iA}} \quad (1.4)$$

$$\hat{V}_{ee} = \sum_{i=1}^N \sum_{j>i}^N \frac{1}{r_{ij}} \quad (1.5)$$

Wavefunction in Schrödinger equation as a function of position vectors (\vec{r}_N) can be expressed as:

$$\Psi = \Psi(\vec{r}_1, \vec{r}_2, \vec{r}_3, \dots, \vec{r}_N) \quad (1.6)$$

Rather than using N-electron wave functions as other methods, Schrödinger equation is solved with electron written as:

$$(\vec{r})=N\langle\Psi|\delta(\vec{r}-\vec{r}_i)|\Psi\rangle \quad (1.7)$$

With equation (1.7), a singular expectation value is written as

$$(\vec{r}_1)=N\int d\vec{r}_2 d\vec{r}_3 \dots d\vec{r}_N |\Psi(\vec{r}_1, \vec{r}_2, \vec{r}_3, \dots, \vec{r}_N)|^2 \quad (1.8)$$

Using this information, total energy is expressed as a functional of external energy and electron density:

$$E=\langle\Psi|\hat{H}|\Psi\rangle=\int v_{\text{ext}}(\vec{r})(\vec{r})d\vec{r}+\langle\Psi|\hat{T} + \hat{V}_{ee} |\Psi\rangle \quad (1.9)$$

Ground state energy for a given external energy v is written as:

$$E = E[\rho] \quad (1.10)$$

$$E = E_v[\rho] = \int v(\vec{r})\rho(\vec{r})d\vec{r} + \langle \Psi | \hat{T} + \hat{V}_{ee} | \Psi \rangle = \int v(\vec{r})\rho(\vec{r})d\vec{r} + F[\rho] \quad (1.11)$$

Where $F[\rho]$ is the universal functional which is identical for all systems and independent of external energy. Kohn-Sham procedure is applied to Schrödinger equation by using the universal functional. Assumption of Hamiltonian operator is:

$$\hat{H}_\lambda = \hat{T} + \hat{v}_\lambda + \lambda \hat{V}_{ee} \quad (1.12)$$

Value of λ is between 0 and 1, where in an ideal system with non-interacting electrons λ is equal to 0 and in a real system under the effect of \hat{v}_{ext} λ is equal to 1. From the Schrödinger equation:

$$\hat{H}_\lambda \Psi_\lambda = \hat{E}_\lambda \Psi_\lambda \quad (1.13)$$

Energy becomes:

$$E_\lambda = \langle \Psi_\lambda | \hat{H}_\lambda | \Psi_\lambda \rangle = \int v_\lambda(\vec{r})\rho(\vec{r})d\vec{r} + \langle \Psi_\lambda | \hat{T} + \lambda \hat{V}_{ee} | \Psi_\lambda \rangle \quad (1.14)$$

Rearranging the equation:

$$[\rho] = \int v_{\text{ext}}(\vec{r})\rho(\vec{r})d\vec{r} + T_s + \int \langle \Psi_\lambda | V_{ee} | \Psi_\lambda \rangle d\lambda \quad (1.15)$$

Where T_s is an imaginary quantity representing kinetic energy of the non-interacting electron system. In order to simplify the equation an exchange correlation energy term was defined as the difference between the second integral in (1.15) and classical interaction energy.

$$V_{\text{classical}}[\rho] = \frac{1}{2} \int \int d\vec{r}_1 d\vec{r}_2 \frac{\rho(\vec{r}_1)\rho(\vec{r}_2)}{|\vec{r}_1 - \vec{r}_2|} \quad (1.16)$$

$$E_{xc}[\rho] = \int_0^1 \langle \Psi_\lambda | \hat{V}_{ee} | \Psi_\lambda \rangle d\lambda - \frac{1}{2} \int \int d\vec{r}_1 d\vec{r}_2 \frac{\rho(\vec{r}_1)\rho(\vec{r}_2)}{|\vec{r}_1 - \vec{r}_2|} \quad (1.17)$$

Rearranging Equations 1.15 and 1.17;

$$\int_0^1 \langle \Psi_\lambda | \widehat{V}_{ee} | \Psi_\lambda \rangle d\lambda = V_{classical} + E_{xc}[\rho]$$

$$E[\rho] = \int v_{ext}(\vec{r})\rho(\vec{r})d\vec{r} + T_s + V_{classical}[\rho] + E_{xc}[\rho] \quad (1.18)$$

Total energy of the electronic system is expressed by equation (1.18). With this equation, all terms are known except exchange-correlation energy part. Kohn-Sham equations are obtained via minimizing the total energy with respect to electron density:

$$\left[-\frac{1}{2}\nabla^2 + v_{ext} + \int d\vec{r}_2 \frac{\rho(\vec{r}_2)}{|\vec{r}_1 - \vec{r}_2|} + \frac{\delta E_{xc}[\rho(\vec{r})]}{\delta \rho(\vec{r})} \right] \varphi_i = \varepsilon_i \varphi_i \quad (1.19)$$

Exchange energy can be calculated by utilization of some approximations such as local density approximation (LDA) or generalized gradient approximations (GGA). Exchange energy according to LDA is written as:

$$E_{xc}^{LDA}[\rho] = \int \varepsilon_{xc}^{hmg}(\rho)\rho(\vec{r})d\vec{r} \quad (1.20)$$

For GGA method, a gradient factor is employed in electron density calculations. Exchange energy according to GGA is written as:

$$E_{xc}[\rho] = \int \varepsilon_{xc}[\rho, \nabla\rho]\rho(\vec{r}) d\vec{r} \quad (1.21)$$

(Seminario, 1995)

GGA method gives more accurate results since exchange correlation of the system is related with both density and derivatives of the density. (Jensen, 2007)

1.9. Objective of the Study

The main objective of this study is to combine computational chemistry with experimental studies to evaluate and interrelate catalytic efficiencies of TWCs in a novel approach. Additionally, promotional effects of manganese doping in TWC compositions are investigated in particular. Starting with the computational studies via DFT methods, CO oxidation mechanisms are investigated on Mn and noble metal (Pd and Rh)

substituted ceria-zirconia surfaces and compared with each other. In the experimental part, catalysts having similar compositions with DFT models were prepared via two different synthesis methods and their catalytic activity tests are performed in a dynamic activity tests system. Catalytic performance are evaluated in terms of maximum conversions and light-off temperatures. Outcomes of computational studies are correlated with experimental results for interpretations on catalytic activity.

CHAPTER 2

LITERATURE SURVEY

2.1. Three Way Catalyst Preparation

Since CeO_2 and $\text{CeO}_2\text{-ZrO}_2$ mixed oxides serve as widely used support materials and promoters in various catalysts, intensive effort has been spent upon the investigation of their role and properties on various catalytic systems. Di Monte et al. (1998), established that the redox properties (OSC) and also the catalytic activity of CeO_2 was enhanced with ZrO_2 doping. High oxygen mobility in the bulk solid solution of $\text{CeO}_2\text{-ZrO}_2$ mixed oxide system leads to an independence of surface area for the redox processes to occur. In this way, the catalysts were thermally stable and even after strong sintering, significant deactivation was not encountered.

Kaspar et al. (2003 a), investigated the textural and structural properties of $\text{Ce}_x\text{Zr}_{1-x}\text{O}_2$ solutions synthesized via citrate complexation method. According to their findings, compositions with higher Ce content were found to be more suitable for catalytic applications operating at low-medium temperatures ($< 1000^\circ\text{C}$). Di Monte & Kaspar (2005), asserted that the most texturally stable composition is $\text{Ce}_{0.8}\text{Zr}_{0.2}\text{O}_2$. Gennari et al. (2008) used co-precipitation and microemulsion methods for the synthesis of $\text{Ce}_{0.8}\text{Zr}_{0.2}\text{O}_2$ mixed oxides. Homogenous $\text{Ce}_{0.8}\text{Zr}_{0.2}\text{O}_2$ nanoparticles were successfully produced with both techniques, however the product of co-precipitation technique had higher surface area.

Effect of synthesis method for CeO₂-ZrO₂ mixed oxide was also studied by Zhao et al. (2010). Co-precipitation, hydrothermal, homogeneous precipitation and microemulsion methods were used to prepare Ce_{0.67}Zr_{0.33}O₂ support. Characterizations of the fresh mixed oxides indicated that the products of hydrothermal and microemulsion methods had higher OSC, however after aging process at 1100°C, a co-existence of tetragonal and cubic phases with a strong sintering led to deterioration on those two products. On the other hand, the products of co- and homogenous precipitation had tetragonal phase only, and hence kept satisfactory OSC and low temperature reducibility after aging process.

In another study, Kaspar & Fornasiero (2003 b), studied the effect of CeO₂-ZrO₂ dispersion on Al₂O₃. They stated that the most striking effect of Al₂O₃ deposition on CeO₂-ZrO₂ mixed oxide is that the enhancement of thermal stability compared to bare mixed oxide. Al₂O₃ retards the sintering rate of CeO₂-ZrO₂ and thus, even after a harsh calcination, particle size was not increased that much and was still below the critical size. However, in the case of impregnation of Al₂O₃ with cerium and zirconium nitrates together, an unstable and nonhomogeneous phase was obtained. Especially at high temperatures, formation of CeAlO₃ hinders the OSC component severely. For this reason, CeO₂-ZrO₂ mixed oxide is synthesized previously and then Al₂O₃ and other components are suspended previously synthesized with the mixed oxide to obtain the washcoat for TWCs.

Gupta et al. (2010) studied the oxygen storage/release characteristics in noble metal-, transition metal- and rare earth ion doped ceria synthesized with solution combustion method. Detailed H₂-TPR analyses showed that substitution of noble metal and transition metals greatly enhanced the oxygen storage and release capacity (OSC) of Ce_{1-x}M_xO_{2-δ} (M= Pd, Pt, Ru, Mn, Fe, Ni, Co, Cu) whilst rare earth ion (La and Y) doping had almost no improvement in OSC. In the presence of Pd dopant ion, reducibility of Fe-, Mn- and Co- doped ceria was highly improved with a synergistic interaction, yet no such behavior was observed for Ni- and Cu- doped ceria. Particularly,

an intense synergistic interaction between Mn, Pd and Ce ions resulted a tremendous increase in OSC.

An extensive study upon ionic noble metal catalysts and their catalytic performance was carried out by Hedge et al. (2008). Nanocrystalline $Ce_{1-x}M_xO_{2-\delta}$ and (M= Pd, Pt, and Rh, $x= 0.01-0.02$) were synthesized by solution combustion method. Substitution of Pd ions were confirmed via XRD analyses. Decrease in the lattice parameter and the absence of diffraction patterns belonging to Pd metal or PdO confirmed the atomic substitution of Pd ion. Comparing with Pt and Rh, Pd ion substituted catalysts showed much better activity for the conversions of CO, hydrocarbons and NO. Conversion rates of the ionic catalysts were much higher compared to impregnated catalysts with same metal amount.

Ceramic monoliths are the most commonly used catalyst carriers for three way catalysts. Off all ceramic monoliths, cordierite ($2MgO.2Al_2O_3.5SiO_2$) is the most widespread support due to its low thermal expansion coefficient and high mechanical strength. (Trimm, 1995; Gandhi & Narula, 1997) A monolithic three way catalyst is prepared by dipping the dry monolith into the washcoating slurry containing the catalyst and other additives. The monolith is then taken out and the excess slurry is gently blown out with pressurized air. A drying and calcination process follows to fix the catalyst coating on the monolith. In order to provide a necessary contact surface between the monolithic support and washcoat, binders are employed. Pseudo-boehmite can be used as a binder in the coating of alumina. The amount of binder in the washcoat should be around 10 wt % whereas the total solid content should be 40-50 wt % (Nijhuis, et al., 2001). Nitric acid is used for the activation of pseudo-boehmite as a binder. (Lachman, et al., 1994)

2.2.Catalytic Activity

Gonzales-Marcos et al. (2012), investigated the catalytic activity behavior of Pd/Ce_{0.68}Zr_{0.32}O₂ using cycled redox complex gas mixtures. The light-off curves of CO, C₃H₆, O₂, and NO species were correlated to different palladium species present on the surface. Pd(I) like species with metallic character were observed in the low temperature range where CO, O₂ and C₃H₆ conversions occur. In the high temperature range, Pd(0)

species were present on the surface and NO was converted with a maximum conversion of 70 %.

Wang et al. (2012) studied the effects of steam on catalytic activity with Pd/Ce_{0.67}Zr_{0.33}O₂-Al₂O₃ catalyst. Activity tests were carried out in a micro reactor with a stoichiometric gas feed of CO, C₃H₈, NO, O₂, CO₂ and balance N₂ and at GSHV of 50000 hr⁻¹. In order to simulate the real TWC environment, 5 wt % of steam was injected to the reactor. Due to water gas shift (WGS) reactions arising from the steam feed, conversion of CO was highly improved in terms of lower T50 and T90 temperatures. Also, C₃H₈ oxidation was enhanced with steam reforming (SR) reactions promoted by addition of steam.

Li et al. (2012) investigated the effect of transition metal doping in CeO₂-ZrO₂ for the application area of Pd-only three way catalysts. Cr, Mn, Fe, Co and Ni were doped into ceria-zirconia mixed oxide with 5 wt % transition metal content and the resulting supports were then impregnated with 0.5 wt % Pd. Catalytic activity tests were performed in a fixed bed continuous flow reactor using a gas mixture of NO, NO₂, C₃H₆, CO, O₂ and balance Ar with a GHSV of 43,000 hr⁻¹. According to activity results, catalysts containing Fe, Mn and Co metals promoted catalytic activity in terms of light-off temperatures and a remarkable enhancement of CO conversion was detected with Mn containing catalyst.

Hickey et al. (2004), reported a reactivation of the deactivated Pd/Ce_{0.68}Zr_{0.32}O₂ catalyst after treating with high temperature oxidation. The catalyst was aged at cycled redox conditions which led to an increase in the light-off temperatures. After the oxidative treatment was applied, Pd was re-dispersed over the CZO support resulting a significant improvement in the activity. Same procedure was applied to Pd/Al₂O₃ catalyst and just a small difference was observed in the activity, revealing that CZO support plays an important role in the restoration of the catalytic activity.

2.3. Density Functional Studies

Nolan et al. (2005 b), implemented periodic DFT computations for bulk ceria and its low index surfaces using VASP package and PAW method. The lattice parameter for the bulk ceria was obtained as 5.470 Å and found to be consistent with the experimental value of 5.411 Å. Computations showed that the relative stability of the surfaces are in the increasing order of (111) > (110) > (100) (Nolan, et al., 2005 a). In a complementary study, the same group investigated the geometry and electronic structure of (111), (110) and (100) surfaces including oxygen defects, this time using the DFT + U method for the comprehension of electronic correlations. Calculations revealed that the formation of oxygen deficiencies are not in the same order with the surface stability and ceria (110) surface was found to have the lowest oxygen vacancy formation energy.

As the experimental studies indicate that the thermal stability and the redox behavior of ceria are substantially enhanced by the inclusion of zirconia, quite a number of DFT studies were carried out in order to explain this behavior. Wang et al. (2009), performed DFT + U calculations to investigate the effect of Zr-doping on the oxygen storage property in a series of $Ce_{1-x}Zr_xO_2$ with x values of 0.75, 0.50 and 0.25. Bond energies were found to be increasing almost linearly with increasing Zr content, suggesting that Zr doping does not lower the bond strength of oxygen. Energy of relaxation profile has a parabolic curve with a minimum energy value at x=0.5, and since the energy of relaxation is a more dominant term than bond energy, equimolar concentrations of Ce and Zr exhibit the highest oxygen storage property.

Another DFT study regarding Zr-doping was carried out by Yang et al. (2008). CeO_2 (110) and $Ce_{0.75}Zr_{0.25}O_2$ (110) surfaces were studied in order to designate the effects of Zr-dopant on the redox property. They postulate that Zr dopant has the capability of changing the electron localization and lowers the reduction energy. Oxygen vacancy formation leads to the reduction of the Ce^{+4} ions to Ce^{+3} and smaller Zr atoms facilitate the reduction process by sparing some space for the larger Ce^{+3} neighboring ions.

Other than Zr doping, incorporation of noble metals such as Pd, Pt and Rh in ceria also studied. Yang et al. (2007), performed DFT calculations on Pd adsorbed ceria (111) with

VASP program using PAW method and GGA approximation. Pd adatom was adsorbed on different sites of the surface and was seen to be favoring Ce-O bridge position the most. Also, the interaction at Pd/CeO₂ interface enables accommodation of extra electrons and reduces the oxygen vacancy formation energy by easing the reduction process.

CO oxidation mechanisms on Pd₄ and Rh₄ metal cluster adsorbed and Pd and Rh substituted CeO₂ and Ce_{0.75}Zr_{0.25}O₂ surfaces were studied using by Gerçeker & Önal (2013). DFT was implemented with VASP package program and PAW method was applied with GGA approximation. Two CO molecules were exothermically oxidized to two CO₂ molecules on Pd substituted CZO surface using surface oxygen and creating an oxygen vacancy. Energy for oxygen vacancy formation on Pd-CZO was reported as 43.7 kcal/mole. An activation barrier of 45 kcal/mole was reported in the steps between the first CO adsorption and CO₂ desorption on Pd-CZO surface. CO oxidation on Rh substituted CZO could not proceed because of the strong attachment of oxygen on the vacant site.

Cen et al. (2012), implemented DFT + U calculations for Mn substituted CeO₂ (111) surface by using VASP program with PAW pseudopotentials. They reported that the oxygen vacancy formation energy decreases by introduction of Mn regardless of the vicinity of Mn atom to the dopant site. Mn doping induces Mn 3d–O 2p gap which enables to decrease the first and second oxygen vacancy formation energies to -0.46 eV and 1.40 eV, respectively, whereas the vacancy formation energy of pure ceria was obtained as 2.40 eV.

Tang et al. (2010), investigated the effects of doping of Ceria with different metals (M = Mn, Pr, Sn, Zr) using DFT calculations. They suggested that there are two mechanisms involved in the formation of oxygen vacancies. One mechanism is related to the structural distortion which is observed in the case of Zr-, Ti- and Si- doping, and this mechanism results in the reduction of the Ce atoms. For the Mn-, Sn- and Pr- doped CeO₂ structural distortion is accompanied by electronic modification as a secondary mechanism and the reduction occurs on the dopant ion. According to their findings, Mn-

doped CeO₂ has the lowest oxygen vacancy formation energy among other dopants, since it has the smallest radius which leads to strong structural distortions.

Oxygen vacancy formation on Mn doped ceria was also studied by Pintos et al. (2013). DFT calculations were performed by VASP program with PAW method using PBE functional and GGA approximation. They reported that Mn doping reduces the energy for creation of oxygen defects. Energy for the formation of two oxygen vacancies on Ce_{0.875}Mn_{0.125}O₂ (111) surface was obtained as 2.66 eV when the energy requirement for a single oxygen vacancy formation on CeO₂ (111) was 2.69 eV. Creation of a single oxygen defect was followed by the reduction of Mn³⁺ cations to stable Mn²⁺ and after the second oxygen defect, one Ce atom was also reduced to Ce³⁺.

Zhang et al. (2012), reported enhanced oxygen storage capacity of Mn-doped ceria by means of both theoretical and experimental investigation. DFT studies showed that Mn ions activate lattice oxygen by increasing the Ce-O bond length and reduced the oxygen vacancy formation energy. In the experimental part of their study, CeO₂ and Ce_{0.88}Mn_{0.12}O_y nanoparticles were synthesized and OSC measurements confirmed that the substitution of Mn enhances the OSC property of ceria.

CO oxidation over Mn doped ceria (111) was studied by Hsu et al. (2012), by using VASP package program with PAW method and GGA approximation. According to their findings, CO oxidation on the ceria surface with Mn adatom restricts oxygen vacancy formation with a barrier of 0.84 eV. On the other hand, Mn substituted Ce_{0.875}Mn_{0.125}O₂ surface performs CO oxidation with no activation barrier and CO₂ desorbs by forming an oxygen vacancy. The vacancy is then healed by an O₂ gas molecule and the surface is regenerated.

CHAPTER 3

EXPERIMENTAL AND COMPUTATIONAL METHODOLOGY

3.1. Experimental Method

In the experimental part of this study, three way catalysts are synthesized, washcoated on laboratory scale monoliths and tested for their catalytic activities in a dynamic test system operating with simulated exhaust gas mixture. Initially, TWCs are prepared with two different techniques; Impregnation Method and Solution Combustion Method. After powder catalysts are obtained, they are mixed with alumina for preparing the washcoating slurry. Monoliths are washcoated with the slurry and catalytic activity tests are performed with the monolithic catalysts. Performance of the catalysts are evaluated by the conversion versus temperature graphs of the reactants.

3.2. Catalyst Preparation

3.2.1. Catalyst Preparation by Impregnation Method

Impregnation method is a conventional method commonly used for the synthesis of three way catalysts, therefore initially, catalytic performances were investigated via impregnated catalysts with varying compositions. Catalyst preparation by impregnation method is carried out in two steps; ceria-zirconia support is initially prepared and metals impregnated on the support as explained in the following sections.

3.2.1.1. Preparation of Ceria-Zirconia Support

Ceria-zirconia mixed oxide is synthesized using co-precipitation method as explained by (Gennari, et al., 2008). The ratio of Ce to Zr was selected as four ($\text{Ce}_{0.8}\text{Zr}_{0.2}\text{O}_2$) considering that it has been suggested as the most texturally stable ceria-zirconia composition (Trovarelli, 1996) and also its proximity to the surface models ($\text{Ce}_{0.75}\text{Zr}_{0.25}\text{O}_2$) in the computational studies.

Cerium (III) nitrate hexahydrate ($\text{CeN}_3\text{O}_9 \cdot 6\text{H}_2\text{O}$) (Aldrich, 99%) and Zirconyl nitrate hexahydrate ($\text{N}_2\text{O}_7\text{Zr}_{\text{aq}}$) (Fluka, % 27 & Zr (gravimetric)) are used as precursors and an aqueous solution is prepared in 1 lt double distilled water with Ce/Zr atomic ratio of 4/1. For complete oxidation, hydrogen peroxide (H_2O_2) (J.T. Baker, 30% v/v) is added to solution and the mixture was vigorously stirred for 1 h. The solution is then added to excess ammonium hydroxide solution (NH_4OH) (Aldrich, 33% NH_3) drop wisely. The resulting suspension was kept for 1 day for complete precipitation. The precipitated product is extracted, washed with isopropanol ($\text{CH}_3\text{CHOHCH}_3$) (J.T. Baker) and filtered. Following, the product is refluxed with isopropanol for 6 h and then dried at 150°C for 12 h. Finally, the resulting powder is grounded and calcined in the muffle furnace with dry air at 500°C for 3h.

3.2.1.2. Impregnation of Metals on Ceria-Zirconia Support

In this study, ceria-zirconia mixed oxide support is impregnated with Palladium, Manganese and Rhodium metals with varying compositions. Palladium (II) chloride solution (Aldrich, PdCl_2 , 5 wt% solution in 10 wt% HCl), and Rhodium (III) nitrate solution (Aldrich, $\text{Rh}(\text{NO}_3)_3 \sim 10$ wt% Rh in 5 wt% nitric acid (HNO_3)) are used readily available metal sources. For the case of Mn, 5 wt % aqueous solution is prepared using Manganese (II) nitrate tetrahydrate ($\text{Mn}(\text{NO}_3)_2 \cdot 4\text{H}_2\text{O}$) (Merck) as metal source. Water capacity of CZO is determined as ml water/1 g of sample, prior to impregnation process. Amount of water is important since too much water might cause pore blockage and prevent uniform distribution of metals. To obtain homogenous mixtures, metals are dissolved in water that is 1.5 times of the water capacity of CZO and mixed in rotary evaporator for 30 min with no heat or vacuum applied. Following, CZO support is added

to the metal-water solution and the flask the containing the mixture is immersed in a water bath at 80°C with 450 mbar vacuum in rotary evaporator and mixed with a rotational speed of 130 rpm until all the liquid in the flask evaporates. Resulting powder was dried at 150°C for 12 h, then finely grounded and calcined in the muffle furnace at 550°C with dry air for 1 h.

With this technique, five catalysts with different metal contents and combinations were synthesized. Labels and compositions of the impregnated catalysts (denoted as IMP) are given in Table 4.

Table 4 Labels and compositions of the catalysts synthesized via impregnation method

Catalyst ID	Composition
IMP1	(0.70 wt % Pd)/CZO + AO
IMP2	(0.70 wt % Mn)/CZO + AO
IMP3	(0.60 wt % Pd)/CZO + (0.10 wt % Mn)/CZO + AO
IMP4	(0.10 wt % Pd)/CZO + (0.60 wt % Mn)/CZO + AO
IMP5	(0.10 wt % Rh)/CZO + (0.60 wt % Mn)/CZO + AO

3.2.2. Catalyst Preparation by Solution Combustion Method

Solution combustion method is used for synthesizing single phase $Ce_{1-x}M_xO_{2-\delta}$ structures with ionic doping of metals (Hedge, et al., 2008). Unlike the impregnation method, synthesis is performed in a single step and all catalyst precursors are involved at the same time. Combustion mixture is prepared using Cerium (III) nitrate hexahydrate ($CeN_3O_9 \cdot 6H_2O$) (Aldrich, 99%) and Zirconyl nitrate hexahydrate ($N_2O_7Zr_{aq}$) (Fluka, % 27& Zr (gravimetric)), Palladium (II) chloride solution (Aldrich, $PdCl_2$, 5 wt% solution in 10 wt% HCl) and Manganese (II) nitrate tetrahydrate $Mn(NO_3)_2 \cdot 4H_2O$ (Merck) as catalyst precursors. An aqueous solution is prepared using the precursors at desired stoichiometries and urea (CH_4N_2O) (Sigma Aldrich, 99.5%) is added to the mixture as the fuel. After vigorous stirring, combustion mixture is introduced to the muffle furnace maintained at 450°C. Initially, the mixture boils, froths and all the liquid evaporates.

Following, the surface ignites with a flame and a voluminous solid product is formed within 5 min (Bera, 2000; Hedge, 2008; Murugan & Ramaswamy, 2005; Priolkar, 2002).

With this technique, three catalysts with different metal contents and combinations were synthesized. Labels and compositions of the catalysts synthesized via solution combustion method (denoted as SC) are given in Table 5.

Table 5 Labels and compositions of the catalysts synthesized via solution combustion method

Catalyst ID	Composition
SC1	$\text{Ce}_{0.79}\text{Zr}_{0.2}\text{Pd}_{0.01}\text{O}_2$
SC2	$\text{Ce}_{0.80}\text{Zr}_{0.1}\text{Mn}_{0.1}\text{O}_2$
SC3	$\text{Ce}_{0.79}\text{Zr}_{0.1}\text{Mn}_{0.1}\text{Pd}_{0.01}\text{O}_2$

3.2.3. Preparation of Washcoating Slurry

For preparation of the washcoating slurry, both catalysts synthesized via two different methods are mixed with gamma phase aluminum oxide (AO) ($\gamma\text{-Al}_2\text{O}_3$) and pseudoboehmite binder material. Cerium content of the mixture is adjusted to be 19 wt % of the total solid amount. Initially, mixed oxide catalyst and alumina are mixed with deionized water to obtain a slurry containing 40 wt % solid content. The mixture is homogenized in a ball mill operating at 275 rpm for 24 h. Following the ball milling process, the mixture is dried at 150°C for 12 h, and the solid product is grounded and calcined in muffle furnace at 550°C for 1 h. Next, pseudoboehmite is added to the powder mixture as 10 wt % of AO and again a slurry containing 40 wt % solid content is prepared with deionized water. Slurry is ball milled at 275 rpm for 30 min and then nitric acid is added to the slurry ball milling is continued for another 3h in order to activate pseudoboehmite. Preparation of pseudoboehmite is explained in the following section. (Lachman, 1994; Nijhuis, 2001).

3.2.4. Preparation of Pseudoboehmite

Pseudoboehmite is prepared by sol-gel method following the synthesis procedure given by (Nguefack, et al., 2003). Aluminum-tri-sec-butoxide (ATSB) ($\text{Al}(\text{OC}_4\text{H}_9)_3$) (Aldrich, 97%) is hydrolyzed with deionized water by vigorous stirring at 60°C for 2 h. Hydrochloric acid HCl (Aldrich, min 37%) is added to solution in order to achieve peptization and the solution is stirred for 1 h at 80°C. The gel product is then dried at 150°C for 48 h. Resulting powder sample is grounded and then calcined in the muffle furnace at 300°C (heating rate of 5°C/min) with dry air for 5 h.

3.2.5. Monolith Coating

In this study, washcoat is coated on laboratory scale monoliths which are 13 mm in height and 22 mm in diameter and have cell densities of 600 cells/in². Initially, bare monoliths are weighed after a drying process at 150°C for 30 min. Then by dip coating technique, monolith is dipped into the washcoating slurry, taken out, turned upside down and dipped again for an efficient coating of the honeycomb structure. The excess slurry deposited in the channels is blown out with pressurized air. Washcoated monoliths are dried at 150°C for 30 min and then calcined at 500°C for 3 h. After calcination, excess coating on the outer walls of the monolith is cleaned and the monolith is weighed again. If the coating amount is found to be insufficient, the coating process is repeated (Nijhuis, et al., 2001).

3.3. Catalyst Characterizations

Characterizations of the catalysts are performed with ICP-MS, XRD, HRTEM and BET methods. Metal contents of the washcoating slurries are analyzed by “Perkin Elmer DRC II” model inductively coupled plasma-mass spectrometer (ICP-MS). Crystal structures of the catalysts are identified by Rigaku D-Max 2200 model X-ray Diffraction (XRD) instrument with Cu X-ray radiation at 40 kV and 30 mA with scan speed of 2 degrees/min. Microstructures of the powdered catalyst slurries are imaged by a JEOL JEM 2100F model High Resolution Transmission Electron Microscope (HRTEM) operating at 200 kV. Also an elemental analysis is made by Energy Dispersive X-ray

(EDX) coupled with TEM. Surface area measurements are carried out by a Quantachrome Corporation, Autosorb-6 model BET instrument. Prior to determination of an adsorption isotherm, the sample was degassed at 200°C for 2 h.

3.4. Catalytic Activity Tests

A dynamic test system specially constructed for simulating the operating conditions of the automobile is used to perform catalytic activity tests. Performance of a TWC is evaluated according to percent conversion of the pollutant gases and the corresponding temperatures. For simulation of the exhaust gases, a mixture of gases are fed to the reactor containing the monolithic catalyst inside. The reactor is dynamically heated and cooled back, similar to automobile engines. Temperature control is adjusted by a thermocouple placed at entrance of the monolith. Dynamical test system is coupled with a mass spectrometer (MS) and a CO analyzer for instant analysis of the gases exiting the reactor. Temperature and conversion data are used in evaluation of the catalytic performance.

3.4.1. Dynamic Activity Test System

Dynamic test system (illustrated in Figure 4) is consisted of a gas flow control and conditioning unit, a split furnace, a quartz reactor and a Hiden HPR-20 Q/C model Mass Spectrometer (MS) and Teledyne model 7600 non-dispersive infrared CO Analyzer. For simulation of the exhaust gases exiting from gasoline vehicles, five gas cylinders are used and a simulating gas mixture is obtained. Gas Hourly Space Velocity (GHSV) of the simulated exhaust gas is adjusted to be 50000 h⁻¹. The first cylinder contains C₃H₆ (0.33 %), C₃H₈ (0.11 %), CO (8.87 %), H₂ (88.65) and balance CO₂. Composition of the first cylinder is determined in a way to satisfy the final composition of the simulating exhaust mixture. In the second cylinder, NO and N₂ are present in equal amounts. Third cylinder contains 100 ppm SO₂ with balance N₂. Since NO and SO₂ have corrosive nature, they are diluted in N₂ and accordingly fed to the system with lower flow rates. Fourth cylinder contains pure O₂, and the fifth contains pure N₂. All gases are transported to the system with 1/8 inch Teflon pipes. Flow rates of all five channels are

controlled by mass flow controllers (MFCs). For oxygen oscillation, a separate pipe is used to send the gas directly to the inlet of the reactor. O₂ gas passes through a solenoid valve operating at a frequency of 1 Hz and a reducer regulates the flow rate. In order to simulate the 10 % water vapor in the exhaust composition, N₂ gas coming from the fifth chamber passes through a water bath kept at 55°C and carries the water vapor to the system. Gases coming from the first four cylinders are mixed in a manifold and at the exit of the manifold, they are combined with saturated N₂ gas. The pipes that carry water vapor are electrically heated to 110°C, in order to prevent condensation of the water vapor. Valve VT6 adjusts the direction of the flow through either reactor or by-pass line. Quartz reactor is vertically placed in the split furnace. It has a quartz cup section in which the monolith is placed and the thermocouple measures the temperature on the top of this section. Temperature control of the furnace is made by thermocouple. A quartz filter is placed at the bottom of the monolithic catalysts to prevent any impurities pass through. Exiting gases are firstly conditioned for removal of water, and then 1L of sample is sent to MS and CO analyzer. Rest of the exiting gases are vented from the system. Data collected by thermocouple, CO analyzer and MS are monitored by MAS-SOFT software program connected to MS.

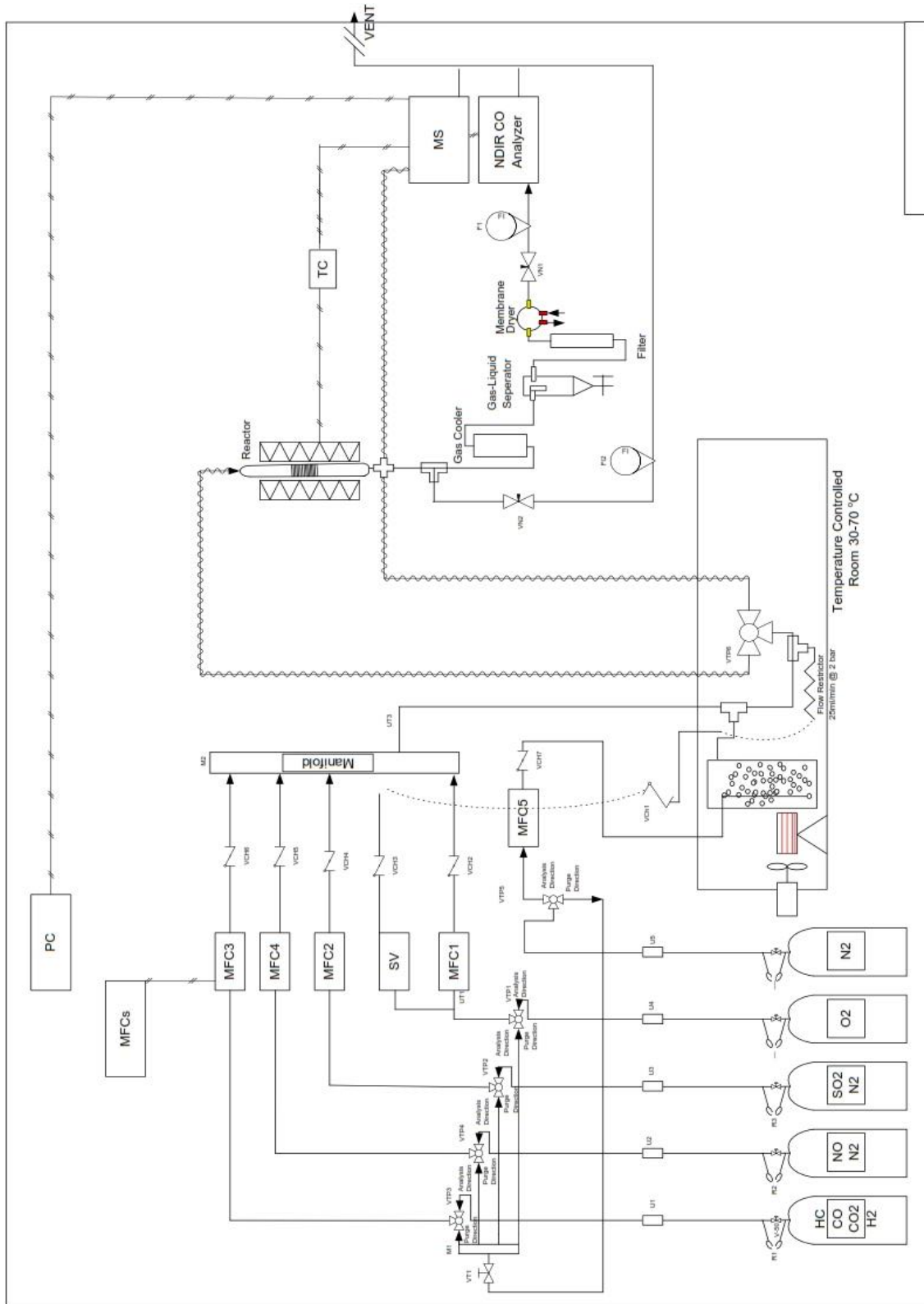


Figure 4 Dynamic activity test system

3.4.2. Catalytic Activity Test Procedure

Activity test starts with placing a laboratory scale sample monolith inside the quartz reactor. The reactor is vertically placed in the split furnace and then, thermocouple is placed inside the flat quartz pipe on the top of the monolith. After mass flow controller unit is started, gas cylinders are opened and flow is passed through the by-pass line. During that time, MS-SOFT starts collecting simultaneous data from CO analyzer, MS, and thermocouple every 40 s and monitors the data on the computer. Once the flow rates are stabilized, concentrations are noted as initial concentrations and VT6 valve is adjusted to change the direction of flow to the reactor. Also, solenoid valve of is opened to start oxygen oscillation between oxidizing and reducing conditions. At the same time, oven is switched on and the reactor is heated up to 600°C with a heating rate of 5 °C/min. After 600°C is achieved, reactor is cooled down by natural convection. Raw data collected by the software is converted to conversion versus temperature plots using MS calibration equations for each species, individually. Simulated exhaust gas mixture compositions are for the tests with and without SO₂ are given in Table 6-7. In Appendix C, calculations for the exhaust gas mixture composition, flow rates of the individual species and a sample catalytic activity analysis are given.

Table 6 Composition of simulated exhaust gas mixture feed with SO₂

Species	Gas Mixture Composition (%)		
	Reducing	Stoichiometric	Oxidizing
H ₂	0.231	0.230	0.230
CO	1.002	1.001	0.999
C ₃ H ₆	0.037	0.037	0.037
C ₃ H ₈	0.012	0.012	0.012
CO ₂	10.018	10.000	9.981
NO	0.150	0.150	0.150
SO ₂	0.002	0.002	0.002
O ₂	0.585	0.767	0.949
N ₂	Balance	Balance	Balance

Table 7 Composition of simulated exhaust gas mixture feed without SO₂

Species	Gas Mixture Composition (%)		
	Reducing	Stoichiometric	Oxidizing
H ₂	0.231	0.230	0.230
CO	1.002	1.001	0.999
C ₃ H ₆	0.037	0.037	0.037
C ₃ H ₈	0.012	0.012	0.012
CO ₂	10.018	10.000	9.981
NO	0.150	0.150	0.150
SO ₂	0.000	0.000	0.000
O ₂	0.585	0.767	0.949
N ₂	Balance	Balance	Balance

3.4.3. Calibrations of Mass Spectrometer

Data collected by MS is in terms of pressure, therefore calibration is necessary in order to obtain accurate data for the concentration of the species in the simulating exhaust gas mixture. Calibrations are performed for O₂, H₂, C₃H₆, C₃H₈, NO and SO₂ gases. No calibration is made for CO since CO analyzer gives the data in ppm units. Throughout calibration process, gases are passed through the by-pass line and furnace is not heated. The calibration gas mixture is consisted of the gas to be calibrated, nitrogen and water vapor. In order to obtain the total GHSV used in catalytic activity tests, nitrogen is sent using two lines. In order to keep the total flow rate constant, flow rate of the nitrogen gas containing water vapor is kept constant during calibration process, and the flow rate of the additional nitrogen line is adjusted according to the flow rate of the calibrated gas. At varying flow rates, concentrations of each species are calculated using the compositions of the gas cylinders. Calculated concentrations are plotted versus MS signals and calibration equations are generated. Calibration data and plots are given in Appendix D.

3.5. Computational Method

3.5.1. Vienna Ab Initio Simulation Package (VASP)

In this study, all quantum mechanical calculations were performed via Vienna Ab Initio Simulation Package (VASP) software. VASP code was developed by George Kresse, Jungen Furthmüller and their team members in University of Vienna (Kresse & Furthmüller, 1996; Kresse & Hafner, 1994). Density Functional Theory (DFT) method is implemented in the VASP script in order to obtain information for any system of interest. The code employs DFT method in a periodical manner and treats a given unit cell as an infinite system. Figure 5 illustrates the unit cell of bulk CeO₂ structure and its periodical repetition in x and y directions during VASP calculations.

VASP script uses plane wave basis set and pseudopotentials for quantum mechanical calculations and in two loops. In one of these loops, Kohn-Sham equations are solved for the energies and forces of a given system. The other loop is responsible for calculations of the ionic movements and geometric optimizations. The code used in this study also includes Projector Augmented Wave (PAW) method for electron ion interactions and Generalized Gradient Approximations (GGA) to compute exchange and correlation energy with supercell approach (Blöchl, 1994; Perdew 1992). K-point mesh created with Monkhorst-Pack is selected as (19 x 19 x 19) for bulk optimizations, (4 x 4 x 1) for surface optimizations and (1 x 1 x 1) for gas phase molecule optimizations. Convergence criterion is chosen as 0.015 eV/Å net force acting on each ion and energy cut-off value is selected to be 500 eV for all calculations.

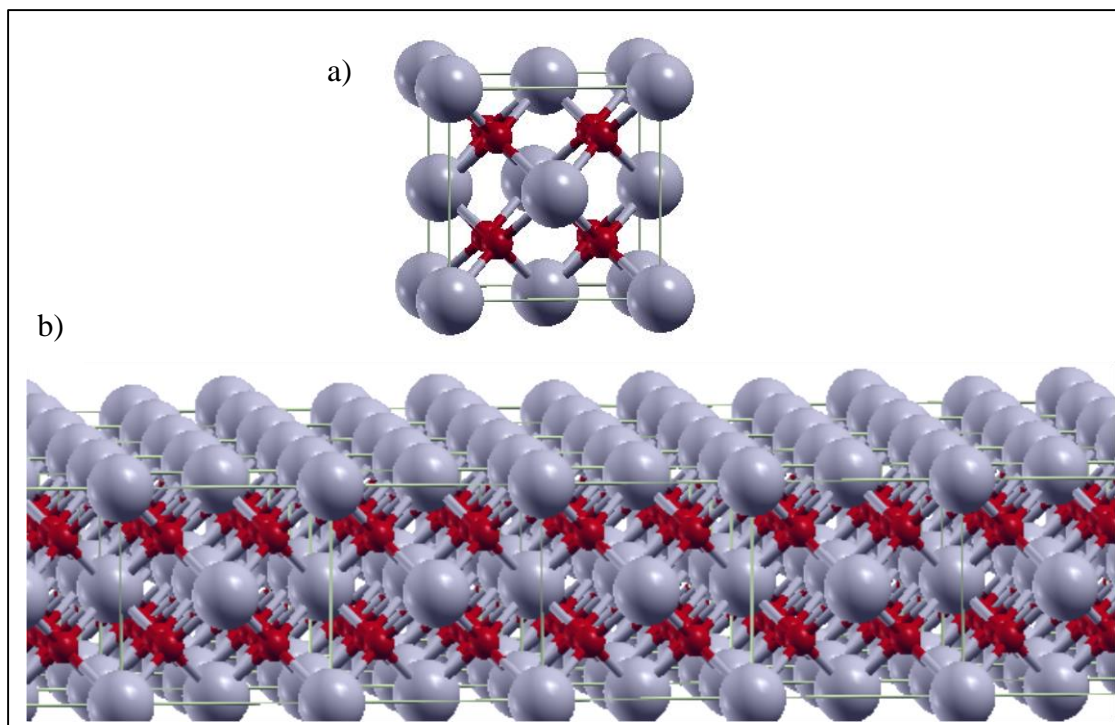


Figure 5 a) Bulk CeO₂ unit cell b) Periodically repeated CeO₂ bulk unit cell

3.2.1. Computational Modelling Procedure

In this study, metal substituted Ce_{0.75}Zr_{0.25}O₂ (110) surfaces and CO oxidation mechanisms on these surfaces were modelled with DFT methods using VASP software. Initially, bulk CeO₂ was optimized using the lattice parameter reported in the literature. In order to obtain a lattice parameter for Ce_{0.75}Zr_{0.25}O₂ (CZO) support structure, one out of four Ce atoms was replaced with a Zr atom and bulk optimization was performed. After obtaining the optimized lattice parameters, CeO₂ (110) surface was cleaved and 20 Å vacuum space was added on top of the surface to avoid any interaction. Surface slab having four layer of Ce atoms was constructed with (3x2) supercells. To obtain Ce_{0.75}Zr_{0.25}O₂ stoichiometry, one of the Ce atoms in each layer was replaced with a Zr atom. Substitution of Mn, Pd and Rh atoms was made in the same manner, one or two Ce atoms on the top layer were replaced with metal atoms and further optimized. Atoms

at the bottom layer were kept fixed for representation of a bulk catalyst surface structure while the atoms in remaining layers were fully relaxed.

After the optimization of surface models were finished, CO oxidation mechanism steps were computed on the surfaces. Gas phase CO and O₂ reactant molecules and CO₂ product molecule were optimized in a 10Å x 10Å x 10Å vacuum cell. Relative energy of each reaction step was calculated with the expression below:

$$E_{rel} = E_{system} - (E_{surface} + \sum E_{reactants}) \quad (3.1)$$

Where E_{system} is the energy of the overall molecular system, $E_{surface}$ is the optimized surface energy and $E_{reactants}$ are energies of the optimized gas phase reactants. For predicting activation barriers and transition state geometries, climbing nudge elastic band (CI-NEB) method was implemented with approximate transition state (ATS) structures. Sample input file scripts are given in Appendix A.

CHAPTER 4

MODELLING THREE WAY CATALYSTS WITH DFT METHODS

4.1. Bulk Structure Optimization

Cerium oxide (CeO_2) is a rare earth oxide having the fluorite (CaF_2) structure with space group $\text{Fm}\bar{3}\text{m}$ and consisted of cubic closed-packed metal atoms with oxygen atoms filling all tetrahedral holes (Trovarelli, 1996; Sebastian, 2008). Lattice parameter of the CeO_2 crystal is found to be 5.411 Å with experimental studies (Gerward & Olsen, 1993). Calculations for bulk relaxation of CeO_2 yielded a lattice parameter of 5.464 Å which is in accordance with the experimental value. Bond lengths of Ce-Ce and Ce-O bonds were obtained as 3.86 Å and 2.36 Å, respectively. Computations for $\text{Ce}_{0.75}\text{Zr}_{0.25}\text{O}_2$ resulted in a smaller lattice parameter of 5.380 Å. An approximate value for lattice constant of $\text{Ce}_{0.75}\text{Zr}_{0.25}\text{O}_2$ was previously reported as 5.39 Å (Yang, et al., 2008). Surface strain caused by Zr substitution is responsible for the contraction of the crystal and decrease in the lattice parameter (Wang, et al., 2009). Optimized bulk unit cells of CeO_2 and $\text{Ce}_{0.75}\text{Zr}_{0.25}\text{O}_2$ are shown in Figure 6.

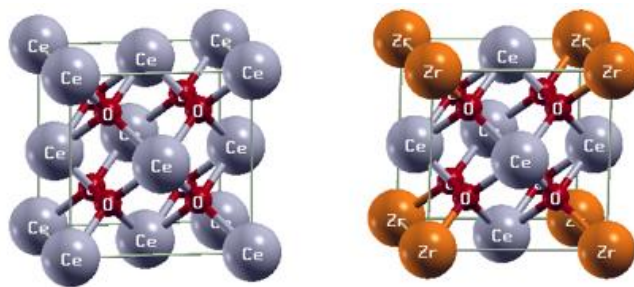


Figure 6 Relaxed bulk unit cells of (a) CeO_2 (b) $\text{Ce}_{0.75}\text{Zr}_{0.25}\text{O}_2$

4.2. Surface Slab Optimization

According to the findings of Gerceker & Önal (2013), (110) surface of CeO_2 and $\text{Ce}_{0.75}\text{Zr}_{0.25}\text{O}_2$ was found to be the most stable surface with the lowest formation energy among (100) and (111) surfaces. Therefore, (110) surface was chosen as the sample surface for computations. By using the lattice parameter of the relaxed $\text{Ce}_{0.75}\text{Zr}_{0.25}\text{O}_2$ bulk structure, surface is cleaved and optimized. Top and side views of the optimized $\text{Ce}_{0.75}\text{Zr}_{0.25}\text{O}_2$ (110) surface slab is shown in Figure 7.

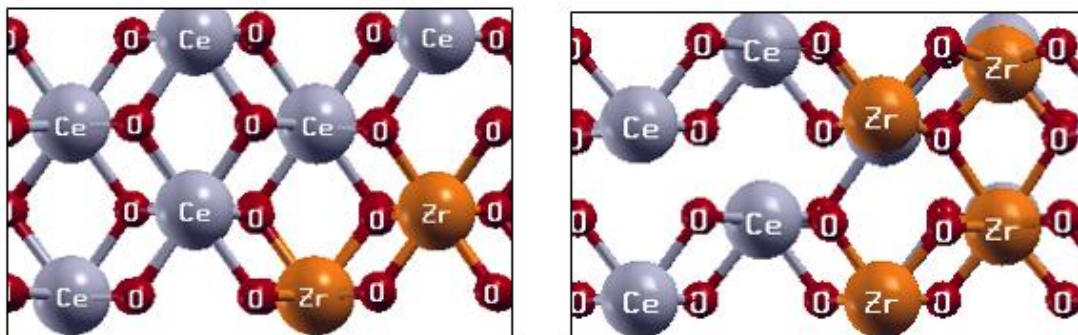


Figure 7 (a) Top and (b) Side view of $\text{Ce}_{0.75}\text{Zr}_{0.25}\text{O}_2$ (110) surface

4.3. Metal Substitution on $\text{Ce}_{0.75}\text{Zr}_{0.25}\text{O}_2$ (110) Surface

Effect of Mn doping on catalytic activity was investigated with three different surface models labelled as; (A)- $\text{Mn}/\text{Ce}_{0.75}\text{Zr}_{0.25}\text{O}_2$, (B)- $\text{Mn}+\text{Pd}/\text{Ce}_{0.75}\text{Zr}_{0.25}\text{O}_2$ and (C)- $\text{Mn}+\text{Rh}/\text{Ce}_{0.75}\text{Zr}_{0.25}\text{O}_2$. For atomic substitution, one or two cerium atoms on the top layer were replaced with Mn, Pd or Rh. On surfaces with bi-metallic substitution, both metals were placed in sites near Zr atoms, but not in direct contact with each other. Top views of these surfaces are given in Figure 8.

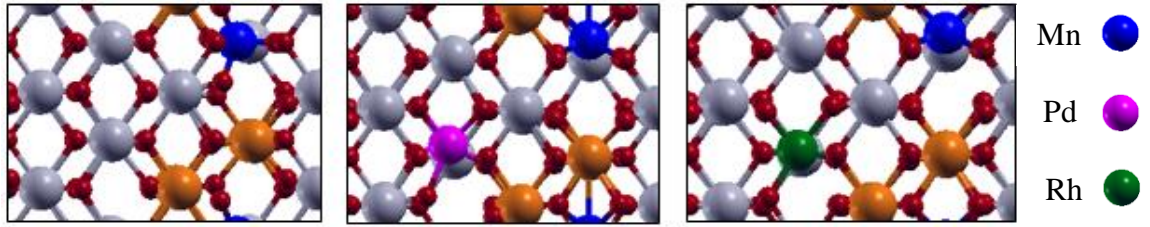


Figure 8 Top views of doped surfaces (a) Mn/Ce_{0.75}Zr_{0.25}O₂, (b) Mn+Pd/Ce_{0.75}Zr_{0.25}O₂ and (c) Mn+Rh/Ce_{0.75}Zr_{0.25}O₂

Energy change due to atomic substitution on the surface is calculated with Equation 4.1

$$\Delta E_{substitution} = (E_{M-surface} + E_{Ce\ atom(s)}) - (E_{surface} + E_M) \quad (4.1)$$

where $E_{M-surface}$ is the optimized energy of the doped surface, $E_{surface}$ is the energy of the optimized bare surface, $E_{Ce\ atom}$ and E_M are the energies of a cerium atom(s) and dopant metal atom(s), respectively. Energy changes of metal substituted surfaces with respect to bare CZO surface are listed in Table 8.

Table 8 Change of energies due to atomic substitution on surfaces

Surface	Energy (kcal/mole)
(A)-Mn/Ce _{0.75} Zr _{0.25} O ₂	102.187
(B)-Mn+Pd/Ce _{0.75} Zr _{0.25} O ₂	385.649
(C)-Mn+Rh/Ce _{0.75} Zr _{0.25} O ₂	307.722

Mn has a similar atomic structure to Ce and Zr atoms, therefore doping CZO with a single Mn atom does not require a high energy. However, in the case for bi-metallic substitutions, energy requirements are higher. Between the two noble metal containing surfaces, Rh substituted surface is energetically more favorable.

4.4. Modelling of CO Oxidation Mechanism

Once the optimized structures of surface models were obtained, CO oxidation mechanisms and energetics on these surfaces were studied in detail. A previous study

upon CO oxidation mechanisms on Pd and Rh substituted $\text{Ce}_{0.75}\text{Zr}_{0.25}\text{O}_2$ surfaces were reported by Gerceker & Önal, (2013). In this study, using the same computational tools and methodology, effect of Mn doping on noble metal (Pd and Rh) containing CZO was investigated. Therefore, outcomes of this study were compared with the previously reported findings for Pd and Rh substituted CZO, for comprehension of any contribution that Mn doping may procure on catalytic activity.

4.4.1. CO Oxidation on (A)-Mn/Ce_{0.75}Zr_{0.25}O₂ Surface

Initially, as an attempt to investigate whether Mn-doped CZO surface is capable of CO conversion or not, computations for CO oxidation on surface (A)-Mn/Ce_{0.75}Zr_{0.25}O₂ were performed. Energies of each step were calculated relative to (A)-Mn/Ce_{0.75}Zr_{0.25}O₂ surface energy. Elementary reaction steps and relative energies of CO oxidation mechanism on (A)-Mn/Ce_{0.75}Zr_{0.25}O₂ surface are given in Table 9.

Table 9 Reaction scheme and relative energies of CO oxidation steps on the surface (A)-Mn/Ce_{0.75}Zr_{0.25}O₂

Reaction Step	Relative Energy (kcal/mole)
A_R1 $\text{CO}_{(\text{g})} \rightarrow \text{CO}_{(\text{ads})}$	-36.501
A_R2 $\text{CO}_{(\text{ads})} \rightarrow \text{CO}_{2(\text{ads})} + \text{O}_{\text{vac}} \rightarrow \text{CO}_{2(\text{g})}$	-30.017
A_R3 $\text{O}_{2(\text{g})} + \text{O}_{\text{vac}} \rightarrow \text{O}_{2(\text{ads})}$	-83.135
A_R4 $\text{CO}_{(\text{g})} + \text{O}_{2(\text{ads})} \rightarrow \text{CO}_{2(\text{ads})}$	-183.388
A_R5 $\text{CO}_{2(\text{ads})} \rightarrow \text{CO}_{2(\text{g})}$	-185.331

CO oxidation on surface A begins with introduction of a CO molecule in gas phase into the system. CO is adsorbed on Mn atom with an adjacent surface oxygen, exothermically. Adsorption of CO molecule releases approximately 28 kcal/mole energy. Extracting a surface oxygen atom, CO is spontaneously desorbed from the surface as CO₂ and an oxygen vacancy is created on the surface. CI-NEB analysis was performed to see if there is an activation barrier between CO adsorption and CO₂ steps, however no barrier was found. Optimized geometries of the gas phase CO approaching

the surface, adsorption of CO and CO₂ desorption are shown in Figure 9 with labels of A1, A2 and A3, respectively.

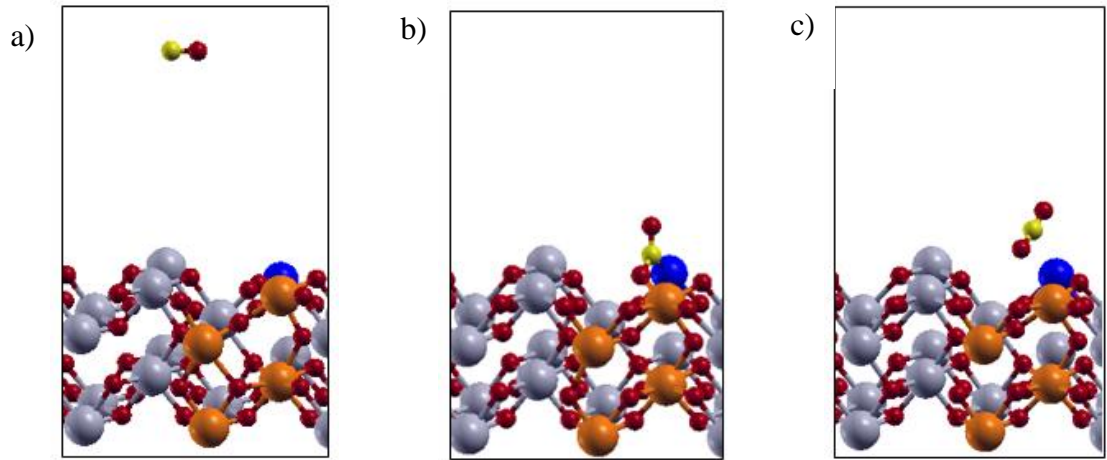


Figure 9 (a) A1 - CO molecule in the gas phase (b) A2 - Adsorbed CO molecule (c) A3 - CO₂ desorption and creation of an oxygen vacancy

CO₂ molecule is then released to gas phase and energy requirement for oxygen vacancy formation E_{vac} is computed with the following equation

$$E_{vac} = \left(E_{vac+surface} + \frac{1}{2} E_{O_2} \right) - E_{surface} \quad (4.2)$$

where $E_{vac+surface}$ is the energy of the surface after CO₂ desorption and $E_{surface}$ is the energy of bare Mn/Ce_{0.75}Zr_{0.25}O₂ surface. Using equation 4.2, oxygen vacancy formation energy was calculated as 59.83 kcal/mole. The vacant oxygen site is then filled with a gas phase O₂ molecule approaching the surface and adsorbing on the vacant site. Adsorption of O₂ released an energy of approximately 46 kcal/mole. Optimized configurations of gas phase CO₂ molecule, gas phase O₂ approaching to the surface and adsorption of O₂ on the vacant site are labelled as A4, A5 and A6, respectively and shown in Figure 10.

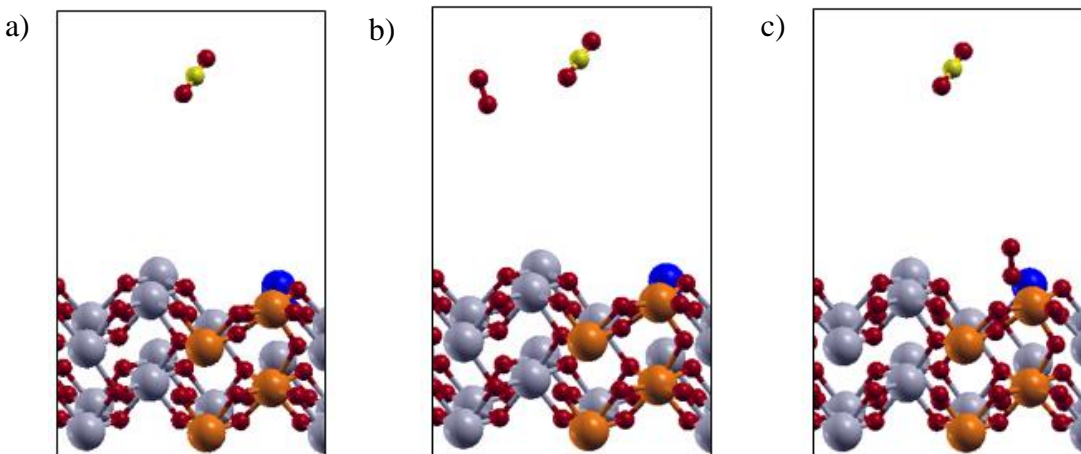


Figure 10 (a) A4 - CO₂ molecule in the gas phase (b) A5 - Approaching gas phase O₂ molecule (c) A6 - Adsorption of O₂ on the vacant site

Following, another gas phase CO molecule approaches to the surface, interacts with the upper oxygen atom and breaks the O₂ molecule in the steps labelled as A7 and A8, respectively. Afterwards, CO₂ is spontaneously desorbed from the surface with an energy release of 100 kcal/mole and this step is labelled as A9. Hereby, surface is regenerated with the formation of the second CO₂ molecule. Optimized geometries A7, A8 and A9 are shown in Figure 11 and overall energy profile is plotted in Figure 12.

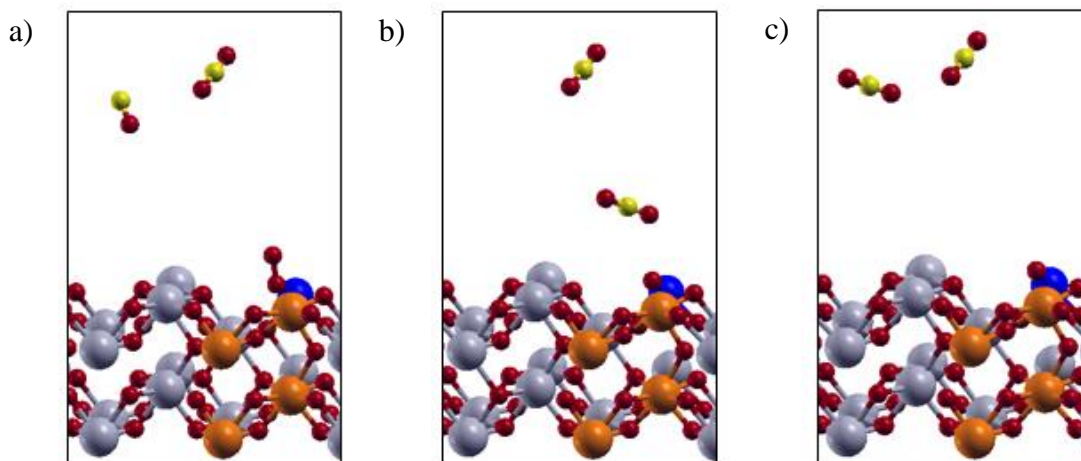


Figure 11 (a) A7 - Gas phase CO molecule approaching the surface (b) A8 - CO₂ desorption from the surface (c) A9 - CO₂ molecule in the gas phase

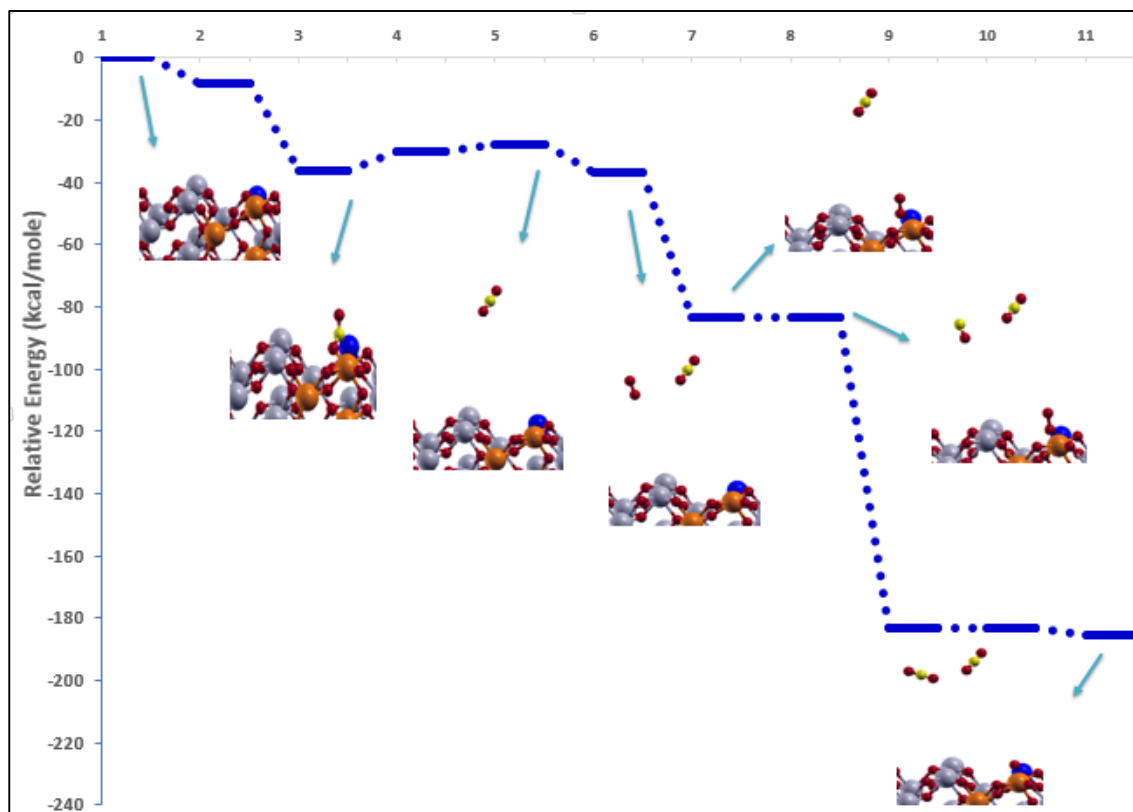


Figure 12 Relative energy profile of CO oxidation mechanism on (A)-Mn/Ce_{0.75}Zr_{0.25}O₂ surface

As a results, two CO molecules are oxidized to two CO₂ molecules exothermically by using surface oxygen on Mn doped Ce_{0.75}Zr_{0.25}O₂ surface, indicating that Mn-doped CZO solely is capable of CO conversion. Regeneration of the surface indicates that the surface has the ability of oxygen storage and release. In other words, OSC property of CZO was proved.

4.4.2. CO Oxidation on (B)-Pd+Mn/Ce_{0.75}Zr_{0.25}O₂ Surface

For investigating if any contribution is provided by Mn doping to Pd-CZO catalyst, CO oxidation mechanism was computed on surface (B)-Pd+Mn-Ce_{0.75}Zr_{0.25}O₂. Energies of each step were calculated relative to (B)-Pd+Mn/Ce_{0.75}Zr_{0.25}O₂ surface energy. Elementary reaction steps and relative energies of CO oxidation mechanism on (B)-Pd+Mn/Ce_{0.75}Zr_{0.25}O₂ surface are given in Table 10.

Table 10 Reaction scheme and relative energies of CO oxidation steps on the surface (B)-Pd+Mn/Ce_{0.75}Zr_{0.25}O₂

Reaction Step	Relative Energy (kcal/mole)
B_R1 CO _(g) → CO _(ads)	-103.718
B_R2 CO _(ads) → CO _{2(ads)} + O _{vac} → CO _{2(g)}	-99.569
B_R3 O _{2(g)} + O _{vac} → O _{2(ads)}	-112.937
B_R4 CO _(g) + O _{2(ads)} → CO _{2(ads)}	-176.719
B_R5 CO _{2(ads)} → CO _{2(g)}	-174.250

CO oxidation begins with a gas phase CO molecule approaching the surface. CO interacts with the surface oxygen atom in between Pd-Zr atoms and spontaneously desorbs as CO₂ molecule from the surface by creating an oxygen vacancy. In order to see if there is an activation barrier for this step, CI-NEB analysis was computed however no activation barrier was encountered. Gerceker and Önal (2013) reported an activation barrier of 45 kcal/mole between steps of CO adsorption and CO₂ desorption on the Pd-Ce_{0.75}Zr_{0.25}O₂ surface. Therefore, it can be inferred that by virtue of Mn doping, activation barrier of CO₂ desorption was overcome. Desorption of CO₂ molecule releases an energy of approximately 103 kcal/mole. CO₂ is then released to gas phase. Optimized geometries of gas phase CO molecule approaching the surface, CO₂ desorption from the surface and gas phase CO₂ molecule are shown in Figure 13 with labels of B1, B2 and B3, respectively.

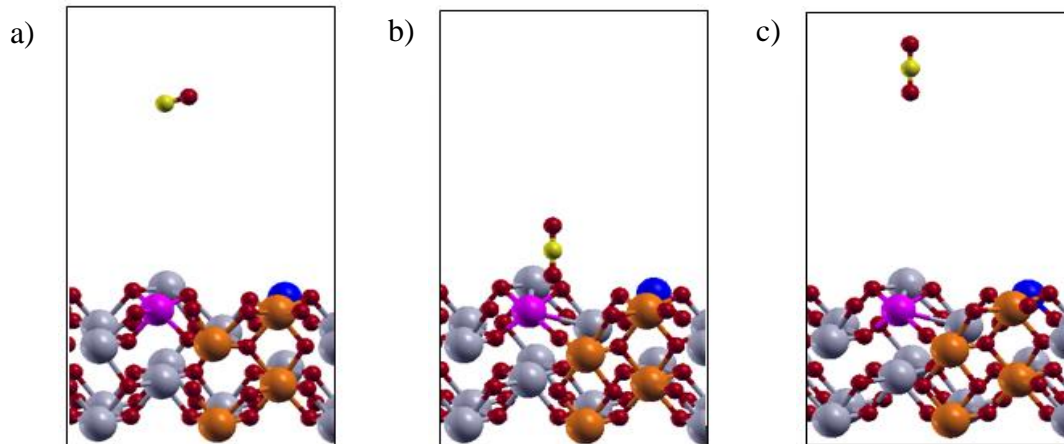


Figure 13 (a) B1 - Gas phase CO molecule approaching the surface (b) B2 - CO₂ desorption from the surface and creation of oxygen defect (c) B3 - CO₂ molecule in the gas phase

Calculation of oxygen vacancy formation energy gave a negative value of -12.09 kcal/mole. Energy of oxygen vacancy formation on Pd-Ce_{0.75}Zr_{0.25}O₂ was reported as 43.7 kcal/mole (Gerçeker & Önal, 2013), indicating that incorporation of both Pd and Mn in CZO substantially enhances the OSC property of CZO. Vacant site is occupied by an O₂ molecule with an energy release of approximately 16 kcal/mole. Optimized geometries of gas phase O₂ molecule approaching the surface and adsorption of O₂ molecule on the surface are shown in Figure 14 with labels of B4 and B5, respectively.

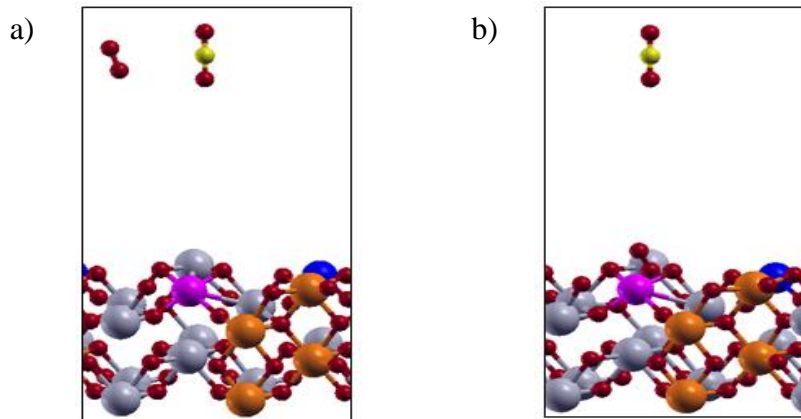


Figure 14 (a) B4 - Gas phase O_2 molecule approaching the surface (b) B5 - Adsorption of O_2 molecule on the vacant site

In the following steps, second gas phase CO molecule approaches the surface and interacts with the upper atom of the adsorbed oxygen molecule. Spontaneously, CO_2 is formed and desorbed from the surface with an energy exchange of approximately 64 kcal/mole. CO_2 molecule is then released into gas phase. Optimized configurations of approaching CO gas phase molecule, adsorption and desorption of CO and gas phase CO_2 molecule are shown in Figure 15 with labels of B6, B7 and B8, respectively. Overall energy profile of CO oxidation is given in Figure 16.

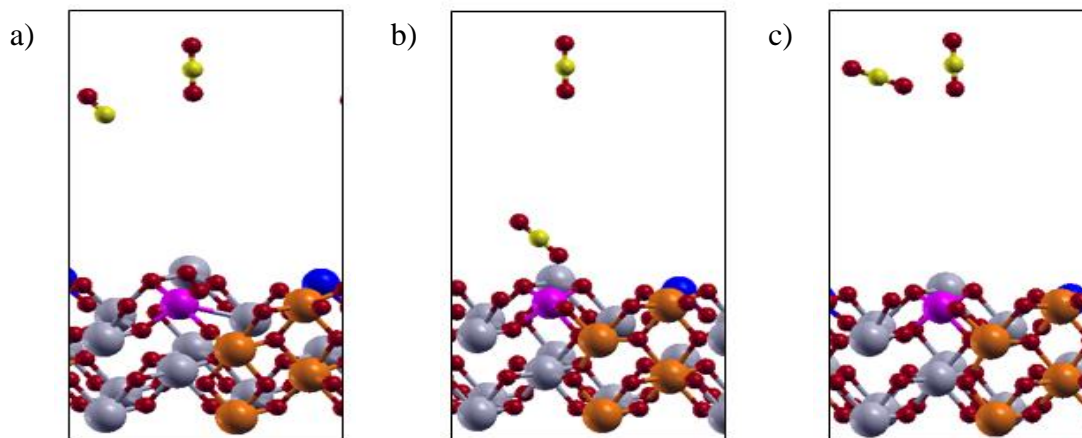


Figure 15 (a) B6 - Gas phase CO molecule approaching the surface (b) B7 - Desorption of CO_2 molecule from the surface (c) B8 - CO_2 molecule in the gas phase

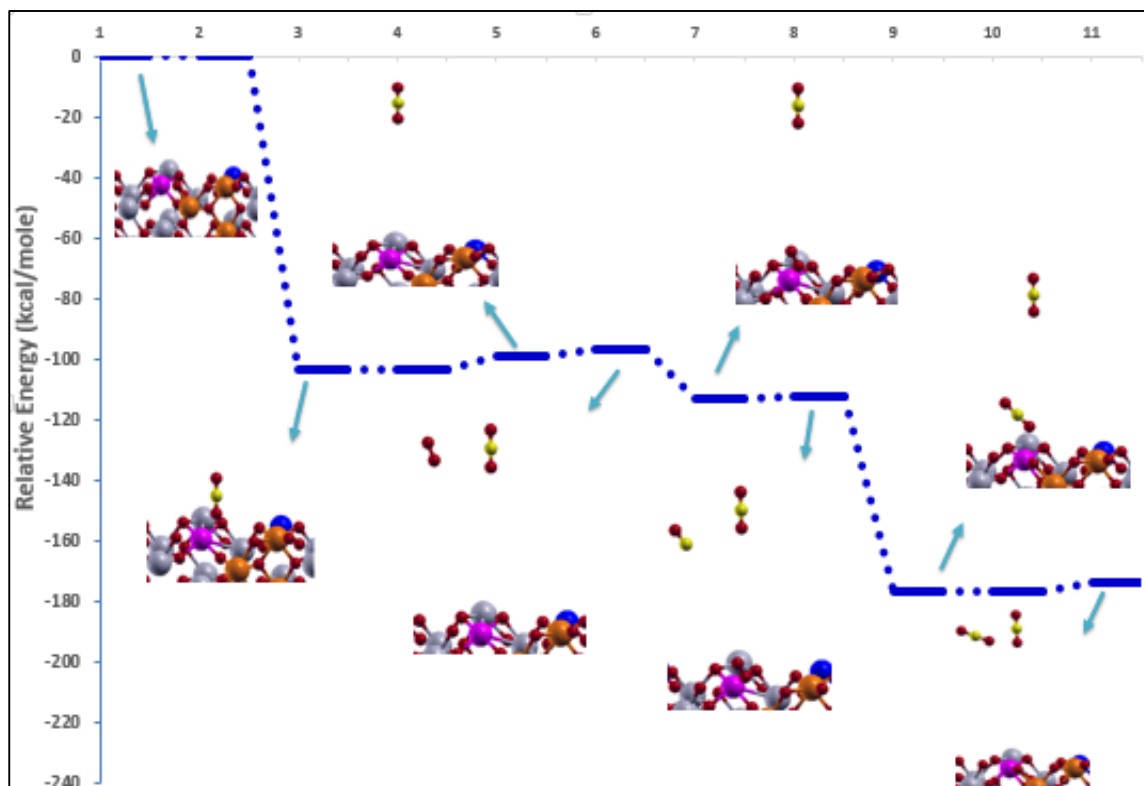


Figure 16 Relative energy profile of CO oxidation mechanism on (B)-Pd+Mn/Ce_{0.75}Zr_{0.25}O₂ surface

Using the surface oxygen, two CO molecules are exothermically converted to CO₂ on (B)-Pd+Mn/Ce_{0.75}Zr_{0.25}O₂ surface. Oxygen release and storage capability was proven with the regeneration of surface after the formation of second CO₂ molecule.

Contribution of Mn doping on catalytic activity was revealed with the enhancement of the OSC property. Apparently, a synergism between Pd and Mn dopants leads to large structural distortions and creates weaker oxide ions on the ceria lattice. Improved reducibility of Pd and Mn doped ceria was confirmed with the OSC measurement results of Gupta et al. (2010). In addition, activation barrier for the adsorption and desorption of the first CO molecule was eliminated with Mn doping on Pd-Ce_{0.75}Zr_{0.25}O₂, probably due to the improvement in OSC component.

4.4.3. CO Oxidation on (C)-Rh+Mn/Ce_{0.75}Zr_{0.25}O₂ Surface

Effect of Mn doping on catalytic activity was further investigated with Rh-CZO in order to see if a synergism between Rh and Mn is also available as in the case with Pd and Mn doping on CZO. Therefore, surface (C) was modelled as identical to surface (B) except for the Rh noble metal substitution instead of Pd. CO oxidation mechanism energetics were investigated and energies of each step were calculated relative to (C)-Rh+Mn/Ce_{0.75}Zr_{0.25}O₂ surface energy. Elementary reaction steps and relative energies of CO oxidation mechanism on (C)-Rh+Mn/Ce_{0.75}Zr_{0.25}O₂ surface are given in Table 11.

Table 11 Reaction scheme and relative energies of CO oxidation steps on the surface (C)-Rh+Mn/Ce_{0.75}Zr_{0.25}O₂

Reaction Step	Relative Energy (kcal/mole)
C_R1 CO _(g) → CO _(ads)	-32.481
C_R2 CO _(ads) → CO _{2(ads)} + O _{vac} → CO _{2(g)}	-67.959
C_R3 O _{2(g)} + O _{vac} → O _{2(ads)}	-83.109
C_R4 CO _(g) + O _{2(ads)} → CO _{2(ads)}	-164.009
C_R5 CO _{2(ads)} → CO _{2(g)}	-164.163

Catalytic cycle begins with a gas phase CO molecule approaching the surface and adsorbing on the Rh atom with a neighboring oxygen. Energy release for CO adsorption was found to be approximately 31 kcal/mole. CO is then desorbed from the surface as CO₂, creating an oxygen defect. Desorption step releases an energy of 43 kcal/mole. No activation barrier was found between these steps with CI-NEB analysis. Optimized geometries of gas phase CO molecule, adsorption of CO on the surface and CO₂ desorption are labelled as C1, C2 and C3, respectively and shown in Figure 17.

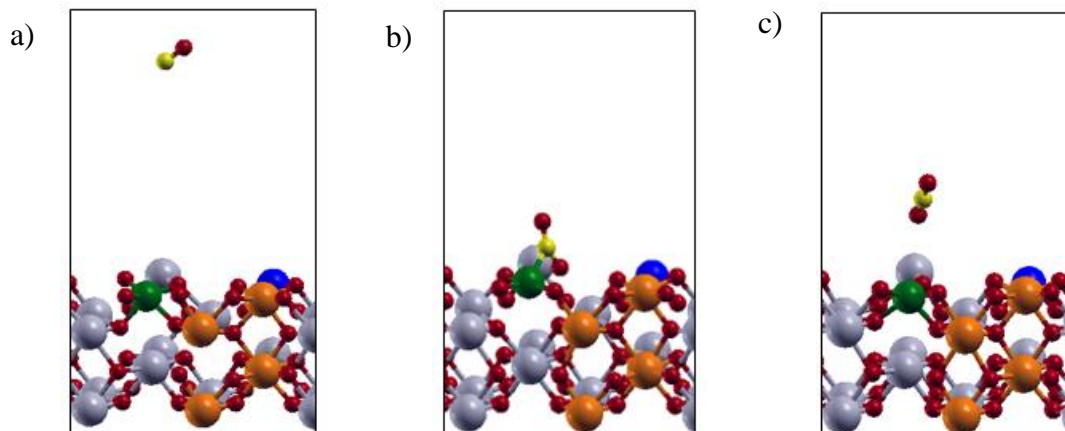


Figure 17 (a) C1 - CO molecule in the gas phase (b) C2 - Adsorbed CO molecule (c) C3 - CO₂ desorption and creation of an oxygen vacancy

CO₂ is then released into gas phase with the step labelled as C4. Energy for oxygen vacancy formation was calculated as 19.51 kcal/mole which is much higher than the oxygen vacancy formation of surface (B). The vacant oxygen site was occupied with an oxygen molecule approaching from the gas phase (step labelled as C5) and adsorbing on the vacant site (step labelled as C6) with an energy release of approximately 19 kcal/mole. Optimized geometries of C4, C5 and C6 steps are shown in Figure 18.

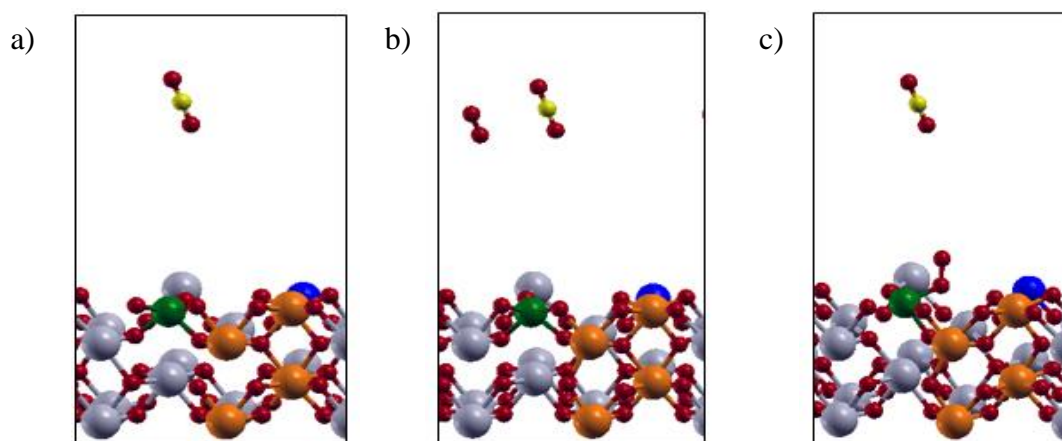


Figure 18 (a) C4 - CO₂ molecule in the gas phase (b) C5 - Gas phase O₂ molecule approaching the surface (c) C6 - Adsorption of O₂ molecule on the vacant site

For completion of the catalytic cycle, another gas phase CO molecule is introduced to the system in the step labelled as C7. CO molecule interacts with the upper atom of the adsorbed oxygen molecule and spontaneously desorbs from the surface as CO₂ with an energy release of approximately 76 kcal/mole in the step labelled as C8. CO₂ is then released into gas phase in the step labelled as C9. Optimized configurations of C7, C8 and C9 are shown in Figure 19 and overall reaction profile of CO oxidation on surface is displayed in Figure 20.

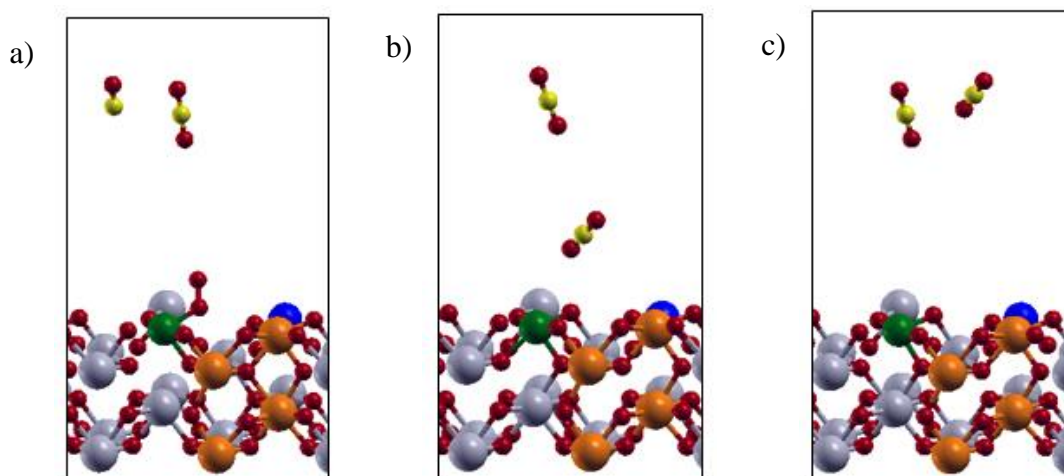


Figure 19 (a) C7 - Gas phase CO molecule approaching the surface (b) C8 - Desorption of CO₂ molecule from the surface (c) C9 - CO₂ molecule in the gas phase

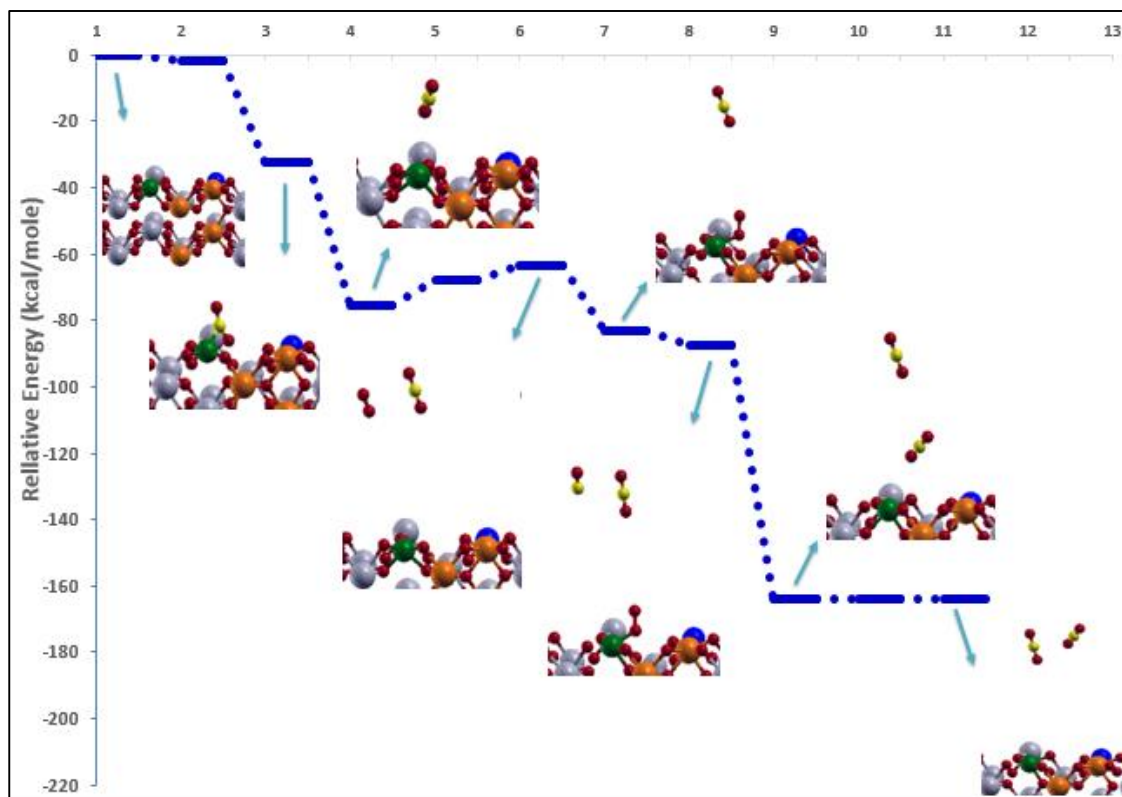


Figure 20 Relative energy profile of CO oxidation mechanism on (C)-Rh+Mn/Ce_{0.75}Zr_{0.25}O₂ surface

As it can be seen on the relative energy profile, two CO molecules were exothermically converted to CO₂ on (C)-Rh+Mn/Ce_{0.75}Zr_{0.25}O₂ surface. Oxygen release and storage capability was again proven with the regeneration of surface after the formation of second CO₂ molecule. Gerceker and Önal (2013) reported an activation barrier of 20 kcal/mole between steps of CO adsorption and CO₂ desorption on Rh-Ce_{0.75}Zr_{0.25}O₂ surface. Also, strong attachment of O₂ molecule on the surface disabled the regeneration process with oxidation of a second CO molecule on Rh/CZO surface. Apparently, Mn doping eliminates the activation barrier and also facilitates the second CO₂ formation with regeneration of the surface.

A comparison for the relative energy profiles of CO oxidation mechanisms on all three surfaces is illustrated in Figure 21.

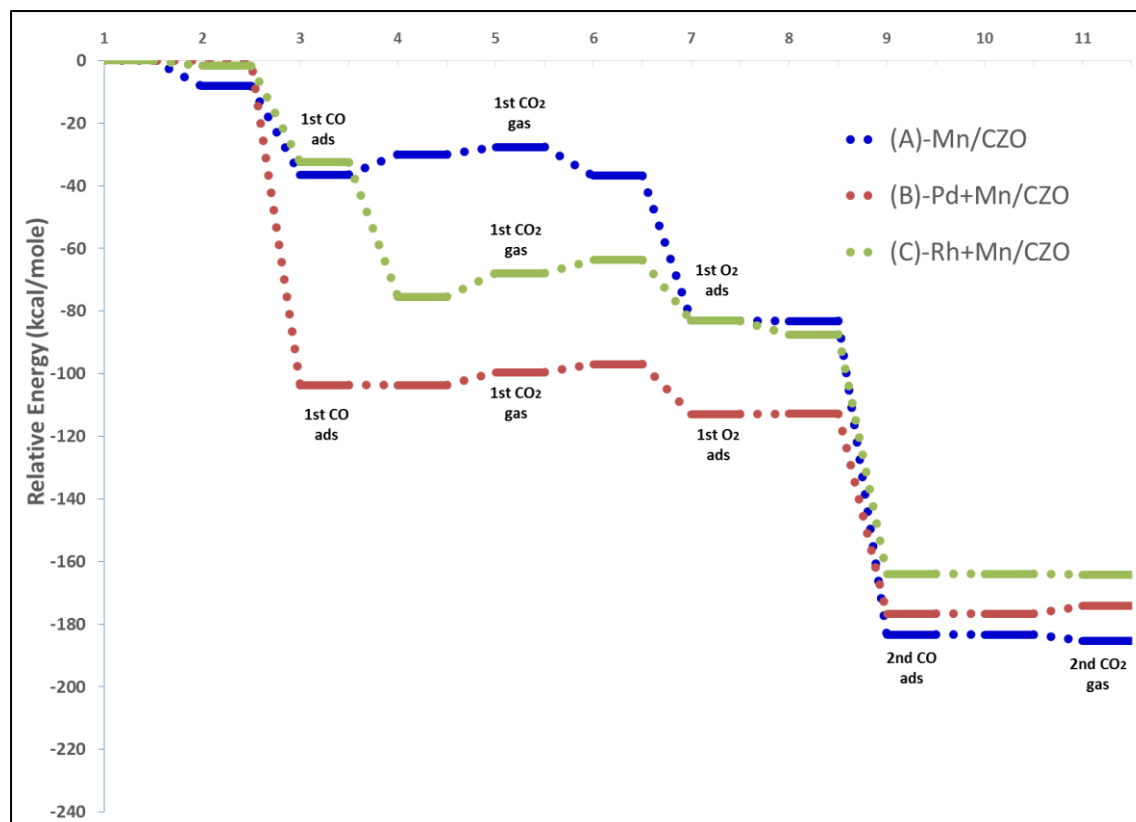


Figure 21 Comparison of the CO oxidation mechanisms on (A)-Mn/CZO, (B)-Pd+Mn/CZO and (C)-Rh+Mn/CZO

Comparison of the energy profiles reveals that CO oxidation is most favored on surface (B)-Pd+Mn/CZO with highest exothermicity on almost all steps. This behavior might be attributed to the enhanced OSC component of ceria due to large structural distortions caused by Pd and Mn doping.

CHAPTER 5

CATALYTIC ACTIVITY TEST RESULTS

In this study, two different methods were employed for the synthesis of three way catalysts. The first one was the impregnation method, in which Pd, Rh and Mn metals were impregnated on the previously synthesized ceria-zirconia mixed oxide at different weight percentages. In the second method named as solution combustion synthesis, metals were substituted in the ceria lattice with different molar ratios. The catalytic activity tests of the monolithic catalysts were evaluated by means of the conversion versus temperature curves of H₂, CO, O₂, C₃H₆ and C₃H₈ species. Performances of the catalysts were interpreted generally in terms of light-off temperature (T₅₀) and maximum conversions of these species. Low T₅₀ and high conversion values indicate good catalytic activity. Catalytic performances were evaluated in terms of two topics; thermal aging and SO₂ exposure. Thermal aging process was applied to catalysts to simulate long term exposure of high temperatures in the automobile exhaust and SO₂ exposure was applied to observe the effect and extent of sulfur poisoning on the catalysts. For each test, two data sets for heating and cooling steps are available, however the cooling step is found to be more trustworthy as the reactor was cooled down by natural convection, steadily. Also, activity curves shift left in the cooling step, probably by virtue of the reduction of the catalyst in the heating step. Therefore, analysis and interpretations regarding catalytic performance were executed based on the activity

data of cooling step. Reproducibility of the activity tests were confirmed in a previous thesis study using the same test system and experimental conditions (Gerceker, 2013).

5.1. Catalysts Synthesized via Impregnation Method

5.1.1. Catalytic Activity Tests of IMP1 Catalyst

First type of impregnated catalyst is IMP1 and was prepared with 0.70 wt % Pd loading on $Ce_{0.8}Zr_{0.2}O_2$. Two laboratory size monoliths were washcoated with the catalyst slurry and named as IMP1-M1 and IMP1-M2. Using the ICP-MS results (see Chapter 6), Pd loadings of IMP1-M1 and IMP1-M2 monolithic catalysts were calculated as 9.57 g/ft³ and 9.25 g/ft³, respectively.

In the first set of tests, IMP1-M1 was used in order to investigate the effect of thermal aging on catalytic activity. In Test 1, fresh IMP1-M1 was tested with simulated exhaust gas feed that does not contain SO₂. After the fresh test, the same monolith was aged at 900°C with dry air and the second test was performed under identical test conditions using the aged monolith. Catalytic activity data of the fresh and aged IMP1-M1 monolith are given in Table 12-13. For a better interpretation of the data, T50 values of the two activity tests of IMP1-M1 monolith were compared in Figure 22. Conversion-temperature profiles of the activity tests with fresh and aged monolithic catalysts are given in Appendix E.

Table 12 Catalytic activity data of IMP1-M1 monolithic catalyst in Test 1 without SO₂ (Fresh Monolith)

Species	Heating			Cooling		
	T50 (C°)	Max. Conv. (%)	Tmax (C°)	T50 (C°)	Max. Conv. (%)	Tmax (C°)
H ₂	281	100	494	219	100	491
CO	245	99	598	244	99	595
O ₂	227	90	598	223	90	595
C ₃ H ₆	223	100	597	223	99	591
C ₃ H ₈	326	100	594	312	99	595

Table 13 Catalytic activity data of IMP1-M1 monolithic catalyst in Test 2 without SO₂ (Monolith aged at 900°C)

Species	Heating			Cooling		
	T50 (C°)	Max. Conv. (%)	Tmax (C°)	T50 (C°)	Max. Conv. (%)	Tmax (C°)
H ₂	180	98	556	209	97	428
CO	244	100	580	228	100	569
O ₂	241	84	595	211	84	589
C ₃ H ₆	206	100	561	228	99	597
C ₃ H ₈	367	77	594	351	80	596

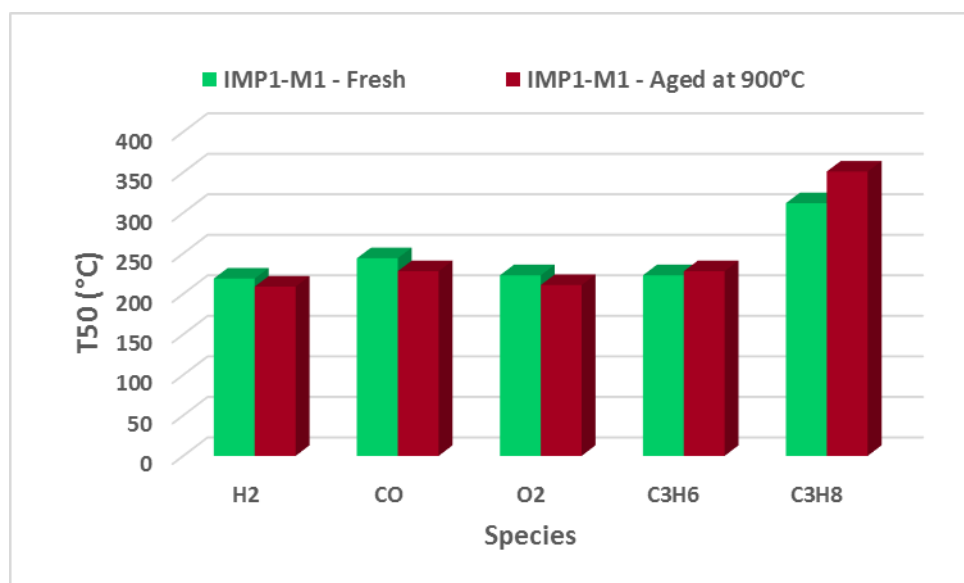


Figure 22 Change in T50 values for IMP1-M1 monolithic catalyst upon Thermal Aging (Tests with no SO₂)

As it can be inferred from the activity data, IMP1-M1 is capable of converting all species at high conversions in both tests. When the activity data of IMP1-M1 monolithic catalyst is evaluated, it was seen that after the monolith was subjected to thermal aging, conversions of H₂, CO and O₂ species were slightly enhanced. On the other hand, C₃H₈ conversion considerably deteriorated upon thermal aging with an increase in the T50 value and a decrease in the maximum conversion. Slight increase in the T50 value of

C₃H₆ conversion indicates that thermal aging does have a high impact on CO conversion.

For a further investigation on the catalytic performance, effect of thermal aging was also investigated with IMP1-M2 in another set of tests using a simulated exhaust gas feed containing SO₂. Catalytic activity data of the fresh and aged IMP1-M2 is given in Table 14-15 and comparison of the T50 of fresh and aged tests are shown in Figure 23. Conversion-temperature profiles of fresh and aged catalytic activity tests are given in Appendix E.

Table 14 Catalytic activity data of IMP1-M2 monolithic catalyst in Test 1 with SO₂ (Fresh Monolith)

Species	Heating			Cooling		
	T50 (C°)	Max. Conv. (%)	Tmax (C°)	T50 (C°)	Max. Conv. (%)	Tmax (C°)
H ₂	272	100	447	270	100	547
CO	327	98	596	288	98	343
O ₂	329	99	596	287	100	379
C ₃ H ₆	274	100	465	270	100	528
C ₃ H ₈	399	93	596	344	95	588

Table 15 Catalytic activity data of IMP1-M2 monolithic catalyst in Test 2 with SO₂ (Monolith aged at 900°C)

Species	Heating			Cooling		
	T50 (C°)	Max. Conv. (%)	Tmax (C°)	T50 (C°)	Max. Conv. (%)	Tmax (C°)
H ₂	320	100	575	283	100	594
CO	326	99	598	300	99	588
O ₂	326	100	594	254	100	501
C ₃ H ₆	253	99	398	272	100	574
C ₃ H ₈	388	94	594	283	100	597

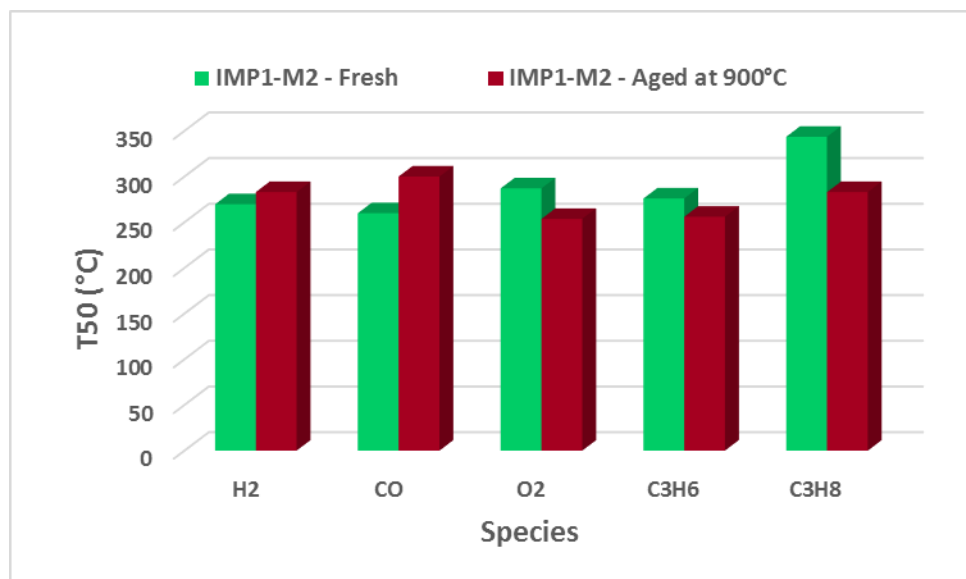


Figure 23 Change in T50 values for IMP1-M2 monolithic catalyst upon Thermal Aging (Tests with SO₂)

In the presence of SO₂, activity tests of the fresh and aged IMP1-M2 monolithic catalyst yielded a different activity profile than IMP1-M1. After aging the monolith at 900°C, T50 values of O₂, C₃H₆ and C₃H₈ species were improved. Slight decrease in T50 values of H₂ and CO species indicate that thermal aging did not affect the conversions of these species. However, when IMP1-M1 and IMP1-M2 were compared in general, it can be seen that IMP1-M2 has higher T50 values, so the detrimental effect of SO₂ was reflected on the catalytic activity as an increase in light-off temperatures.

5.1.2. Catalytic Activity Tests of IMP2 Catalyst

Since the noble metals are rare and expensive, they are incorporated in three way catalyst compositions at very low concentrations. On the other hand, transition metals are abundant and much more cost effective. Therefore research have been focused on replacing noble metals with transition metals, or lowering the amount of noble metals by combining them with transition metals. For that reason, after the activity tests of Pd-only IMP1 catalyst were completed, a Mn-only catalyst IMP2 was synthesized with 0.70 wt % Mn impregnation on Ce_{0.8}Zr_{0.2}O₂. Since Mn containing catalysts are very susceptible to SO₂ exposure, only the effect of thermal aging was investigated with IMP2 catalyst.

Thus, only one monolith was washcoated with the catalyst slurry and named as IMP2-M1. Using the ICP-MS results, Mn loading of the monolithic catalyst was calculated as 12.48 g/ft³.

The first test was carried out using the fresh IMP2-M1 monolith with the simulated exhaust gas mixture not including SO₂. The monolithic catalyst was then aged at 900°C with dry air and the second test under the same conditions was performed using the aged monolith. Catalytic activity data of the fresh and aged IMP2-M1 monolithic catalyst is given in Table 16-17 and a visualization of variance in T50 values of the two tests is shown in Figure 24. Conversion-temperature profiles of fresh and aged catalytic activity tests are given in Appendix E.

Table 16 Catalytic activity data of IMP2-M1 monolithic catalyst in Test 1 without SO₂ (Fresh Monolith)

Species	Heating			Cooling		
	T50 (C°)	Max. Conv. (%)	Tmax (C°)	T50 (C°)	Max. Conv. (%)	Tmax (C°)
H ₂	385	98	538	349	98	547
CO	411	99	597	388	99	595
O ₂	403	100	597	368	100	595
C ₃ H ₆	413	100	597	380	100	585
C ₃ H ₈	491	84	597	464	85	595

Table 17 Catalytic activity data of IMP2-M1 monolithic catalyst in Test 2 without SO₂ (Monolith Aged at 900°C)

Species	Heating			Cooling		
	T50 (C°)	Max. Conv. (%)	Tmax (C°)	T50 (C°)	Max. Conv. (%)	Tmax (C°)
H ₂	543	88	597	483	89	595
CO	-	-	-	-	-	-
O ₂	504	95	596	463	100	587
C ₃ H ₆	503	95	597	464	100	592
C ₃ H ₈	594	54	590	-	48	592

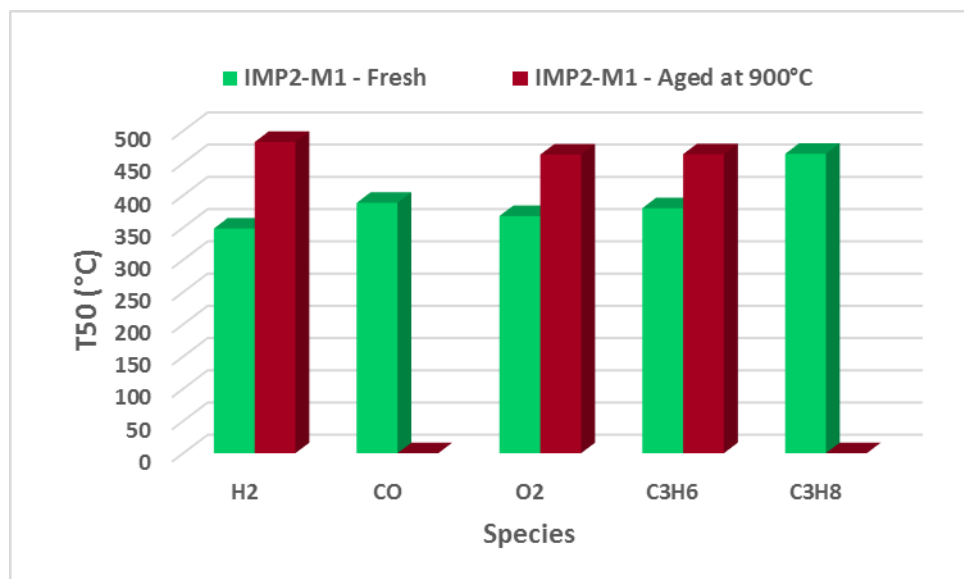


Figure 24 Change in T50 values for IMP2-M1 monolithic catalyst upon Thermal Aging (Tests with no SO₂)

Looking at the activity data, it can be inferred that the fresh IMP2-M1 monolithic catalyst is capable of converting all species at high conversions and reasonable T50 values. However, when the monolith was subjected to thermal aging at 900°C, irreversible activity losses were encountered especially in CO and C₃H₈ conversions. Catalyst lost the ability of converting CO and the maximum conversion of C₃H₈ fell back to 48 %. Also, T50 values of other species considerably increased after thermal aging. The fact is that a Mn-only catalyst IMP2 could not catch up with the performance of noble metal containing IMP1, as expected. Apparently, noble metal is an essential part of a three way catalyst and cannot simply be replaced entirely with a transition metal.

5.1.3. Catalytic Activity Tests of IMP3 Catalyst

After the performances of Pd-only and Mn-only catalysts IMP1 and IMP2 were evaluated, the effect of combination of Pd and Mn metals was studied with the catalyst IMP3. For this purpose, total metal loading was kept at 0.70 wt % as in the previous catalysts, with 0.60 wt % Pd and 0.10 wt % Mn separately impregnated on equal portions of Ce_{0.8}Zr_{0.2}O₂ and then combined. Two laboratory size monoliths were

washcoated with the catalyst slurry and named as IMP3-M1 and IMP3-M2. Via ICP-MS analysis results, Pd content of the two monoliths were calculated as 8.65 g/ft³ and 9.26 g/ft³ and Mn contents were calculated as 1.69 g/ft³ and 1.81 g/ft³, respectively.

Using the IMP3-M1 monolithic catalyst, effect of thermal aging was investigated with two activity tests using the simulated exhaust gas mixture that does not contain SO₂. After the first of the fresh IMP3-M1, and the monolith was subjected to thermal aging at 900°C and the second test was performed using the aged monolith. Catalytic activity data of the fresh and aged tests of IMP3-M1 are given in Table 18-19 and comparison of the T50 values of the two tests are displayed on Figure 25. Conversion-temperature profiles of fresh and aged catalytic activity tests are given in Appendix E.

Table 18 Catalytic activity data of IMP3-M1 monolithic catalyst in Test 1 without SO₂ (Fresh Monolith)

Species	Heating			Cooling		
	T50 (C°)	Max. Conv. (%)	Tmax (C°)	T50 (C°)	Max. Conv. (%)	Tmax (C°)
H ₂	188	96	597	163	98	283
CO	261	100	589	225	100	593
O ₂	258	95	597	221	95	544
C ₃ H ₆	265	100	400	218	100	463
C ₃ H ₈	370	96	596	309	96	588

Table 19 Catalytic activity data of IMP3-M1 monolithic catalyst in Test 2 without SO₂ (Monolith Aged 900°C)

Species	Heating			Cooling		
	T50 (C°)	Max. Conv. (%)	Tmax (C°)	T50 (C°)	Max. Conv. (%)	Tmax (C°)
H ₂	269	100	598	200	100	501
CO	266	100	597	230	100	582
O ₂	253	92	588	191	92	576
C ₃ H ₆	262	100	588	205	100	593
C ₃ H ₈	407	97	598	323	97	597

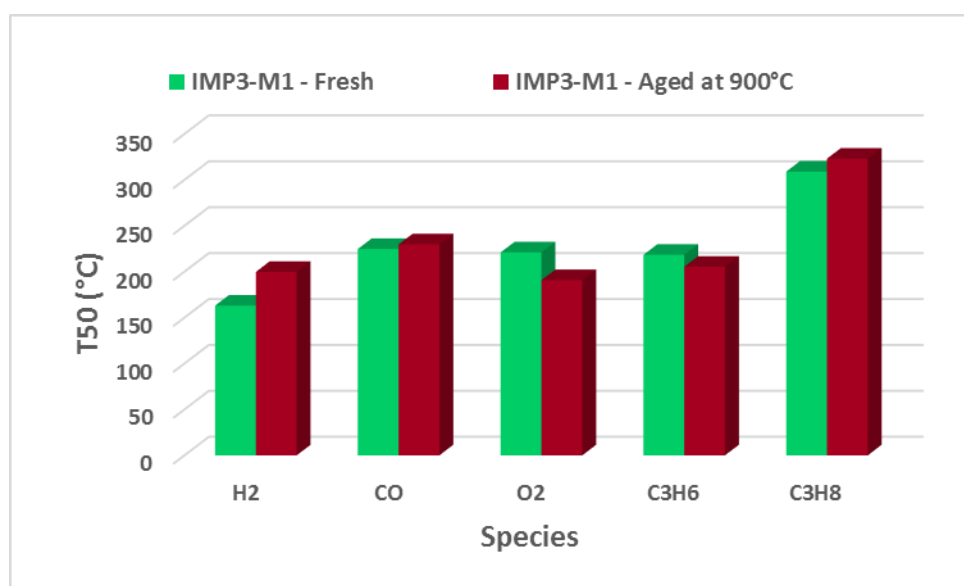


Figure 25 Change in T50 values for IMP3-M1 monolithic catalyst upon Thermal Aging (Tests with no SO₂)

When the activity data of the two tests were evaluated, it can be said that thermal aging process did not have much of a negative impact on the catalytic performance. T50 values of the O₂ and C₃H₆ conversions were improved after thermal aging and there were just slight increases in the T50 value of CO and C₃H₈ conversions. For a better interpretation of any contribution of Mn in terms of catalytic activity, a comparison between the T50 values of IMP1 and IMP3 for activity tests without SO₂ is displayed on Figure 26.

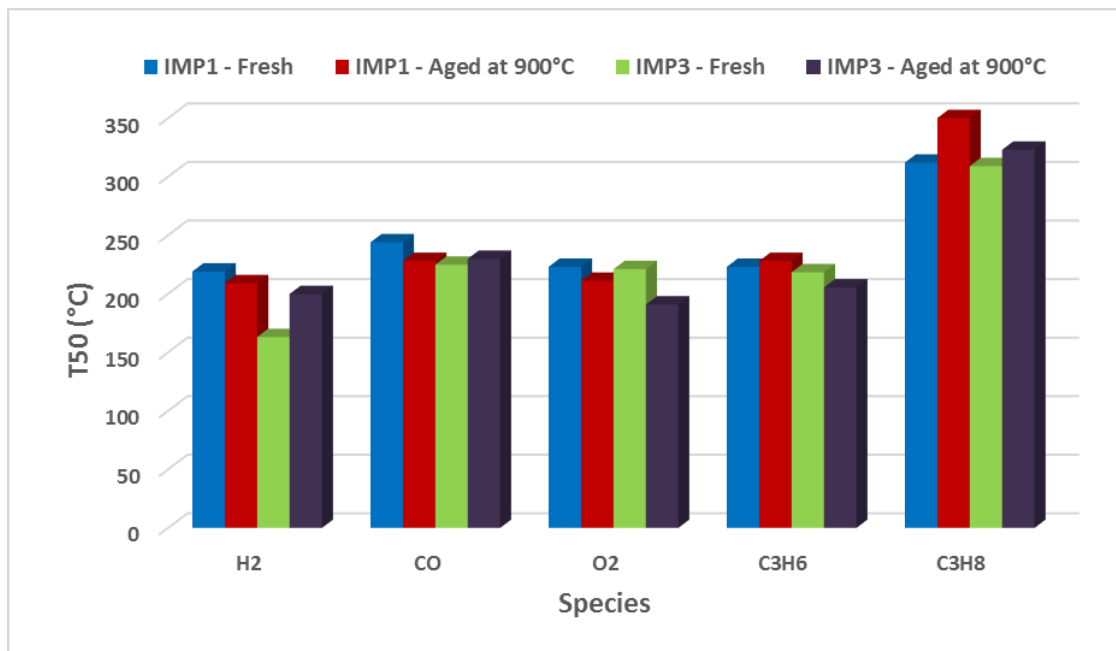


Figure 26 Comparison of T50 values of IMP1 and IMP3 monolithic catalysts with thermal aging effect (Tests with no SO₂)

T50 values of IMP1 and IMP3 catalysts are not much different than each other, yet at some points effect of Mn supplement on activity is clearly seen. For instance, when the T50 values of the fresh tests were compared for CO conversion, it can be seen that the performance of catalyst IMP3 is better than IMP1. This is actually in accordance with the findings of our computational studies. DFT calculations revealed that the synergism between Pd and Mn enhances the OSC property of the catalyst and accordingly promotes CO oxidation. For C₃H₆ and C₃H₈ conversions, T50 values are almost the same for the fresh tests, however IMP3 has superior activity in the aged in the aged tests.

Effect of thermal aging is further investigated with another set of tests, this time in the presence of SO₂. First test was done with the fresh IMP3-M2 monolithic catalyst, and after the monolith was aged at 900°C, second test was performed under the same test conditions. Catalytic activity data of the fresh and aged tests of IMP3-M2 are given in Table 20-21 and a comparison of the T50 values of the two tests can be seen in Figure 27. Conversion-temperature profiles of fresh and aged catalytic activity tests are given in Appendix E.

Table 20 Catalytic activity data of IMP3-M2 monolithic catalyst in Test 1 with SO₂
(Fresh Monolith)

Species	Heating			Cooling		
	T50 (C°)	Max. Conv. (%)	Tmax (C°)	T50 (C°)	Max. Conv. (%)	Tmax (C°)
H ₂	211	100	299	272	98	340
CO	261	100	500	281	100	516
O ₂	290	69	587	284	70	537
C ₃ H ₆	268	100	598	266	100	498
C ₃ H ₈	395	95	598	345	95	598

Table 21 Catalytic activity data of IMP3-M2 monolithic catalyst in Test 2 with SO₂
(Monolith Aged at 900°C)

Species	Heating			Cooling		
	T50 (C°)	Max. Conv. (%)	Tmax (C°)	T50 (C°)	Max. Conv. (%)	Tmax (C°)
H ₂	311	89	367	269	89	318
CO	318	100	598	323	100	595
O ₂	317	100	430	282	100	441
C ₃ H ₆	326	95	471	314	96	412
C ₃ H ₈	404	86	598	356	85	590

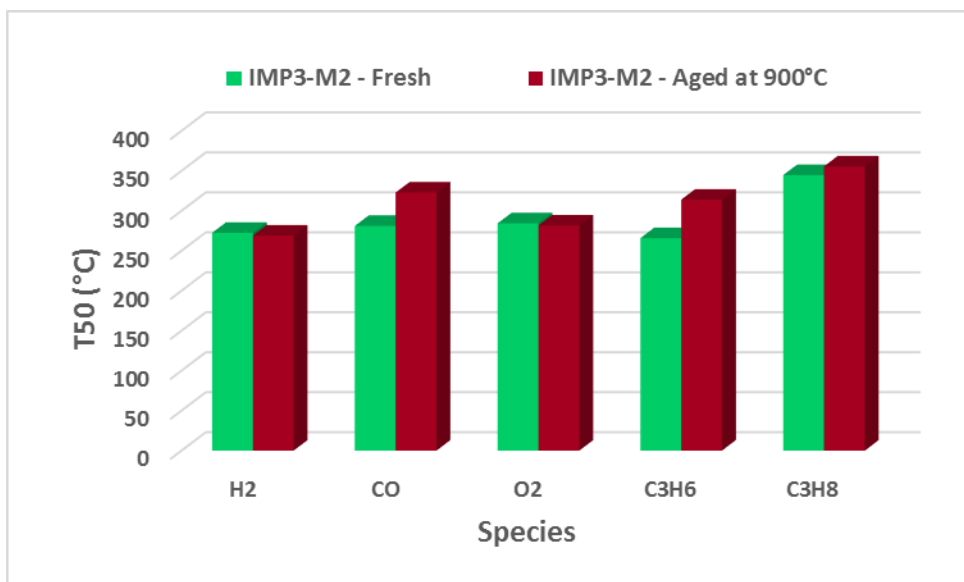


Figure 27 Change in T50 values for IMP3-M2 monolithic catalyst upon Thermal Aging (Tests with SO₂)

Presence of SO₂ in the simulated exhaust gas feed entirely altered the catalytic activity behavior of IMP3. Conversions of CO, C₃H₆ and C₃H₈ species were harmed after the monolith was thermally aged and the conversions of H₂ and O₂ did not change with thermal aging. When the two monolithic catalysts, IMP3-M1 and IMP3-M2 from the same batch are compared, the detrimental effect of SO₂ on catalytic activity can be spotted as in the case for IMP1. In order to compare the performances of IMP1 and IMP3 catalysts in the presence of SO₂, their T50 values are illustrated in Figure 28.

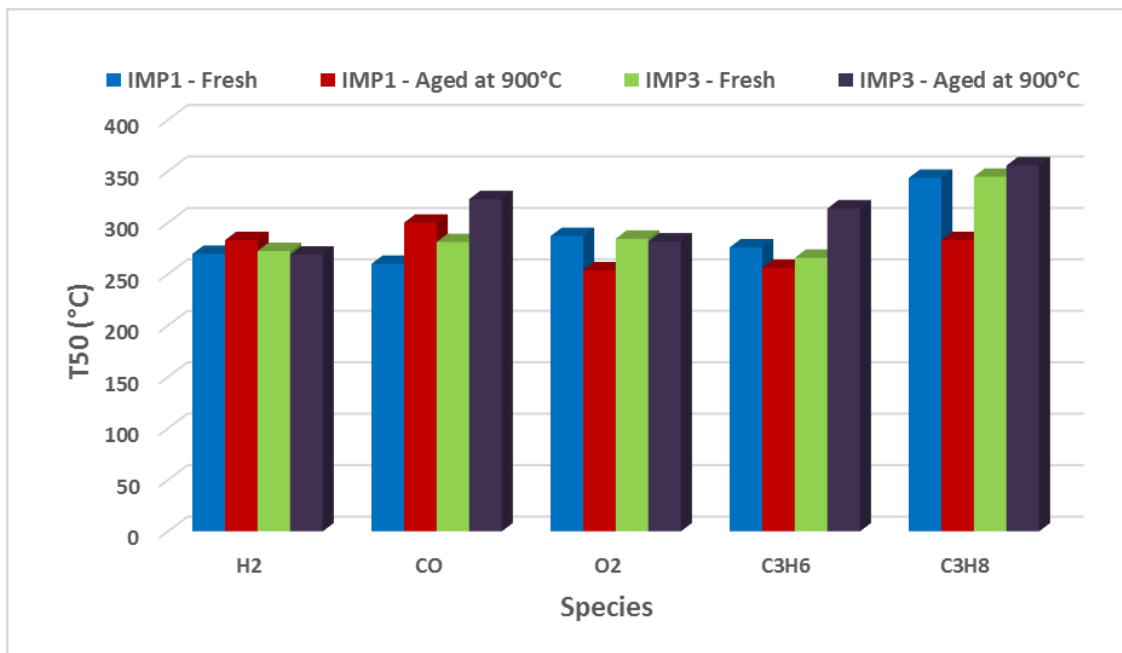


Figure 28 Comparison of T50 values of IMP1 and IMP3 monolithic catalysts with thermal aging effect (Tests with SO₂)

Comparison of T50 values reveals that Mn containing IMP3 catalyst is more susceptible to sulfur poisoning as expected and accordingly, it has a lesser performance than IMP1 for almost all cases.

5.1.4. Catalytic Activity Tests of IMP4 Catalyst

Combination of Pd and Mn in three way catalyst composition was also investigated with respect to varying loadings of these two metals. In order to see whether a little amount of Pd coupled with a higher Mn loading could provide a sufficient catalytic activity, catalyst IMP4 was synthesized. For this purpose, Pd and Mn loadings in IMP3 catalyst were interchanged, thus 0.10 wt % Pd and 0.60 wt % Mn were separately impregnated on Ce_{0.8}Zr_{0.2}O₂ and then combined. Two laboratory size monoliths were washcoated with the catalyst slurry and named as IMP4-M1 and IMP4-M2. Based on the ICP-MS results and the slurry pick up of the monolith, Pd contents of the two monoliths were calculated to be 1.45 g/ft³ and 1.32 g/ft³ and Mn contents were calculated to be 11.86 g/ft³ and 10.84 g/ft³ for IMP4-M1 and IMP4-M2, respectively.

Effect of thermal aging in the absence of SO₂ in the gas feed was investigated using IMP4-M1 monolithic catalyst. Catalytic activity data of the fresh and thermally aged IMP4-M1 are given in Table 22-23 and a comparison of the T50 values of the two fresh and aged tests is presented in Figure 29. Conversion-temperature profiles of fresh and aged catalytic activity tests are given in Appendix E.

Table 22 Catalytic activity data of IMP4-M1 monolithic catalyst in Test 1 without SO₂ (Fresh Monolith)

Species	Heating			Cooling		
	T50 (C°)	Max. Conv. (%)	Tmax (C°)	T50 (C°)	Max. Conv. (%)	Tmax (C°)
H ₂	326	98	556	295	98	580
CO	316	99	597	286	99	596
O ₂	316	89	597	268	89	580
C ₃ H ₆	352	100	595	307	100	532
C ₃ H ₈	489	84	597	454	89	596

Table 23 Catalytic activity data of IMP4-M1 monolithic catalyst in Test 2 without SO₂ (Monolith Aged 900°C)

Species	Heating			Cooling		
	T50 (C°)	Max. Conv. (%)	Tmax (C°)	T50 (C°)	Max. Conv. (%)	Tmax (C°)
H ₂	335	98	564	297	99	564
CO	332	95	597	309	96	591
O ₂	329	87	597	297	87	585
C ₃ H ₆	331	99	591	308	100	585
C ₃ H ₈	574	59	597	550	58	595

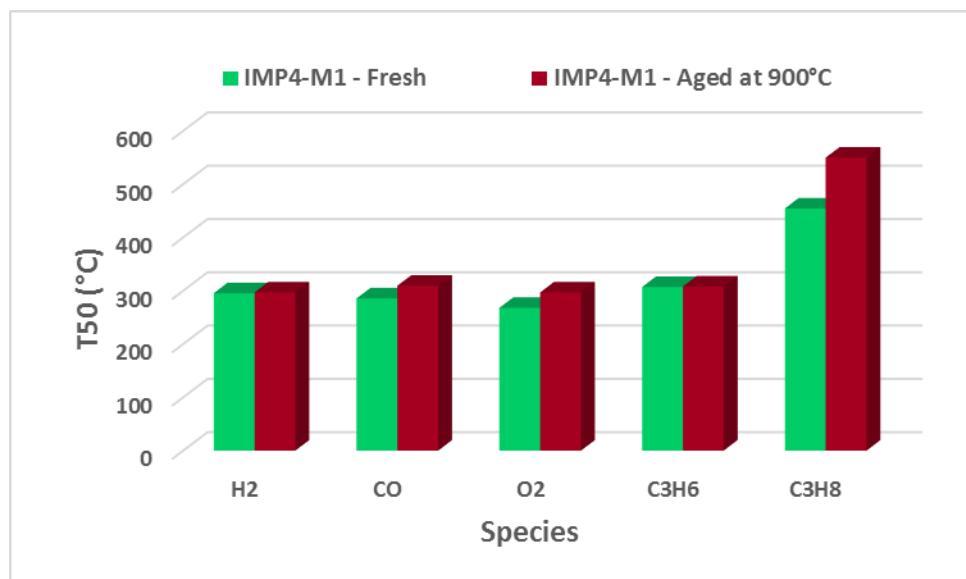


Figure 29 Change in T50 values for IMP4-M1 monolithic catalyst upon Thermal Aging (Tests with no SO₂)

When the data of the two tests are analyzed, it can be seen that the negative impact of thermal aging is more pronounced for the conversions of CO and C₃H₈ species. An increase in the T50 value of CO conversion takes place with a slight decrease in the maximum conversion after aging the monolith at 900°C. C₃H₈ conversion was much more affected from thermal aging, with an increase in the light-off temperature and serious decline in the maximum conversion. On the contrary, C₃H₆ conversion was not affected from thermal aging at all.

The effect of thermal aging was also investigated via another set of activity tests using IMP4-M2 monolithic catalyst, with the simulated gas feed containing SO₂. Catalytic activity data of the fresh and thermally aged IMP4-M2 monolith are given in Table 24-25 and the comparison of the T50 values of the two tests are demonstrated in Figure 30. Conversion-temperature profiles of fresh and aged catalytic activity tests are given in Appendix E.

Table 24 Catalytic activity data of IMP4-M2 monolithic catalyst in Test 1 with SO₂
(Fresh Monolith)

Species	Heating			Cooling		
	T50 (C°)	Max. Conv. (%)	Tmax (C°)	T50 (C°)	Max. Conv. (%)	Tmax (C°)
H ₂	347	100	505	339	96	447
CO	356	100	598	352	100	595
O ₂	375	66	598	359	66	547
C ₃ H ₆	327	99	531	316	100	547
C ₃ H ₈	492	90	592	458	93	578

Table 25 Catalytic activity data of IMP4-M2 monolithic catalyst in Test 2 with SO₂
(Monolith Aged 900°C)

Species	Heating			Cooling		
	T50 (C°)	Max. Conv. (%)	Tmax (C°)	T50 (C°)	Max. Conv. (%)	Tmax (C°)
H ₂	381	100	588	307	98	597
CO	418	99	597	354	99	596
O ₂	402	100	596	329	100	566
C ₃ H ₆	393	100	584	341	99	511
C ₃ H ₈	438	83	596	388	86	592

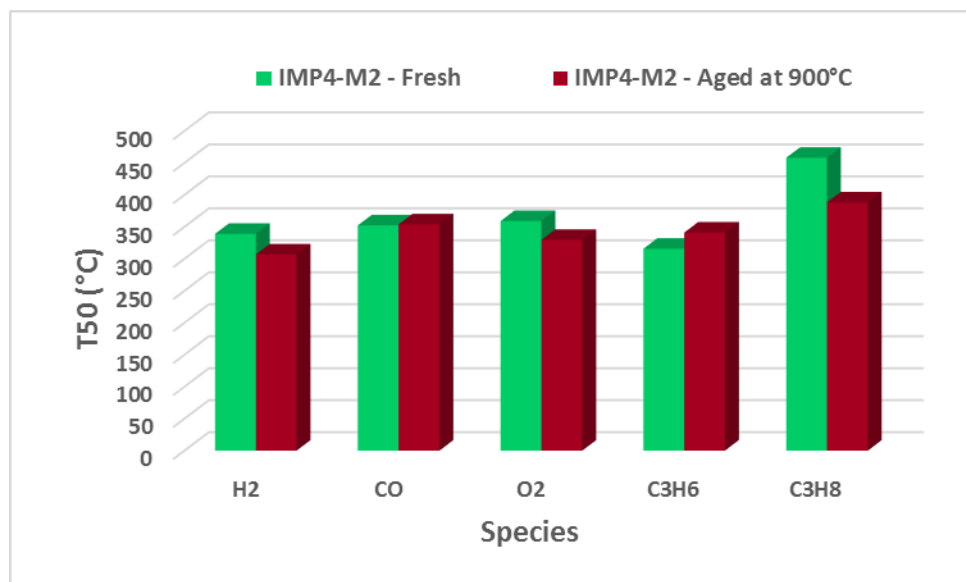


Figure 30 Change in T50 values for IMP4-M2 monolithic catalyst upon Thermal Aging (Tests with SO₂)

Again, the presence of SO₂ completely changed the activity behavior of the catalyst. For instance, CO conversion was not affected from thermal aging and the light-off temperature of C₃H₈ conversion was decreased and maximum conversion was increased, in contrast to the outcomes of the IMP4-M1 monolithic catalyst. Therefore, SO₂ is proven to be facilitating C₃H₈ conversion. On the other side, T50 value of C₃H₆ conversion increased after thermal aging so SO₂ did not have such an effect on C₃H₆ conversion.

5.1.5. Catalytic Activity Tests of IMP5 Catalyst

As last one of the impregnated catalyst series, IMP5 was synthesized and instead of using Pd as a noble metal, Rh was incorporated in the catalyst composition. Rh is generally included in conventional three way catalyst compositions as it functions as a reductive catalyst. Therefore, Rh was combined with an oxidative catalyst Mn and the effect of collaboration of these metals was investigated in terms of catalytic performance. Rh is loaded in three way catalyst compositions at very low concentrations, hence in catalyst IMP5, 0.10 wt % Rh loading together with 0.60 wt % Mn content were separately impregnated on equal portions of Ce_{0.8}Zr_{0.2}O₂ and then

combined. Using the catalyst slurry, one laboratory size monolith was washcoated and named as IMP5-M1. Based on the results of ICP-MS characterization and catalyst pick-up value, Rh content was calculated to be 1.04 g/ft³ and Mn content was calculated to be 7.92 g/ft³.

Catalytic performance of the catalyst IMP5 was investigated via effect of thermal aging. Using the fresh IMP5-M1 monolithic catalyst, first activity test was performed with simulated gas feed in the absence of SO₂. Then, the monolith was aged at 900°C with dry air and the second test was carried out in the same experimental conditions. Catalytic activity data of the fresh and aged tests of IMP5-M1 are given in Table 26-27 and comparison of the T50 values of the two tests is demonstrated in Figure 31. Conversion-temperature profiles of fresh and aged catalytic activity tests are given in Appendix E.

Table 26 Catalytic activity data of IMP5-M1 monolithic catalyst in Test 1 without SO₂ (Fresh Monolith)

Species	Heating			Cooling		
	T50 (C°)	Max. Conv. (%)	Tmax (C°)	T50 (C°)	Max. Conv. (%)	Tmax (C°)
H ₂	348	99	574	308	98	579
CO	345	99	598	311	99	591
O ₂	344	91	597	303	91	585
C ₃ H ₆	354	99	597	315	100	596
C ₃ H ₈	486	84	598	422	82	596

Table 27 Catalytic activity data of IMP5-M1 monolithic catalyst in Test 2 without SO₂
(Monolith Aged at 900°C)

Species	Heating			Cooling		
	T50 (C°)	Max. Conv. (%)	Tmax (C°)	T50 (C°)	Max. Conv. (%)	Tmax (C°)
H ₂	427	93	598	382	93	592
CO	422	98	598	358	98	596
O ₂	426	87	596	364	87	592
C ₃ H ₆	456	100	598	442	100	596
C ₃ H ₈	-	47	598	-	45	592

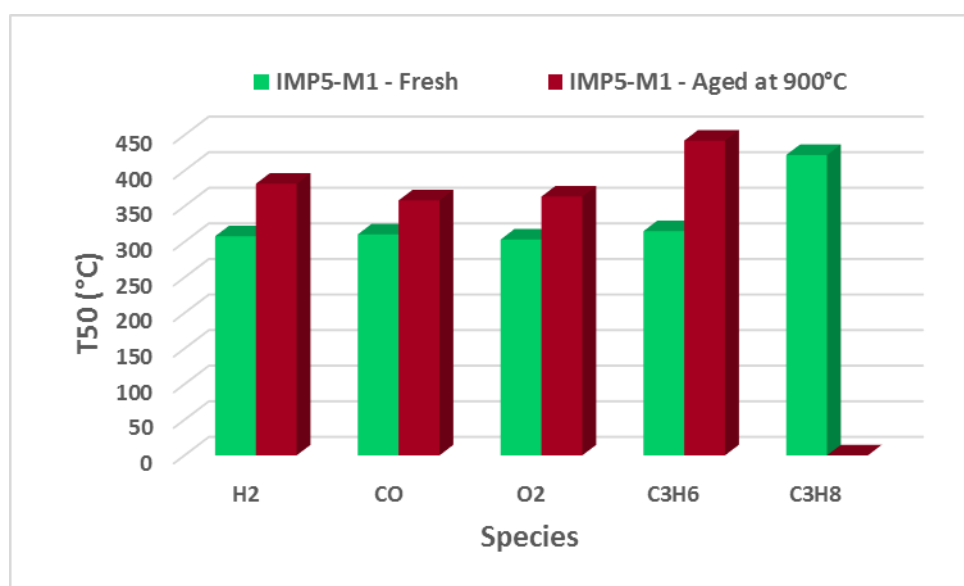


Figure 31 Change in T50 values for IMP5-M1 monolithic catalyst upon Thermal Aging
(Tests with no SO₂)

Fresh IMP5-M1 monolithic catalyst was capable of converting all species with relatively high conversions. However, after the catalyst was thermally aged, catalytic activity was dramatically damaged. Light-off temperatures of all species increased and serious activity loss was encountered in especially C₃H₈ species.

Since IMP4 and IMP5 catalysts are akin and the only difference between them is the type of noble metal, a comparison of the T50 values of these two catalysts was made and presented in Figure 32. Conversion-temperature profiles of fresh and aged catalytic activity tests are given in Appendix E.

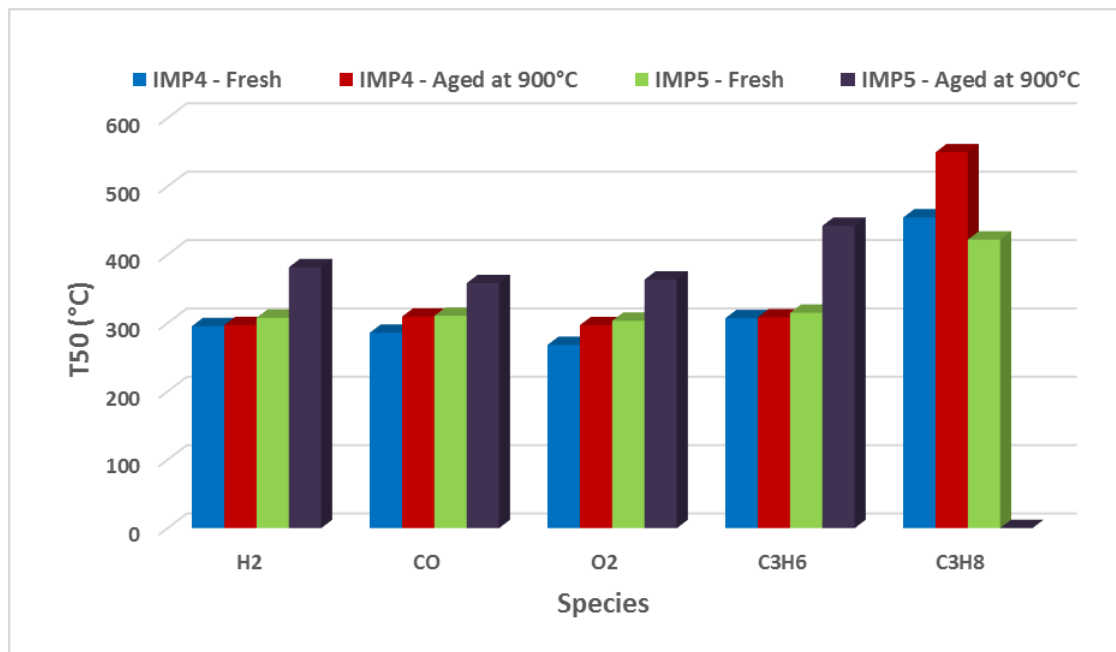


Figure 32 Comparison of T50 values of IMP4 and IMP5 monolithic catalysts with thermal aging effect (Tests with no SO₂)

As it can be inferred from the comparison, in terms of catalytic performance, combination of Pd and Mn metals is a much better choice than Rh and Mn combination. For all species, T50 values of the IMP5 catalyst are greater than T50 values of IMP4. For CO oxidation, such behavior was also observed with the DFT studies. Computational studies on Pd+Mn/CZO surface was found to be superior to Rh+Mn/CZO for CO oxidation indicating that the Pd-Mn couple is synergistically. Above all, thermal aging had a much more degrading impact on the catalytic activity of the IMP5 catalyst. Therefore, combination of Rh and Mn in three way catalyst composition was considered to be ineffective.

5.2. Catalysts Synthesized via Solution Combustion Method

5.2.1. Catalytic Activity Tests of SC1 Catalyst

The first catalyst SC1 was synthesized by solution combustion method and has a composition of $Ce_{0.79}Zr_{0.2}Pd_{0.01}O_2$. Two laboratory size monoliths were washcoated in the catalyst slurry and named as SC1-M1 and SC1-M2. Using the ICP-MS analysis results, Pd metal loadings for SC1-M1 and SC1-M2 were calculated as 8.35 g/ft^3 and 8.59 g/ft^3 , respectively.

In order to investigate the effect of thermal aging on catalytic activity, SC1-M1 monolithic catalyst was used. First test was carried out with the fresh SC1-M21 monolithic catalyst. After the first test, the monolith was aged at 900°C for 1 h with a dry air flow and the second test was performed using the aged monolith. Catalytic activity data of tests with simulated gas mixture in the absence of SO_2 are given in Table 28-29 and the comparison of T50 values are shown in Figure 33. Conversion-temperature profiles of fresh and aged catalytic activity tests are given in Appendix E.

Table 28 Catalytic activity data of SC1-M1 monolithic catalyst in Test 1 without SO_2 (Fresh Monolith)

Species	Heating			Cooling		
	T50 (C°)	Max. Conv. (%)	Tmax (C°)	T50 (C°)	Max. Conv. (%)	Tmax (C°)
H₂	285	99	399	278	98	537
CO	344	100	583	292	100	580
O₂	323	88	597	283	88	596
C₃H₆	349	100	502	290	100	541
C₃H₈	474	88	593	442	90	596

Table 29 Catalytic activity data of SC1-M1 monolithic catalyst in Test 2 without SO₂ (Monolith aged at 900°C)

Species	Heating			Cooling		
	T50 (C°)	Max. Conv. (%)	Tmax (C°)	T50 (C°)	Max. Conv. (%)	Tmax (C°)
H ₂	251	99	373	256	98	450
CO	324	100	584	290	100	586
O ₂	312	98	597	274	99	586
C ₃ H ₆	325	100	415	309	100	469
C ₃ H ₈	537	62	596	517	67	595

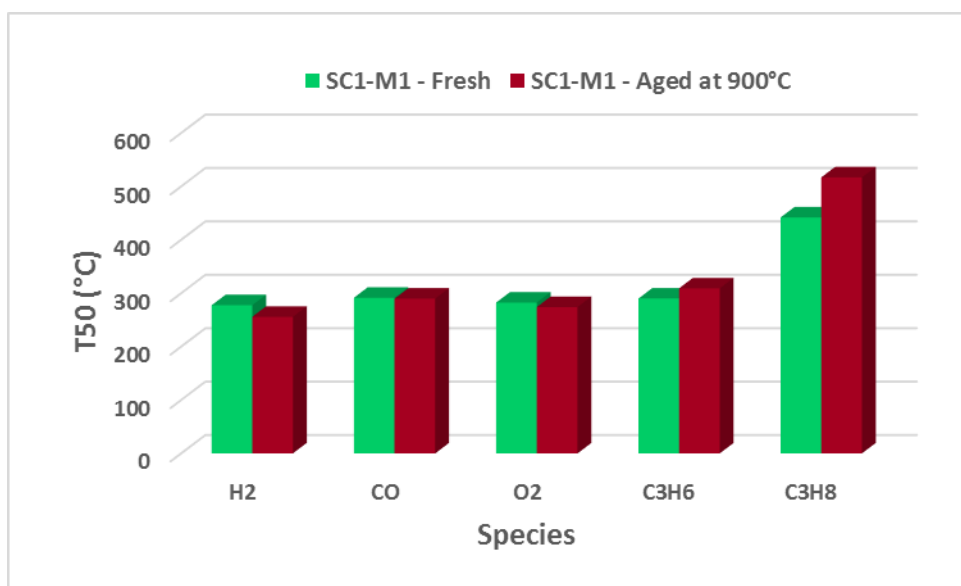


Figure 33 Change in T50 values for SC1-M1 monolithic catalyst upon Thermal Aging

Comparisons of the T50 values of the fresh and aged tests showed that thermal aging has different effects on the catalytic activity. For instance, H₂ and O₂ conversions were improved after aging, whereas CO conversions was not affected. However, C₃H₆ and C₃H₈ conversions deteriorates after aging and the negative impact is especially more significant in C₃H₈ conversion.

For a further investigation on the catalytic performance, effect of SO₂ exposure was investigated using SC1-M2 monolith. First activity test was performed with the simulated exhaust gas mixture in the absence of SO₂. After the fresh test, same monolith was tested with the simulated exhaust gas containing SO₂ in order to evaluate the performance change upon SO₂ exposure. Catalytic activity data of SC1-M2 monolithic catalyst are given in Table 30-31. For a better interpretation of the data, T50 values of the two activity tests of SC1-M2 monolith were compared in Figure 34. Conversion-temperature profiles of the catalytic activity tests with and without SO₂ are given in Appendix E.

Table 30 Catalytic activity data of SC1-M2 monolithic catalyst in Test 1 without SO₂

Species	Heating			Cooling		
	T50 (C°)	Max. Conv. (%)	Tmax (C°)	T50 (C°)	Max. Conv. (%)	Tmax (C°)
H ₂	265	100	545	264	100	391
CO	269	100	530	274	100	478
O ₂	353	62	570	290	62	583
C ₃ H ₆	305	100	408	281	100	377
C ₃ H ₈	482	87	596	466	90	594

Table 31 Catalytic activity data of SC1-M2 monolithic catalyst in Test 2 with SO₂

Species	Heating			Cooling		
	T50 (C°)	Max. Conv. (%)	Tmax (C°)	T50 (C°)	Max. Conv. (%)	Tmax (C°)
H ₂	317	93	564	297	100	480
CO	354	100	597	358	100	574
O ₂	357	80	597	300	90	387
C ₃ H ₆	346	100	443	342	100	394
C ₃ H ₈	445	92	594	402	93	593

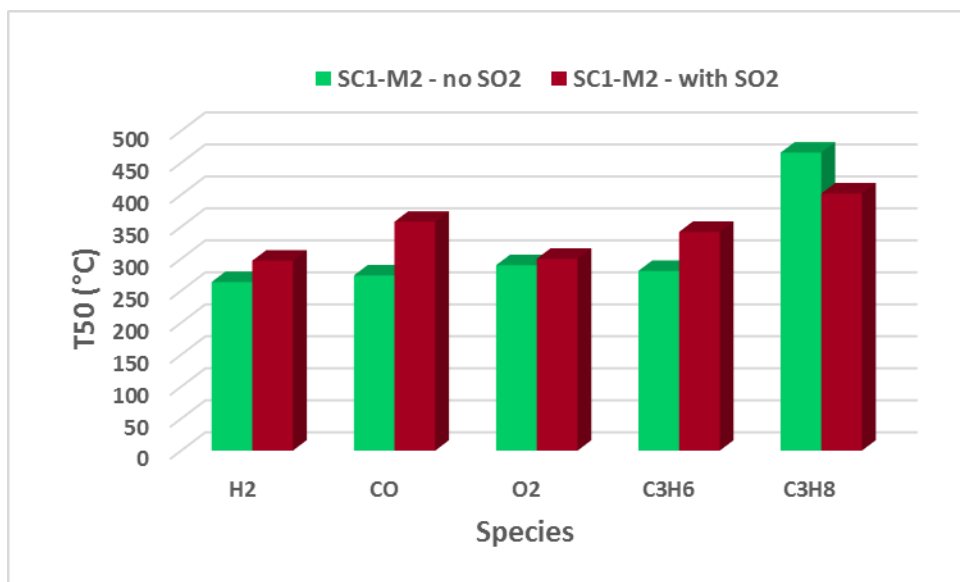


Figure 34 Change in T50 values for SC1-M2 monolithic catalyst upon SO₂ exposure

SO₂ is known to be poisonous for three way catalytic converters, therefore exposure had a detrimental effect on the conversion of almost all species, except C₃H₈ conversion. C₃H₈ conversion was increased from 90 % to 93 % along with a remarkable decrease in the light-off temperature.

5.2.2. Catalytic Activity Tests of SC2 Catalyst

Similar to IMP2, a Mn-only catalyst SC2 was synthesized with solution combustion method. Since Mn metal is economic and abundant, this time its concentration in the catalyst composition was kept 10 fold higher (in moles basis) than the amount of Pd in SC1 catalyst and Ce_{0.8}Zr_{0.1}Mn_{0.1}O₂ was synthesized. Two laboratory size monoliths SC2-M1 and SC2-M2 were washcoated with the catalyst slurry and using the ICP-MS results, Mn metal loadings were calculated as 72.94 g/ft³ and 78.84 g/ft³, respectively.

Effect of thermal aging was assessed with SC2-M1 monolithic catalyst. Catalytic activity data of the fresh and aged tests of SC2-M1 are given in Table 32-33 and variation of T50 values with aging process are shown in Figure 35. Conversion-temperature profiles of fresh and aged catalytic activity tests are given in Appendix E.

Table 32 Catalytic activity data of SC2-M2 monolithic catalyst in Test 1 without SO₂
(Fresh Monolith)

Species	Heating			Cooling		
	T50 (C°)	Max. Conv. (%)	Tmax (C°)	T50 (C°)	Max. Conv. (%)	Tmax (C°)
H ₂	382	97	589	375	97	510
CO	507	97	598	447	97	592
O ₂	485	85	598	422	85	587
C ₃ H ₆	460	100	597	426	100	581
C ₃ H ₈	545	80	598	514	80	596

Table 33 Catalytic activity data of SC2-M2 monolithic catalyst in Test 2 without SO₂
(Monolith aged at 900°C)

Species	Heating			Cooling		
	T50 (C°)	Max. Conv. (%)	Tmax (C°)	T50 (C°)	Max. Conv. (%)	Tmax (C°)
H ₂	524	79	598	491	80	596
CO	-	48	598	-	49	596
O ₂	574	59	598	554	59	591
C ₃ H ₆	525	82	598	514	83	591
C ₃ H ₈	-	36	598	-	43	596

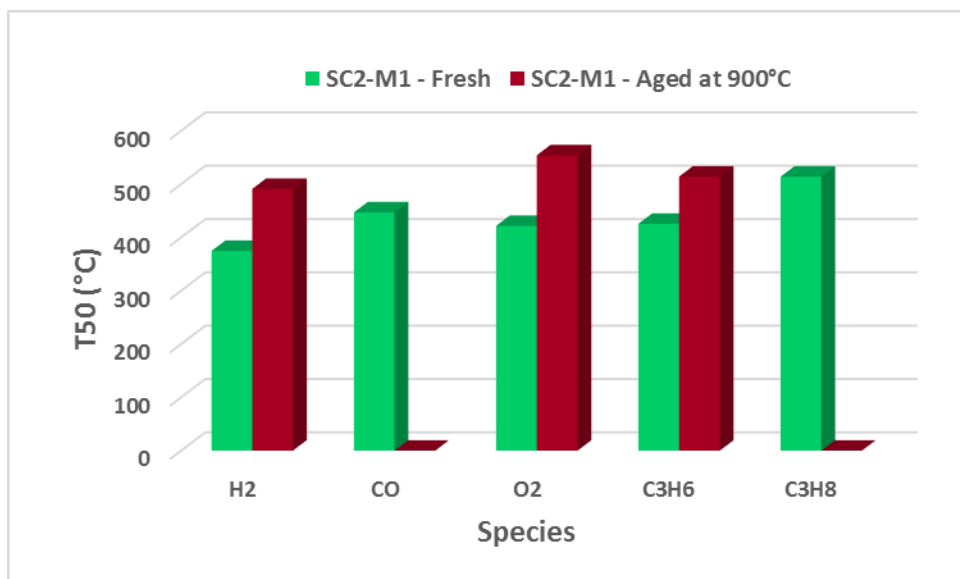


Figure 35 Change in T50 values for SC1-M1 monolithic catalyst upon Thermal Aging

Catalytic activity data show that the fresh SC2-M1 monolithic catalyst can provide high conversion values for majority of species. However, in terms of light-off temperatures, SC2-M1 could not catch up with the performance of SC1-M1 as expected. Furthermore, comparison between fresh and aged tests displayed that thermal aging severely damages catalytic activity in terms of both maximum conversion and T50 values of all species.

Effect of SO₂ exposure was investigated by using SC2-M2 monolithic catalyst. First test was performed with the simulated exhaust gas mixture without SO₂, and in the following test SO₂ was included in the gas mixture. Catalytic activity data of SC2-M2 were given in Table 34-35 and comparison of the T50 values of the two tests were shown in Figure 36. Conversion-temperature profiles of the catalytic activity tests with and without SO₂ are given in Appendix E.

Table 34 Catalytic activity data of SC2-M2 monolithic catalyst in Test 1 without SO₂

Species	Heating			Cooling		
	T50 (C°)	Max. Conv. (%)	Tmax (C°)	T50 (C°)	Max. Conv. (%)	Tmax (C°)
H ₂	342	98	554	345	98	475
CO	485	100	597	425	100	586
O ₂	510	59	597	447	59	587
C ₃ H ₆	432	100	503	415	100	525
C ₃ H ₈	553	85	597	498	89	592

Table 35 Catalytic activity data of SC2-M2 monolithic catalyst in Test 2 with SO₂

Species	Heating			Cooling		
	T50 (C°)	Max. Conv. (%)	Tmax (C°)	T50 (C°)	Max. Conv. (%)	Tmax (C°)
H ₂	435	98	578	388	98	544
CO	516	74	597	542	75	589
O ₂	527	55	597	542	55	584
C ₃ H ₆	468	100	578	461	100	564
C ₃ H ₈	572	58	597	548	60	597

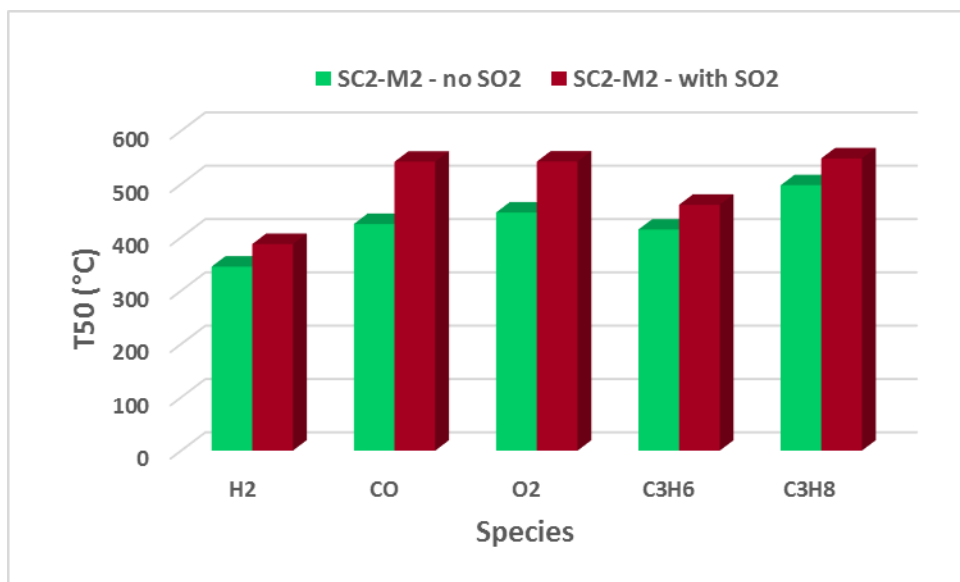


Figure 36 Change in T50 values for SC2-M2 monolithic catalyst upon SO₂ exposure

SO₂ exposure had a degrading effect on T50 values of all species. Especially, CO and C₃H₈ conversions were severely affected from SO₂. Maximum CO conversion was reduced from 100 % to 75 % conversion, along with a high increase in its light-off temperature. Similarly, maximum conversion of C₃H₈ decreased from 89 % to 69 % with an increase in the light-off temperature. Maximum C₃H₆ conversion could reach up to 100 % conversion in both tests however, T50 value increased after SO₂ exposure.

5.2.3. Catalytic Activity Tests of SC3 Catalyst

After evaluating the performance of Pd-only catalyst SC1 and Mn-only catalyst SC2, catalyst SC3 having a composition of Ce_{0.79}Zr_{0.1}Mn_{0.1}Pd_{0.01}O₂ was synthesized in order to investigate the effects of combination of both metals on catalytic performance with solution combustion method. Two laboratory size monoliths were washcoated with the catalyst slurry and named as SC3-M1 and SC3-M2. Based on the ICP-MS analysis results, Pd contents of the monolithic catalysts were calculated as 8.37 g/ft³ and 9.11 g/ft³ and Mn contents were calculated as 37.52 g/ft³ and 40.84 g/ft³ for SC3-M1 and SC3-M2, respectively.

Effect of thermal aging on catalytic performance in the absence of SO₂ was analyzed with SC3-M1 monolithic catalyst. Catalytic activity data of the fresh and aged tests of SC3-M1 are given in Table 36-37 and the comparison of T50 values of the two tests are shown in Figure 37. Conversion-temperature profiles of fresh and aged catalytic activity tests are given in Appendix E.

Table 36 Catalytic activity data of SC3-M1 monolithic catalyst in Test 1 without SO₂ (Fresh Monolith)

Species	Heating			Cooling		
	T50 (C°)	Max. Conv. (%)	Tmax (C°)	T50 (C°)	Max. Conv. (%)	Tmax (C°)
H ₂	239	100	365	241	100	292
CO	333	100	598	256	100	596
O ₂	320	89	598	251	89	596
C ₃ H ₆	329	100	586	260	100	453
C ₃ H ₈	411	100	598	365	100	587

Table 37 Catalytic activity data of SC3-M1 monolithic catalyst in Test 2 without SO₂ (Monolith aged at 900°C)

Species	Heating			Cooling		
	T50 (C°)	Max. Conv. (%)	Tmax (C°)	T50 (C°)	Max. Conv. (%)	Tmax (C°)
H ₂	188	99	360	196	98	493
CO	284	100	594	257	100	586
O ₂	283	87	597	253	87	591
C ₃ H ₆	285	100	529	276	100	529
C ₃ H ₈	357	97	590	417	96	586

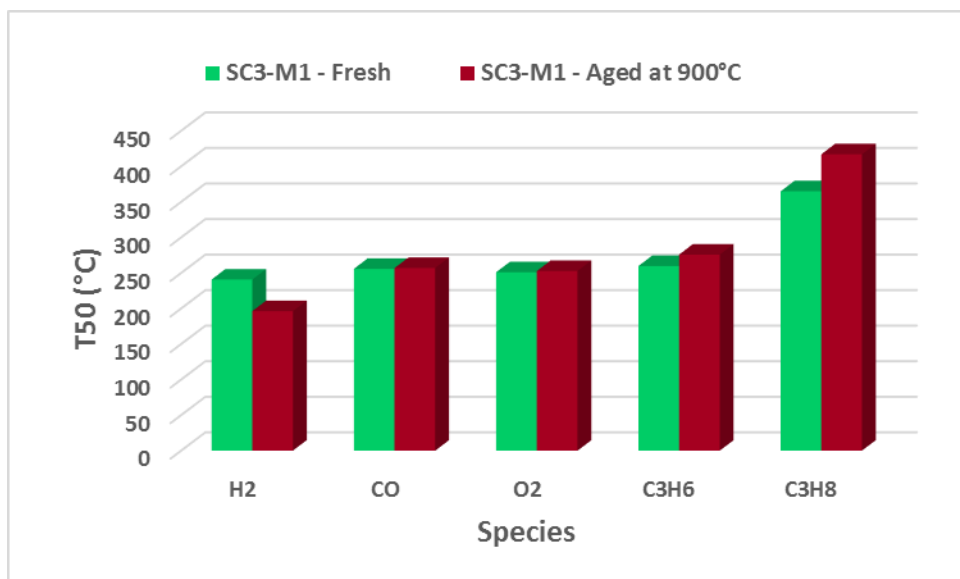


Figure 37 Change in T50 values for SC3-M1 monolithic catalyst upon Thermal Aging

When the activity data of the fresh and aged tests were compared, it can be said that thermal aging affected each species in a different manner. For instance, after the monolith was thermally aged, CO and O₂ conversions did not change whereas an improvement in H₂ conversion occurred. However, hydrocarbon conversions were negatively affected from aging and especially, a dramatic increase in T50 value of C₃H₈ conversion arised.

Performances of SC1-M1 and SC3-M1 under thermal aging are compared and illustrated on Figure 38.

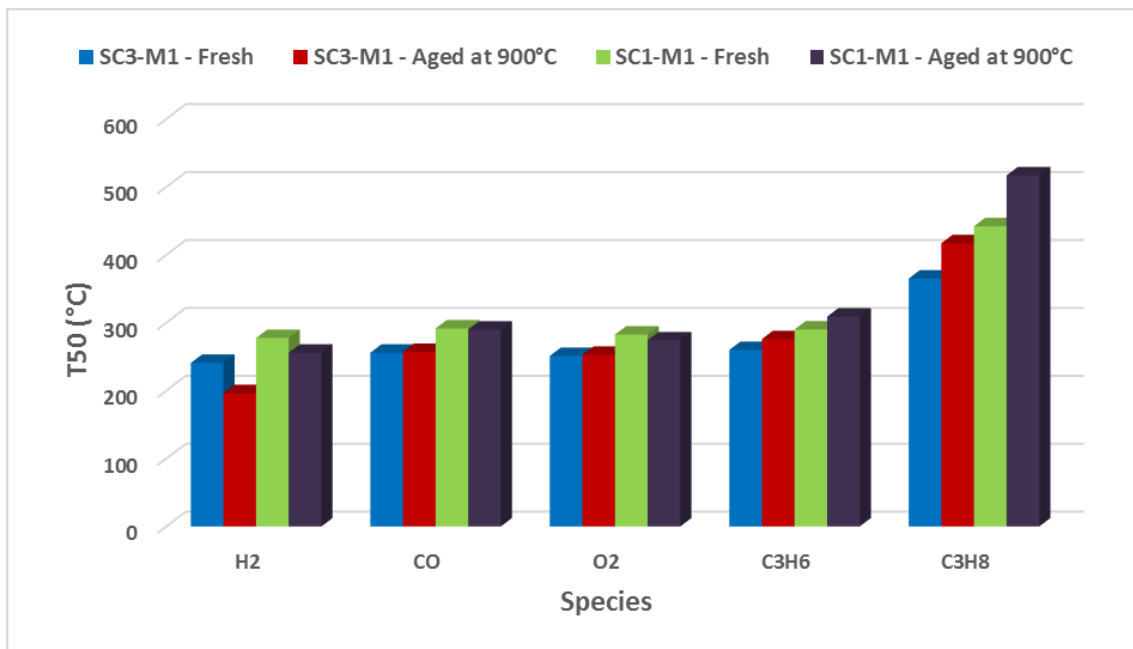


Figure 38 Comparison of T50 values of SC1 and SC3 monolithic catalysts with thermal aging effect (Tests with no SO₂)

The two catalysts have very similar activity trends between the activity tests of the fresh and aged catalysts, yet SC3 has clearly a superior performance than SC1 for the conversions of all species. As a matter of course, this behavior is attributed to the incorporation of manganese in the catalyst composition. This result is again in accordance with the finding of the computational studies.

SC3-M2 monolithic catalyst was used for the examination of on catalytic performance. Catalytic activity data of SC3-M2 in the tests with and without SO₂ were given in Table 38-39 and comparison of the T50 values of the two tests were shown in Figure 39. Conversion-temperature profiles of the catalytic activity tests with and without SO₂ are given in Appendix E.

Table 38 Catalytic activity data of SC3-M2 monolithic catalyst in Test 1 without SO₂

Species	Heating			Cooling		
	T50 (C°)	Max. Conv. (%)	Tmax (C°)	T50 (C°)	Max. Conv. (%)	Tmax (C°)
H ₂	260	100	389	220	100	311
CO	329	100	583	217	100	359
O ₂	-	46	596	-	47	520
C ₃ H ₆	307	99	550	247	100	431
C ₃ H ₈	470	98	597	444	99	596

Table 39 Catalytic activity data of SC3-M2 monolithic catalyst in Test 2 with SO₂

Species	Heating			Cooling		
	T50 (C°)	Max. Conv. (%)	Tmax (C°)	T50 (C°)	Max. Conv. (%)	Tmax (C°)
H ₂	268	92	596	258	100	462
CO	348	100	495	305	100	518
O ₂	351	77	596	-	86	430
C ₃ H ₆	340	95	573	330	100	484
C ₃ H ₈	482	90	596	408	91	595

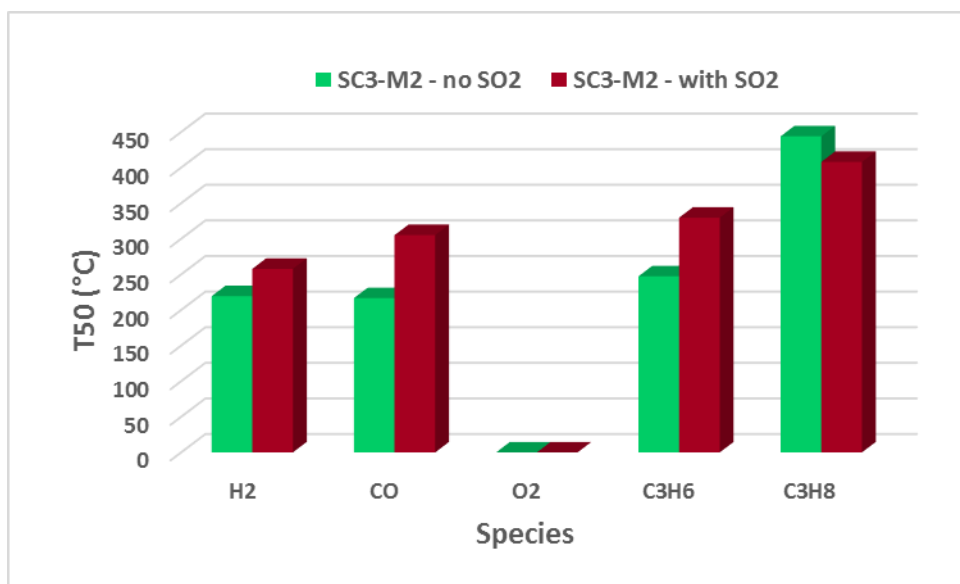


Figure 39 Change in T50 values for SC3-M2 monolithic catalyst upon SO₂ exposure

Comparison between the two tests demonstrated that SO₂ exposure has different effects on the activity of different species. For the conversions of H₂, CO and C₃H₆ species, light-off temperatures were increased when the monolith was exposed to SO₂. On the other hand, C₃H₈ conversions was improved in terms of both T50 and maximum conversion in the presence of SO₂. This fashion is familiar with the activity behavior of the SC1 catalyst, however no such behavior was observed in the test results of SC2 catalyst. Therefore, it has been asserted that Pd containing catalysts have an ability to promote C₃H₈ conversions in the presence of SO₂.

A comparison between the performances of SC1-M2 and SC3-M2 under SO₂ exposure are illustrated on Figure 40.

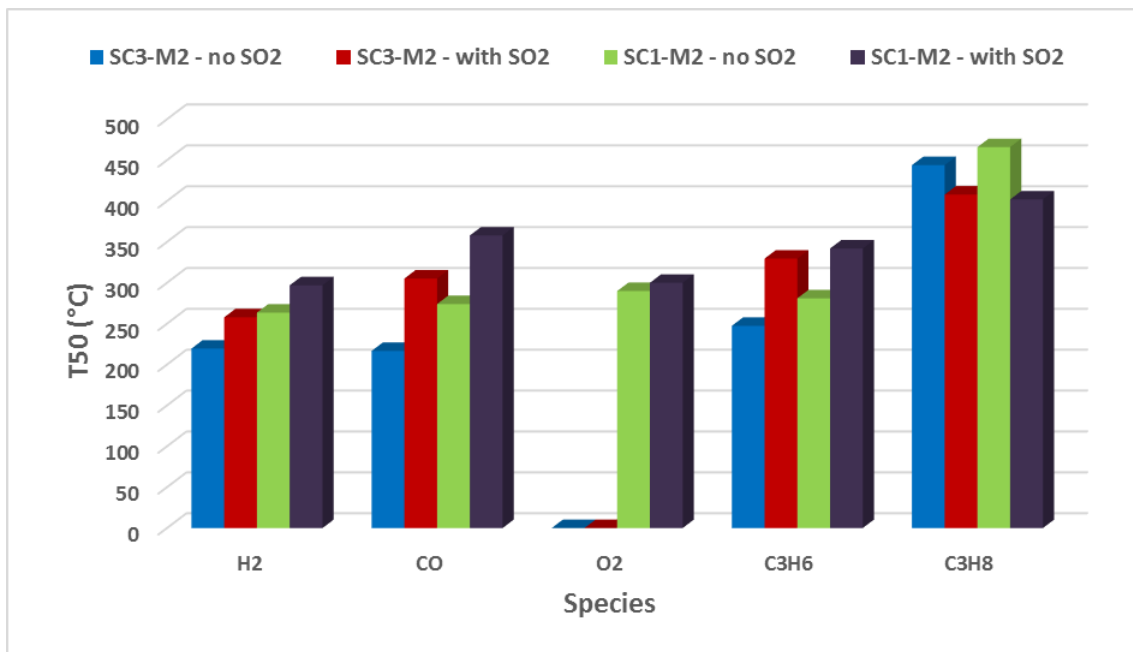


Figure 40 Comparison of T50 values of SC1 and SC3 monolithic catalysts with the effect of SO₂ exposure

After exposing to SO₂, both catalyst shows the same incremental trend in their light-off temperatures. Performances of the two catalyst are almost the same for the conversions of C₃H₆ and C₃H₈ species. However, SC3 has a better activity for CO conversion, even after SO₂ exposure. One possible reason for this behavior is that Mn might be acting as a

SO₂ trap for the catalyst, and accordingly, moderates the extent of sulfur poisoning for Pd.

CHAPTER 6

CATALYST CHARACTERIZATIONS

6.1. ICP-MS Studies

ICP-MS technique was employed to analyze the metal contents of the powdered catalyst slurries. Analysis results of the IMP and SC powder catalyst metal contents with the targeted contents were given in Table 40-41. Small differences between the analysis results and the targeted values can be attributed to metal losses during synthesis, errors in weighing catalyst precursors or miscalculation of the total catalyst weight. No extraordinary deviation from targeted values were encountered in the ICP-MS analysis results.

Table 40 ICP-MS analysis for metal contents of IMP catalysts

		Ce (%)	Pd (%)	Mn (%)	Rh (%)	Al (%)
IMP1	Targeted	19.0	0.200	-	-	34.8
	ICP result	17.8	0.193	-	-	33.4
IMP2	Targeted	19.0	-	0.200	-	34.8
	ICP result	17.9	-	0.195	-	33.5
IMP3	Targeted	19.0	0.172	0.029	-	34.8
	ICP result	17.9	0.169	0.033	-	32.0
IMP4	Targeted	19.0	0.028	0.170	-	34.8
	ICP result	18.0	0.024	0.172	-	33.1
IMP5	Targeted	19.0	-	0.172	0.029	34.8
	ICP result	17.9	-	0.167	0.021	33.4

Table 41 ICP-MS analysis for metal contents of SC catalysts

		Ce (%)	Pd (%)	Mn (%)	Al (%)
SC1	Targeted	19.0	0.182	-	34.7
	ICP result	17.9	0.177	-	33.6
SC2	Targeted	19.0	-	0.922	35.1
	ICP result	18.0	-	0.906	33.9
SC3	Targeted	19.0	0.215	0.944	35.0
	ICP result	17.9	0.206	0.923	33.9

6.1. X-ray Diffraction Studies

X-ray diffraction (XRD) technique was employed to identify the crystal structures of the catalysts and also to determine if any solid phase transformations occur due to thermal aging effects. To begin with, X-ray diffractogram of $\text{Ce}_{0.8}\text{Zr}_{0.2}\text{O}_2$ fresh powder was obtained and displayed on Figure 41.

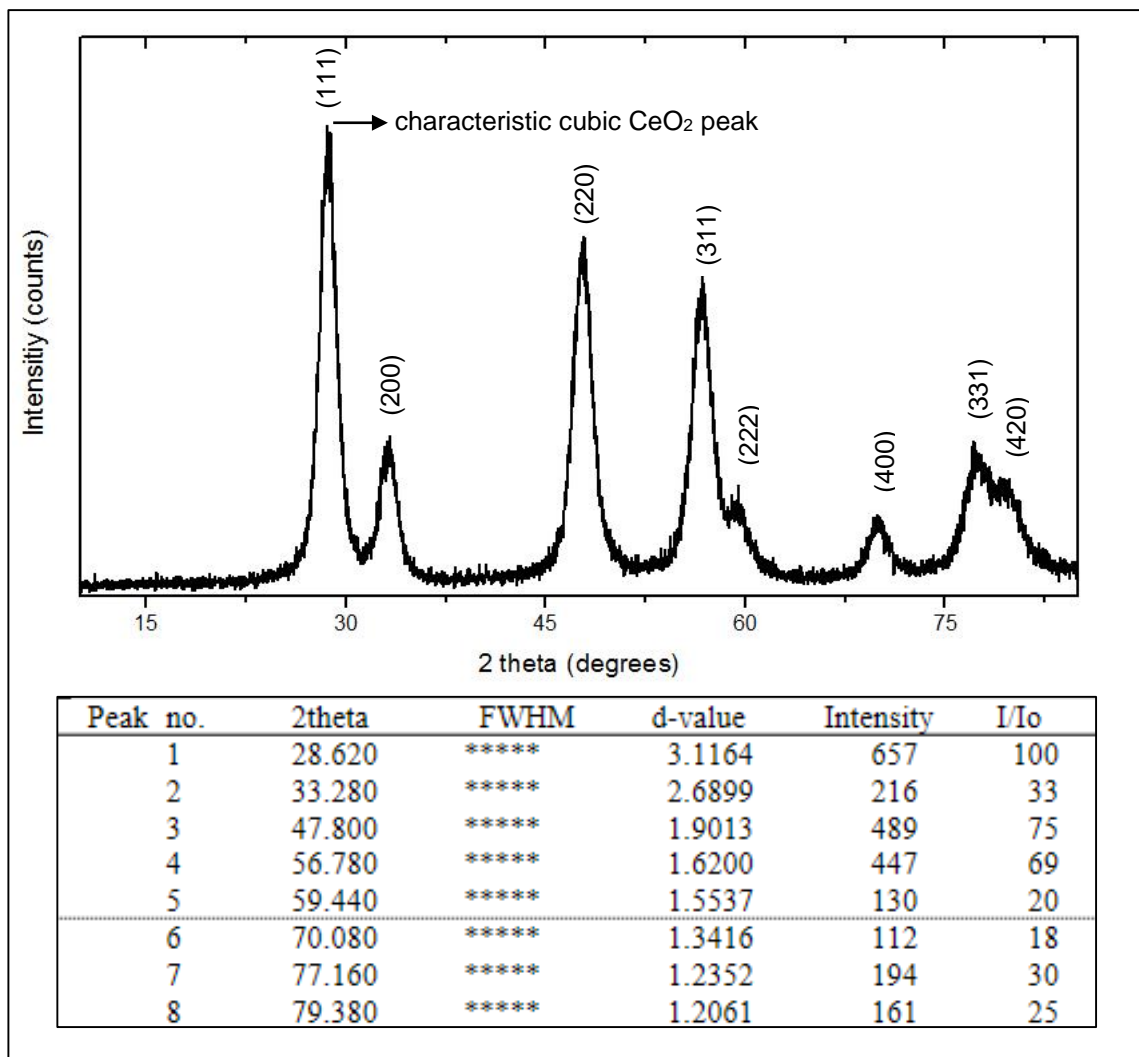


Figure 41 X-ray diffractogram and data of the fresh $\text{Ce}_{0.8}\text{Zr}_{0.2}\text{O}_2$ powder

$\text{Ce}_{0.8}\text{Zr}_{0.2}\text{O}_2$ (JCPDS Card No 28-0271) structure was confirmed by the Qualitative Analysis software of the instrument. In addition, XRD pattern of the $\text{Ce}_{0.8}\text{Zr}_{0.2}\text{O}_2$ sample is similar to the XRD patterns reported by Dhage et al. (2004) and Yu et al. (2003). Highest peak of the pattern corresponds to the cubic fluorite structure of ceria (Damyanova, et al., 2008). The average crystalline size is calculated by the utilization of Scherrer's equation based on this highest peak as 7.01 nm.

X-ray diffraction patterns of all catalysts were compared with the diffraction pattern of $Ce_{0.8}Zr_{0.2}O_2$ to in order to detect any change in crystalline structure due to metal loadings. An example is the XRD pattern of IMP1 fresh powder which is illustrated in Figure 42.

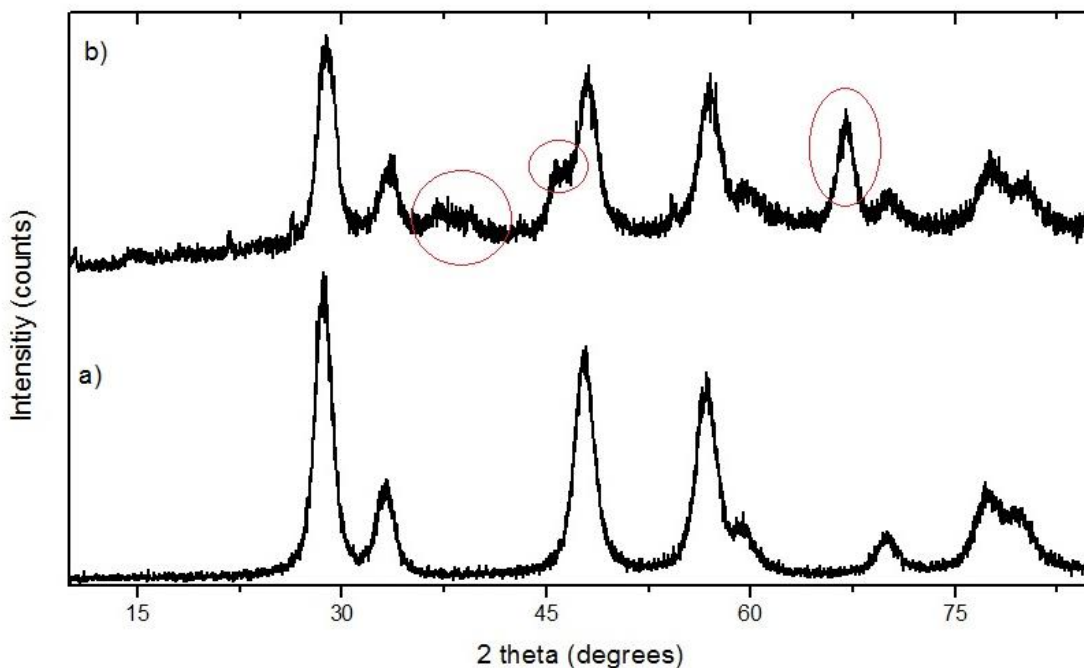


Figure 42 XRD of a) $Ce_{0.8}Zr_{0.2}O_2$ fresh powder b) Catalyst IMP1 fresh powder

Compared to the XRD pattern of CZO, diffraction pattern of catalyst IMP1 has additional peaks in three regions. Analyzing the pattern via software, these peaks are attributed to the presence of $\gamma-Al_2O_3$ in the catalyst composition. Also, Di Monte et al. (2000) presented similar diffraction patterns for CZO/ Al_2O_3 systems (Di Monte, et al., 2000). Other than $\gamma-Al_2O_3$, no diffraction lines for Pd are observed on the pattern indicating a good distribution of Pd on CZO. Similar to IMP1, XRD pattern of another impregnated catalyst IMP2 is given in Figure 43. Again, $\gamma-Al_2O_3$ is detected in the pattern, however there are no diffraction lines belonging to Mn.

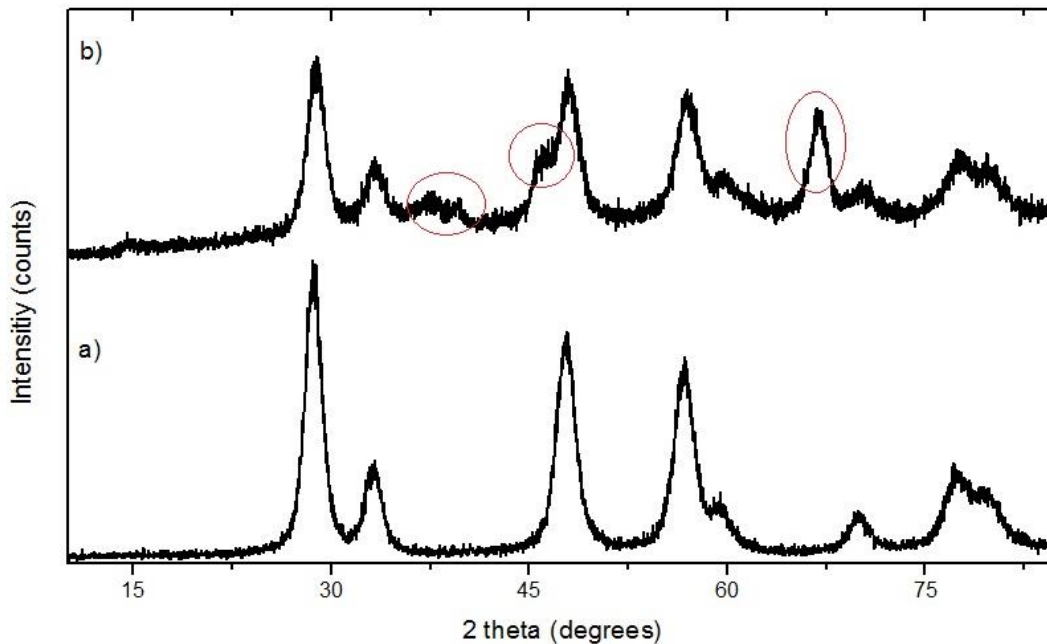


Figure 43 XRD of a) $\text{Ce}_{0.8}\text{Zr}_{0.2}\text{O}_2$ fresh powder b) Catalyst IMP2 fresh powder

No traces of metals were detected in the X-ray diffraction patterns of the other impregnated catalysts IMP3, IMP4 and IMP5, as well. Corresponding XRD patterns are given in Appendix.

Similar X-ray diffraction patterns were also obtained with the analysis of the catalysts synthesized via solution combustion method. An example is the XRD pattern of SC1 fresh powder which is shown in Figure 44. XRD patterns of SC2 and SC3 are given in Appendix. Once again, additional diffraction lines were attributed to $\gamma\text{-Al}_2\text{O}_3$, and no Pd or Mn diffraction peaks were detected in the XRD patterns of these catalysts indicating a good distribution/substitution of metals on the surface.

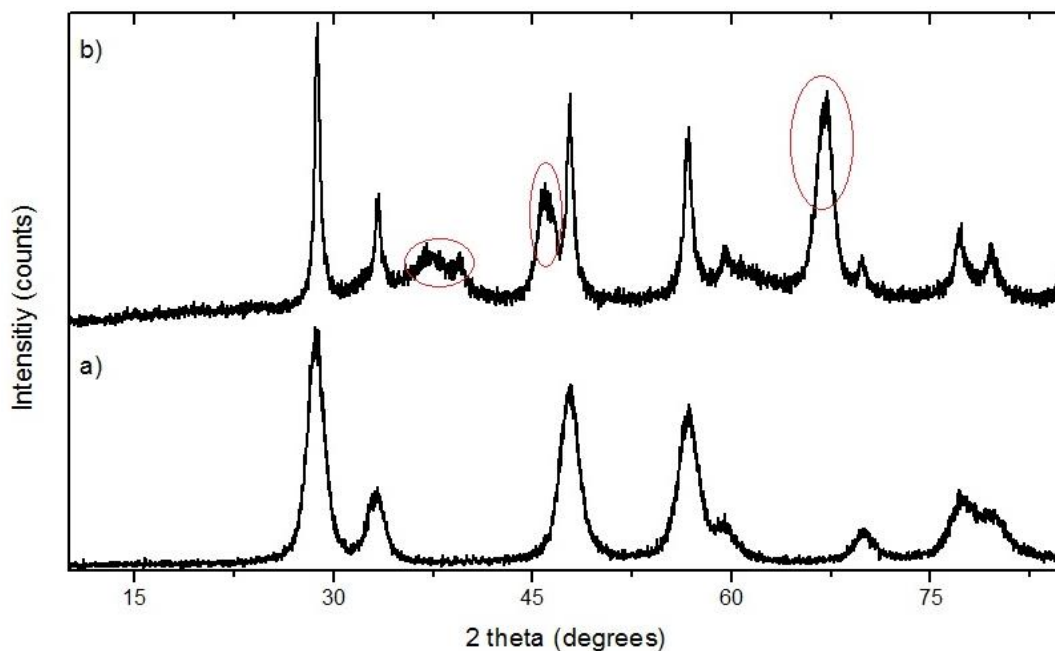


Figure 44 XRD of a) $\text{Ce}_{0.8}\text{Zr}_{0.2}\text{O}_2$ fresh powder b) Catalyst SC1 fresh powder

In order to observe surface modifications that might have occurred due to thermal aging, XRD analyses were also performed with the catalyst samples aged at 900°C and compared with the diffraction patterns of the fresh samples. As an example, XRD patterns of the fresh and aged IMP1 powder samples are shown in Figure 45.

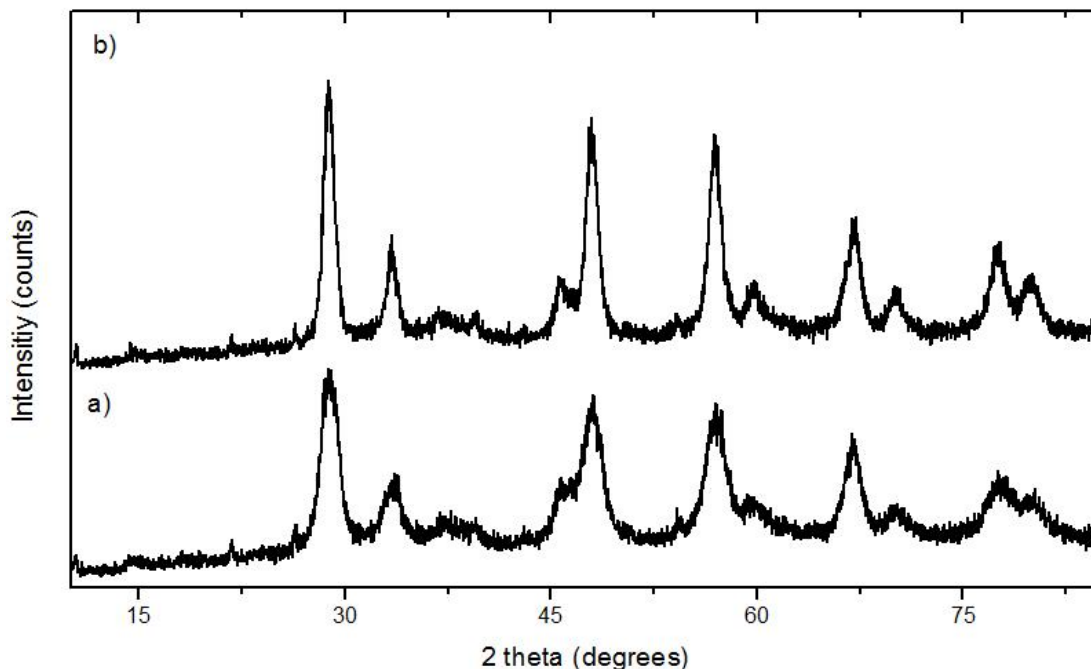


Figure 45 XRD of a) Fresh IMP1 powder b) IMP1 powder aged at 900°C

When the fresh and aged X-ray diffraction patterns of IMP1 were compared, additional peaks as indicators of phase changes were not observed in the aged catalyst sample. All catalysts presented in this study showed the same behavior and maintained high thermal stability with no solid-solid phase transformations after subjected to thermal aging at 900°C. Fresh and aged XRD patterns of the corresponding catalyst samples can be viewed in Appendix F.

Although thermal aging did not induce any phase transformations, particle sizes of all samples were increased upon aging. Sharpening of the peaks in diffraction patterns of aged samples are the indication of particle growth. Crystallite sizes of the fresh and aged catalyst samples were determined using Scherrer's equation and given in Table 42.

Table 42 Particle sizes of the fresh and aged catalyst samples calculated based on the cubic ceria peak in XRD patterns

Catalyst ID	Fresh sample particle size (nm)	Aged sample particle size (nm)
IMP1	7.33	11.65
IMP2	7.26	11.76
IMP3	7.06	11.22
IMP4	7.94	11.88
IMP5	7.41	11.35
SC1	13.02	14.39
SC2	9.22	15.77
SC3	15.01	17.03

Particle sizes of the impregnated catalysts are very close to each other in both fresh and aged samples. This is because CZO was synthesized at once and metals were impregnated on the same CZO support in each catalyst. However, the effect of synthesis method on particle size is observed with the catalysts synthesized via solution combustion method. Clearly, SC catalysts are more thermally stable but IMP catalysts have smaller particle sizes.

6.2. TEM Characterizations

Microstructures of the powder catalyst samples were analyzed using a JEOL JEM 2100F model High Resolution Transmission Electron Microscope (HRTEM) operating at 200 kV. HRTEM images of IMP3 and SC3 catalyst samples at different magnifications are given in Figure 46 and Figure 47.

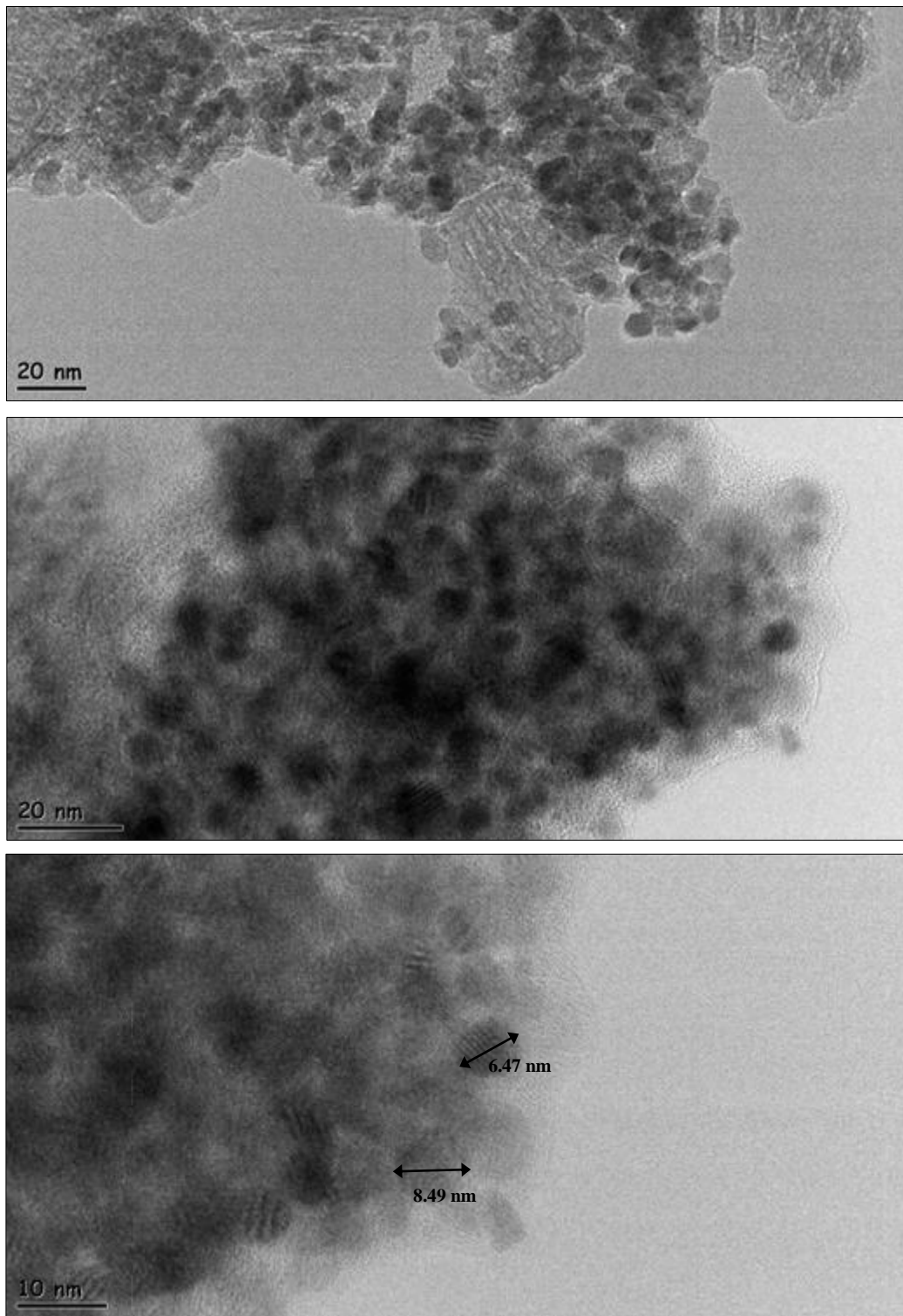


Figure 46 HRTEM images of the fresh IMP3 catalyst powder

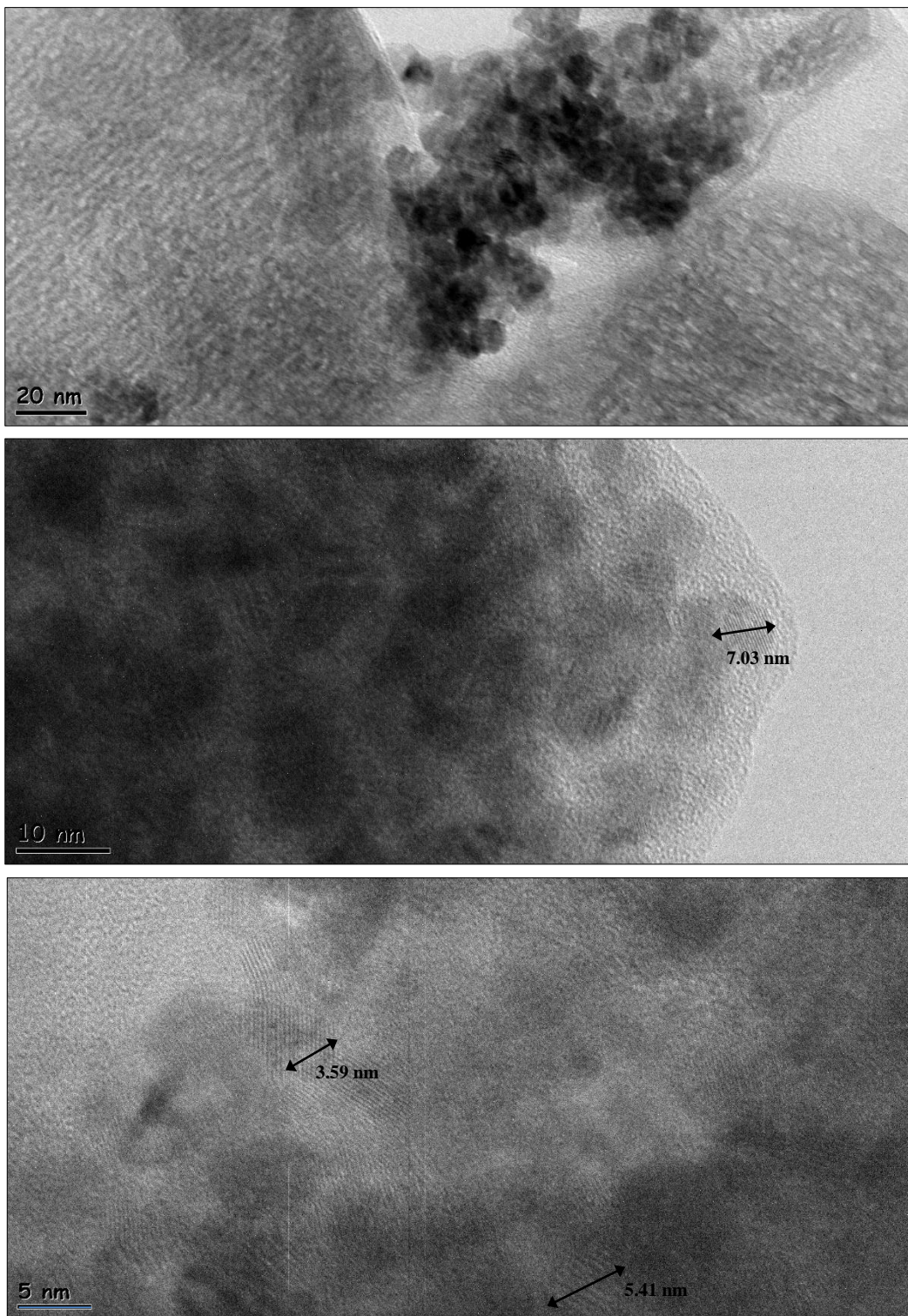


Figure 47 HRTEM images of the fresh SC3 catalyst powder

Looking at the HRTEM images, dispersion of nanocrystalline ceria structures on alumina matrix can clearly be observed. Similar nanostructures of ceria were reported by (Wang, et al., 2011), (Yu, et al., 2011) and (Kurnatowska, et al., 2012). In both samples, ceria crystals does not exhibit a specific type of crystal form, hence various types of crystal planes are exposed. Due to very low loading and high dispersion on the surface, Pd cannot be identified explicitly on these images.

Further characterization of the microstructure was performed via Energy Dispersive X-ray (EDX) analysis. Elemental composition of the SC3 catalyst sample was investigated with EDX point-analysis in three different regions. Spectral compositions of these three regions are given in Figure 48.

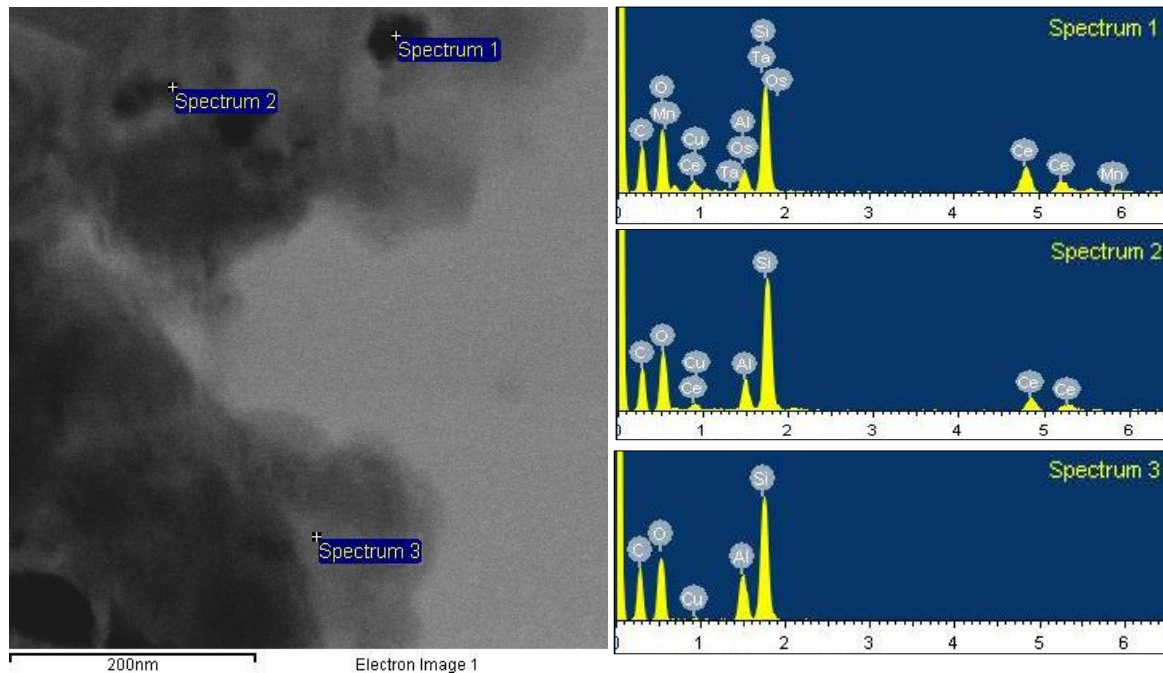


Figure 48 EDX analysis of different regions on SC3 catalyst sample

First region to be evaluated by EDX was selected as it is rich crystalline structures. EDX analysis with Spectrum 1 confirms the presence of Ce, Mn and Al elements in that region. In a similar region, Spectrum 2 contains Ce and Al elements only. Absence of Mn in Spectrum 2 indicates that Mn dispersion changes in different regions. Finally, elemental analysis of the matrix was performed on the third region. Spectrum 3 confirms

that only Al element is present in the matrix. Interestingly, Zr is not detected in all three regions. It might be interfered by another element in the spectra and cannot be observed. Additional elements present on the spectra are probably due to some impurities caused by precursors used in catalyst synthesis or spectral interference of some elements. EDX is not a precise technique for elemental analysis yet it provides a general idea for the structural composition.

6.3.BET Characterizations

Surface area measurements were performed with single point Brunauer–Emmet–Teller method (BET) and given in Table 43 for fresh and aged samples of IMP3 and SC3 representing the catalysts prepared by two synthesis methods

Table 43 Surface areas of IMP3 and SC3 catalysts for fresh and aged samples

Catalyst	IMP3 Fresh	IMP3 Aged at 900°C	SC3 Fresh	SC3 Aged at 900°C
BET Surface Area (m²/g)	80.88	52.37	80.34	46.64

As it can be inferred from that results, fresh samples of both catalysts have quite high surface areas. However, once they were subjected to thermal aging, surface areas substantially decreased. Thus, activity losses observed in thermally aged catalysts might be attributed to the decrements in surface areas.

CHAPTER 7

CONCLUSIONS

This thesis work was constructed upon the investigation of the catalytic performances of three way catalysts by means of both quantum mechanical calculations and experimental studies. Density functional theory with generalized gradient approximation (GGA) was implemented by Vienna Ab Initio Package (VASP) software to model the reaction geometries and energetics on catalyst surfaces. Once the outputs of computational studies were comprehended, experimental studies were conducted in a deeper extent with similar catalyst structures to see if the results of the theoretical studies were consistent with reality. Catalysts were synthesized using two different techniques; impregnation and solution combustion synthesis. Laboratory scale monoliths were washcoated with catalysts and catalytic activity tests were performed in a dynamic test system simulating automobile exhaust conditions. Comparing the light-off temperatures, performances of the catalysts were evaluated in terms of activity changes upon thermal aging and SO₂ exposure.

The main focus of this study was to investigate the effect of manganese doping in three way catalyst compositions. In DFT computations, Mn, Pd and Rh metals were atomically substituted in Ce_{0.75}Zr_{0.25}O₂ (110) structure (CZO) and CO oxidation mechanisms were investigated on three model surfaces; (A)-Mn/Ce_{0.75}Zr_{0.25}O₂, (B)-Pd+Mn/Ce_{0.75}Zr_{0.25}O₂ and (C)-Rh+Mn/Ce_{0.75}Zr_{0.25}O₂. On all surfaces, two CO molecules were exothermically oxidized to two CO₂ molecules by using a surface oxygen and

creating and oxygen vacancy. The vacancy was then filled with an oxygen molecule adsorbing on the vacant site and hereby, oxygen storage capacity (OSC) of ceria was proved. Energy of vacancy formation on surface (B)-Pd+Mn/CZO was found to be the lowest among others with a negative value of -12.09 kcal/mole. When compared to the vacancy formation energy of 43.7 kcal/mole on Pd substituted CZO (Gerçeker & Önal, 2013), a synergism between Pd and Mn was identified upon enhancement of the OSC. A collaborative act was also observed on surface (C)-Rh+Mn/CZO, however not as much as Pd and Mn synergism. Also, when the CO oxidation energetics on three surface models were compared, it was clearly seen that CO oxidation is more energetically favored on surface (B)-Pd+Mn/CZO and this trend is attributed to the enhancement of the OSC component.

In order to interrelate with the theoretical results, experimental studies were performed with Pd, Mn and Rh containing catalysts synthesized via two different methods. To keep in mind, surface models used in DFT calculations should not be considered as identical to the catalysts synthesized for experimental studies, nevertheless they represent a general TWC structure with desired compositions and give very important clues upon catalytic activity.

The first set of catalysts were synthesized by impregnation method and catalytic activity tests were performed under the effect of thermal aging. First catalyst, IMP1 was prepared with 0.70 wt % Pd loading on CZO and as a conventional Pd containing TWC, catalytic performance of IMP1 was successful. The second impregnated catalyst, IMP2 was prepared with 0.70 wt % Mn loading on CZO in order to see if a Mn only catalyst was catalytically active. Fresh IMP2 catalyst was capable of converting all species with reasonable light-off temperatures. Hereby, CO oxidation ability of a Mn-CZO catalyst was proved experimentally. When the catalyst was subjected to thermal aging, irreversible activity losses were encountered in CO and C₃H₈ conversions. Therefore, Mn-only catalyst IMP2 was found to be insufficient. A third impregnated catalyst, IMP3 was synthesized with combination of the two metals Pd and Mn with loadings of 0.60 wt % and 0.10 wt %, respectively. Under the effect of thermal aging, activity trend of IMP3

was similar to IMP1 in the tests with no SO₂ presence. When the light-off values of fresh catalysts are compared for CO conversion, a slightly better activity was observed with IMP3, and this is in accordance with the results of the computational studies. IMP3, also had a higher performance than IMP1 in C₃H₆ and C₃H₈ conversions. However when tests were performed in the presence of SO₂, this time IMP3 yielded a lesser performance than IMP1 with slightly higher light-off temperatures, due to the susceptibility of Mn to SO₂ poisoning. Combination of Pd and Mn was further investigated with the catalyst IMP4 having 0.10 wt % Pd and 0.60 wt % Mn in its composition. Performance of IMP4 for CO and C₃H₆ conversions was not as much as the performances of IMP1 and IMP3 catalysts, but still quite good. As the last one of the impregnated catalysts, IMP5 was synthesized with 0.10 wt % Rh and 0.60 wt % Mn. Fresh IMP5 catalyst was capable of converting all species, catalytic activity was dramatically damaged after thermal aging. Still, CO oxidation ability of a Rh and Mn containing TWC was proved experimentally. In addition, a comparison between IMP4 and IMP5 catalysts revealed that the combination of Pd and Mn is a better choice than Rh and Mn combination which supported the findings of DFT studies.

The second set of catalysts were synthesized via solution combustion technique. This technique postulates formation of single phase Ce_{1-x}M_xO_{2-δ} structure with ionic substitutions of metals (Hedge, et al., 2008). The first catalyst SC1 was prepared with only Pd having a composition of Ce_{0.79}Zr_{0.2}Pd_{0.01}O₂ and similar to the other Pd-only catalyst IMP1, catalytic performance of SC1 was quite good. The second catalyst SC2 having a composition of Ce_{0.80}Zr_{0.1}Mn_{0.1}O₂ was synthesized with only Mn, but this time its concentration was kept 10 fold higher (in mole basis) than the amount of Pd in SC1 catalyst. Fresh SC2 could provide high conversion values for the majority of the species, still it could not catch up with the performance of SC1 even with that much of Mn content. Also, thermal aging severely damaged catalytic activity and similar to the performance IMP2, activity losses were encountered in CO and C₃H₈ conversions after aging the catalyst. Finally, SC3 having a composition of Ce_{0.79}Zr_{0.1}Mn_{0.1}Pd_{0.01}O₂ was prepared in order to investigate the collaboration of Pd and Mn on catalytic activity. Activity trend of SC3 was very similar to SC1 in between the test results of fresh and

aged catalysts, yet a superior performance was observed with SC3 for the conversion of all species. Hence, similar to IMP3 catalyst, contribution of Mn was also seen with SC3 catalyst which is again in compliance with the findings of theoretical studies.

REFERENCES

- Anderson, J., 1975. *Structure of Metallic Catalysts*. London: Academic Press.
- Armor, J., 1992. Environmental catalysis. *Applied Catalysis B: Environmental*, 1(4), pp. 221-256.
- Bera, P. et al., 2000. Ionic Dispersion of Pt and Pd on CeO₂ by Combustion Method: Effect of Metal–Ceria Interaction on Catalytic Activities for NO Reduction and CO and Hydrocarbon Oxidation. *Journal of Catalysis*, Volume 196, p. 293–301.
- Blöchl, P., 1994. Projector augmented-wave method. *Physical Review B*, 50(24), p. 17953.
- Bunluesin, T., Putna, E. & Gorte, R., 1996. A comparison of CO oxidation on ceria-supported Pt, Pd, and Rh. *Catalysis Letters*, 41(1), pp. 1-5.
- Cen, W. et al., 2012. A theoretic insight into the catalytic activity promotion of CeO₂ surfaces by Mn doping. *Phys. Chem. Chem. Phys.*, Issue 14, pp. 5769-5777.
- Cullity, B. & Stock, S., 2001. *Elements of X-ray Diffraction*. 3rd ed. New York: Prentice Hall.
- Damyanova, S. et al., 2008. Study of the surface and redox properties of ceria–zirconia oxides. *Applied Catalysis A: General*, Volume 337, p. 86–96.
- Dhage, S., Gaikwad, S., Muthukumar, P. & Ravi, V., 2004. Synthesis of Ce_{0.75}Zr_{0.25}O₂ by citrate gel method. *Materials Letters*, Volume 58, p. 2704– 2706.

Di Monte, R., Fornasiero, P., Graziani, M. & Kaspar, J., 1998. Oxygen storage and catalytic NO removal promoted by CeO₂-containing. *Journal of Alloys and Compounds*, pp. 877-885.

Di Monte, R. et al., 2000. Pd/CeO₂:6ZrO₂:4Al₂O₃ as advanced materials for three-way catalysts Part 1. Catalyst characterisation, thermal stability and catalytic activity in the reduction of NO by CO. *Applied Catalysis B: Environmental*, Volume 24, p. 157–167.

Di Monte, R. & Kaspar, J., 2005. Heterogeneous environmental catalysis – a gentle art: CeO₂–ZrO₂ mixed oxides as a case history. *Catalysis Today*, Issue 100, pp. 27-35.

Ertl, G., Knozinger, H. & Weitkamp, J., 1999. *Environmental Catalysis*. s.l.:Wiley-VCH.

Farrauto, R. & Heck, R., 1999. Catalytic converters: state of the art and perspectives. *Catalysis Today*, Volume 51, pp. 351-360.

Fogler, H., 2006. *Elements of chemical reaction engineering*. 4th ed. Massachusetts: Prentice Hall.

Fornasiero, P. et al., 2000. Thermal Stability and Oxygen Storage Capacity of Noble Metal/Ceria-Zirconia Catalysts for the Automotive Converters with the On-Board-Diagnostics (OBD). *Studies in Surface Science and Catalysis*, Volume 130, p. 1355–1360.

Gandhi, H. & Narula, C., 1997. History of monolithic automotive catalyst technology. *Chem. Sustainable Dev*, 5(3), pp. 291-302.

Gennari, F., Montini, T., Fornasiero, P. & Gamboa, J. A., 2008. Reduction behavior of nanoparticles of Ce_{0.8}Zr_{0.2}O₂ produced by different approaches. *International Journal of Hydrogen Energy*, Issue 33, pp. 3549-3554.

Gerceker, D., 2013. *Removal of Hydrocarbons, Carbon Monoxide and Nitric Oxides in Automotive Exhaust with Three Way Catalytic Converter*. Ankara: METU.

Gerçeker, D. & Önal, I., 2013. A DFT study on CO oxidation on Pd₄ and Rh₄ clusters and adsorbed Pd and Rh atoms on CeO₂ and Ce_{0.75}Zr_{0.25}O₂ supports for TWC adsorbed Pd and Rh atoms on CeO₂ and Ce_{0.75}Zr_{0.25}O₂ supports for TWC. *Applied Surface Science*, Issue 285P, pp. 927-936.

Gerward, L. & Olsen, J., 1993. Powder diffraction analysis of cerium dioxide at high pressure. *Powder Diffraction*, 8(2), pp. 127-129.

Gonzalez-Marcos, M. et al., 2012. On the effect of reduction and ageing on the TWC activity of Pd/Ce_{0.68}Zr_{0.32}O₂ under simulated automotive exhausts. *Catalysis Today*, Issue 180, pp. 88-95.

Granados, M. et al., 2005. Modification of a three-way catalyst washcoat by aging: A study along the longitudinal axis. *Applied Surface Science*, Volume 252, pp. 8442-8450.

Gupta, A., Waghmare, U. & Hedge, M., 2010. Correlation of Oxygen Storage Capacity and Structural Distortion in Transition-Metal-, Noble-Metal-, and Rare-Earth-Ion-Substituted CeO₂ from First Principles Calculation. *Chem. Mater.*, Issue 22, pp. 5184-5198.

Hedge, M., Madras, G. & Patil, K., 2008. Noble Metal Ionic Catalysts. *Accounts of Chemical Research*, 42(6), pp. 704-712.

Heine, T., Joswig, J. & Gelessus, A., 2009. *Computational chemistry workbook: learning through examples*. Weinheim: Wiley-VCH.

Hickey, N. et al., 2003. Reactivation of aged model Pd/Ce_{0.68}Zr_{0.32}O₂ three-way catalyst by high. *Chem. Commun.*, pp. 196-197.

Hsu, L.-C., Tsai, M.-K., Lu, Y.-H. & Chen, H.-T., 2013. Computational Investigation of CO Adsorption and Oxidation on Mn/CeO₂(111) Surface. *J. Phys. Chem. C*, Issue 117, pp. 433-441.

Jensen, F., 2007. *Introduction to Computational Chemistry*. 2nd ed. West Sussex: John Wiley & Sons Ltd.

Kaspar, J. & Fornasiero, P., 2003 b. Nanostructured materials for advanced automotive de-pollution catalysts. *Journal of Solid State Chemistry*, Issue 171, pp. 19-29.

Kaspar, J. et al., 2003 a. Effect of ZrO₂ content on textural and structural properties of CeO₂ - ZrO₂ solid solutions made by citrate complexation route. *Inorganica Chimica Acta*, Issue 349, pp. 217-226.

Kaspar, J., Fornasiero, P. & Hickey, N., 2003. Automotive catalytic converters: current status and some perspectives. *Catalysis Today*, Volume 77, pp. 419-449.

Kresse, G. & Furthmüller, J., 1996. Efficiency of ab initio total energy calculations for metals and semiconductors using plane wave basis set. *Computational Materials Science*, 6(1), pp. 15-50.

Kresse, G. & Hafner, J., 1994. Ab initio molecular dynamics simulation of the liquid metal amorphous semiconductor transition in germanium. *Physical Review B*, 49(20), pp. 14251-14269.

Kurnatowska, M., Kepinski, L. & Mista, W., 2012. Structure evolution of nanocrystalline Ce_{1-x}Pd_xO_{2-y} mixed oxide in oxidizing and reducing atmosphere: Reduction-induced activity in low-temperature CO oxidation. *Applied Catalysis B: Environmental*, Volume 117-118, p. 135– 147.

Lachman, I. et al., 1994. *Process for removal of hydrocarbons carbon monoxide, and oxides of nitrogen from oxygen-containing waste gas using molecular sieve-palladium-platinum catalyst on a substrate*. U.S., Patent No. 5,292,991.

Lambrou, P. et al., 2005. The effects of the use of weak organic acids on the improvement of oxygen storage and release properties of aged commercial three-way catalysts. *Applied Catalysis B: Environmental*, Volume 59, pp. 1-11.

Lassi, U., 2003. *Deactivation correlations of Pd/Rh three way catalysts designed for Euro IV emission limits. Effects of ageing atmosphere, temperature and time.* Oulu: University of Oulu.

Lewars, E., 2003. *Computational chemistry: introduction to the theory and applications of molecular and quantum mechanics.* 1st ed. Dordrech: Kluwer Academic Publishers.

Li, G. et al., 2011. Effect of iron doping into CeO₂–ZrO₂ on the properties and catalytic behaviour of Pd-only three-way catalyst for automotive emission control. *Journal of Hazardous Materials*, Volume 189, p. 911–920.

Li, G., Wang, Q., Zhao, B. & Zhou, R., 2012. A new insight into the role of transition metals doping with CeO₂–ZrO₂ and its application in Pd-only three-way catalysts for automotive emission control. *Fuel*, Issue 92, pp. 360-368.

Martinez-Arias, A., Conesa, J., Fernandez-Garcia, M. & Anderson, J., 2012. Supported Metals in Vehicle Emission Control. In: *Supported Metals in Catalysis.* s.l.:Imperial College Press, pp. 493-552.

Matsumoto, S., 2004. Recent advances in automobile exhaust catalysts. *Catalysis Today*, Volume 90, pp. 183-190.

McDouall, J., 2013. *Computational Quantum Chemistry : Molecular Structure and Properties in Silico.* Cambridge: RSC Publishing.

Murugan, B. & Ramaswamy, A., 2005. Nature of Manganese Species in Ce_{1-x}Mn_xO₂-Solid Solutions Synthesized by the Solution Combustion Route. *Chem. Mater.*, Volume 17, pp. 3983-3993.

Nguefack, M., Popa, A., Rossignol, S. & Kappenstein, C., 2003. Preparation of alumina through a sol–gel process. Synthesis, characterization, thermal evolution and model of intermediate boehmite. *Phys. Chem. Chem. Phys.*, Volume 5, p. 4279–4289.

Nijhuis, T. et al., 2001. Preparation of Monolithic Catalysts. *Catalysis Reviews*, 43(4), pp. 345-380.

Nolan, M. et al., 2005 a. Density functional theory studies of the structure and electronic structure of pure and defective low index surfaces of ceria. *Surface Science*, Volume 576, pp. 217-229.

Nolan, M., Parker, S. C. & Watson, G. W., 2005 b. The electronic structure of oxygen vacancy defects at the low index surfaces of ceria. *Surface Science*, Volume 595, pp. 223-232.

Parr, R. & Yang, W., 1994. *Density-functional theory of atoms and molecules*. s.l.:Oxford University Press.

Perdew, J., 1992. Atoms, molecules, solids and surfaces: applications of the generalized gradient approximation for exchange and correlation. *Physical Review B*, 46(11), p. 6671.

Pintos, D. G., Juan, A. & Irigoyen, B., 2013. Mn-Doped CeO₂: DFT+U Study of a Catalyst for Oxidation Reactions. *J. Phys. Chem. C*, Issue 117, pp. 18063-18073.

Pratt, A. & Cairns, C., 1977. Noble Metal Catalysts on Metallic Substrates. *Platinum Metals Rev.*, 21(3), pp. 74-83.

Priolkar, K. et al., 2002. Formation of Ce_{1-x}Pd_xO_{2- δ} Solid Solution in Combustion-Synthesized Pd/CeO₂ Catalyst: XRD, XPS, and EXAFS Investigation. *Chem. Mater.*, Volume 14, pp. 2120-2128.

Sebastian, M., 2008. *Dielectric Materials for Wireless Communication*. First ed. Amsterdam: Elsevier.

Seminario, J., 1995. An introduction to density functional theory in chemistry. In: *Modern Density Functional Theory: A Tool For Chemistry*. s.l.:Elsevier Science..

Sholl, D. & Steckel, J., 2009. *Density functional theory: a practical introduction*. s.l.:Wiley.

- Summers, J., Williamson, W. & Henk, M., 1988. Uses of Palladium in Automotive Emission Control Catalysts. *SAE Technical Paper Series 880281*.
- Tang, Y. et al., 2010. First-principles investigation on redox properties of M-doped CeO₂ (M=Mn,Pr,Sn,Zr). *Physical review B*, Issue 82, p. 125104.
- Taylor, K., 1993. Nitric Oxide Catalysis in Automotive Exhaust Systems. *Catalysis Reviews: Science and Engineering*, 35(4), pp. 457-481.
- Trimm, D., 1995. Materials selection and design of high temperature catalytic. *Catalysis Today*, Issue 26, pp. 231-238.
- Trovarelli, A., 1996. Catalytic Properties of Ceria and CeO₂-Containing Materials. *Catalysis Reviews: Science and Engineering*, 38(4), pp. 439-520.
- Twigg, M., 2011. Catalytic control of emissions from cars. *Catalysis Today*, Volume 163, pp. 33-41.
- Wang, H.-F. et al., 2009. A Model to Understand the Oxygen Vacancy Formation in Zr-Doped CeO₂: Electrostatic Interaction and Structural Relaxation. *J. Phys. Chem. C*, Volume 113, pp. 10229-10232.
- Wang, J. et al., 2012. Steam effects over Pd/Ce_{0.67}Zr_{0.33}O₂-Al₂O₃ three-way catalyst. *Journal of Rare Earths*, 30(8), p. 748.
- Wang, Q. et al., 2011. Effect of synthesis method on the properties of ceria–zirconia modified alumina and the catalytic performance of its supported Pd-only three-way catalyst. *Journal of Molecular Catalysis A: Chemical*, Volume 344, p. 132– 137.
- Yang, Z., Fu, Z., Wei, Y. & Hermansson, K., 2008. The electronic and reduction properties of Ce_{0.75}Zr_{0.25}O₂(110). *Chemical Physics Letters*, 450(4-6), pp. 286-291.
- Yang, Z., Lu, Z., Luo, G. & Hermansson, K., 2007. Oxygen vacancy formation energy at the Pd/CeO₂(111) interface. *Physics Letters A*, Issue 369, pp. 132-139.

Young, D., 2001. *Computational Chemistry: A Practical Guide for Applying Techniques to Real-World Problems*. s.l.:John Wiley & Sons, Inc.

Yu, J., Zhang, L. & Lin, J., 2003. Direct sonochemical preparation of high-surface-area nanoporous ceria and ceria–zirconia solid solutions. *Journal of Colloid and Interface Science*, Volume 260, p. 240–243.

Yu, Q. et al., 2011. Mesoporous ceria–zirconia–alumina nanocomposite-supported copper as a superior catalyst for simultaneous catalytic elimination of NO–CO. *Catalysis Communications*, Volume 12, p. 1311–1317.

Zhang, M., Jiang, D. & Jiang, H., 2012. Enhanced oxygen storage capacity of Ce_{0.88}Mn_{0.12}O_y compared to CeO₂: An experimental and theoretical investigation. *Materials Research Bulletin*, Issue 47, pp. 4006-4012.

Zhao, B. et al., 2010. Preparation of Ce_{0.67}Zr_{0.33}O₂ mixed oxides as supports of improved Pd-only three-way catalysts. *Applied Catalysis B: Environmental*, Issue 96, pp. 338-349.

APPENDICES

APPENDIX A

SAMPLE VASP SCRIPTS

A1. Sample VASP Codes for Bulk Relaxation

A1.1. INCAR File

SYSTEM = CeO2

!ISTART = 0

PREC = HIGH

ISIF = 3

IBRION = 1;

NSW = 150

LREAL = AUTO

ISMEAR = 0; SIGMA = 0.01;

ENCUT = 500

ALGO = FAST

EDIFFG = -0.001

A1.2. KPOINTS File

K-Points

0

Monkhorst Pack

18 18 18

0 0 0

A1.3. POSCAR File

Ce O

1.0000000000000000

5.4110000000000000 0.0000000000000000 0.0000000000000000

0.0000000000000000 5.4110000000000000 0.0000000000000000

0.0000000000000000 0.0000000000000000 5.4110000000000000

Ce O

4 8

Selective dynamics

Cartesian

0.0000000000 0.0000000000 0.0000000000 T T T

2.7055000000 2.7055000000 0.0000000000 T T T

0.0000000000 2.7055000000 2.7055000000 T T T

2.7055000000 0.0000000000 2.7055000000 T T T

1.3527500000 1.3527500000 1.3527500000 T T T

4.0582500000 1.3527500000 1.3527500000 T T T

4.0582500000 4.0582500000 1.3527500000 T T T

1.3527500000 4.0582500000 1.3527500000 T T T

1.3527500000 4.0582500000 4.0582500000 T T T

1.3527500000	1.3527500000	4.0582500000	T T T
4.0582500000	1.3527500000	4.0582500000	T T T
4.0582500000	4.0582500000	4.0582500000	T T T

A2. Sample VASP Codes for Surface Optimizations

A2.1. INCAR File

```
EDIFFG = -0.015  
IBRION = 2  
!POTIM = 0.2;  
!NFREE = 20  
ISMEAR = 0; SIGMA = 0.01;  
LREAL = Auto  
ENCUT = 500  
IDIPOL = 3  
LDIPOL = .TRUE.  
NSW = 300  
ALGO=FAST
```

A2.2. KPOINTS File

```
K-Points  
0  
Monkhorst Pack  
4 4 1  
0 0 0
```

A2.3. POSCAR File

Zr Mn Ce O

1.0000000000000000

10.758200000000000 0.000000000000000 0.000000000000000

0.000000000000000 7.607199999999999 0.000000000000000

0.000000000000000 0.000000000000000 30.705400000000000

4 1 11 32

Selective dynamics

Cartesian

7.1721690000 0.9509000000 0.0000000000 F F F

9.8334660000 2.8118120000 1.6140000000 T T T

7.1461460000 0.9640330000 4.0863200000 T T T

9.8328070000 2.8190320000 5.1911300000 T T T

9.8343120000 6.6739520000 5.4961640000 T T T

1.7930690000 0.9509000000 0.0000000000 F F F

1.7930690000 4.7545000000 0.0000000000 F F F

7.1721690000 4.7545000000 0.0000000000 F F F

9.8355120000 6.6860110000 1.7336050000 T T T

4.5171480000 2.8293250000 1.7557120000 T T T

4.5182920000 6.6783790000 1.7651870000 T T T

7.1953120000 4.7151990000 3.8134230000 T T T

1.7694870000 4.7346060000 3.8646550000 T T T

1.7871380000 0.9693230000 3.8693900000 T T T

4.4997660000 6.6571040000 5.5397140000 T T T

4.4935550000 2.8551090000 5.5666410000 T T T

0.4482940000 2.8527000000 0.0000000000 F F F

0.4482940000	6.6563000000	0.0000000000	F F F
5.8273940000	2.8527000000	0.0000000000	F F F
5.8273940000	6.6563000000	0.0000000000	F F F
3.1378440000	2.8527000000	0.0000000000	F F F
3.1378440000	6.6563000000	0.0000000000	F F F
8.5169440000	2.8527000000	0.0000000000	F F F
8.5169440000	6.6563000000	0.0000000000	F F F
8.5469580000	1.0042740000	1.5814460000	T T T
6.0011630000	0.9482330000	1.6899070000	T T T
0.4362560000	4.7077780000	1.7876750000	T T T
0.4372980000	1.0077780000	1.8061340000	T T T
8.5412030000	4.6795550000	1.8322220000	T T T
3.1215200000	4.7542900000	1.8359600000	T T T
3.1313570000	0.9494040000	1.8448930000	T T T
5.8729010000	4.7568800000	1.8675220000	T T T
8.5219880000	2.6747180000	3.5972370000	T T T
0.3633780000	2.8462670000	3.6100280000	T T T
5.8722910000	6.8001060000	3.7794040000	T T T
5.8680950000	2.7120820000	3.7862430000	T T T
8.4706690000	6.7884290000	3.7922890000	T T T
3.1419770000	6.6594850000	3.7961850000	T T T
0.4256100000	6.6600290000	3.7964580000	T T T
3.1401060000	2.8572860000	3.7998430000	T T T
8.6018880000	4.6159870000	5.5081690000	T T T
0.3329260000	4.6176060000	5.5980560000	T T T
0.3148050000	1.0571310000	5.6035060000	T T T

5.7845580000	4.7512000000	5.6050310000	T T T
8.5307690000	1.0783380000	5.6451740000	T T T
3.2273400000	0.9620060000	5.7120320000	T T T
3.2166010000	4.7539640000	5.7221990000	T T T
5.8575480000	0.9447460000	5.7370010000	T T T

A3. Sample VASP Codes for CI-NEB Calculations

A3.1. INCAR File

```
!FOR CNEB
IMAGES = 8
SPRING = -5
ICHAIN = 0
LCLIMB = .TRUE.
LTANGENTOLD = .FALSE.
LDNEB = .FALSE.
!EDIFFG = -0.015
IBRION = 1;
POTIM = 0.2;
!NFREE = 20
NSW = 200
LDIPOL = .TRUE.
ISMEAR = 0; SIGMA = 0.1;
LREAL = Auto
ENCUT = 500
IDIPOL = 3
```

A3.2. KPOINTS File

K-Points

0

Monkhorst Pack

4 4 1

0 0 0

A4. Sample VASP Codes For Transition State Calculations

A4.1. INCAR File

EDIFFG = -0.015

IBRION = 1

!POTIM = 0.2;

!NFREE = 20

ISMEAR = 0; SIGMA = 0.01;

LREAL = Auto

ENCUT = 500

IDIPOL = 3

LDIPOL = .TRUE.

NSW = 300

ALGO=FAST

A4.2. KPOINTS File

K-Points

0

Monkhorst Pack

4 4 1

0 0 0

APPENDIX B

CATALYST PREPARATION

B1. Impregnation Method

B1.1. Preparation of Ceria-Zirconia Mixed Oxide (CZO)

For synthesis of 100 g of $Ce_{0.8}Zr_{0.2}O_2$ mixed oxide powder:

- 214.00 g of $CeN_3O_9 \cdot 6H_2O$ and 41.80 g of $N_2O_7Zr \cdot aq$ are dissolved in and stirred for 30 min in 1 lt of deionized water.
- 333 ml of H_2O_2 is added to the mixture and stirred for 1 h.
- Mixture is dropwisely added to 550 ml of NH_4OH solution and kept for 12 h.
- Product is washed and filtered with excess $CH_3CHOHCH_3$ then refluxed in 250 ml $CH_3CHOHCH_3$ for 6 h.
- Refluxed product is dried at $150^\circ C$ for 12 h.
- Dried powder sample is finely grounded and calcined in the muffle furnace under dry air at $600^\circ C$ for 5 h.

B1.2. Impregnation of Metals

For the synthesis of 10 g of IMP1 catalyst:

- 2.33 ml of $PdCl_2$ solution is solved in 7.9 ml water

- The mixture is rotated in rotary vacuum evaporator for 15 minutes without applying any heating or vacuum.
- Metal solution and 10 g of $\text{Ce}_{0.8}\text{Zr}_{0.2}\text{O}_2$ are mixed together and rotated in the water bath kept at 80 °C under vacuum at ~450 mbar
- When all the liquid is evaporated, the product is dried at 150 °C for 12 h.
- The powder sample is grounded and calcined in the muffle furnace under dry air at 500 °C. for 3 h.

For the synthesis of 10 g of IMP3 catalyst:

- 2.0 ml of PdCl_2 solution is solved in 3.95 ml water and rotated in rotary vacuum evaporator for 15 minutes without applying any heating or vacuum.
- Metal solution and 5 g of $\text{Ce}_{0.8}\text{Zr}_{0.2}\text{O}_2$ are mixed together and rotated in the water bath kept at 80 °C under vacuum at ~450 mbar .
- 0.91 ml of $\text{Mn}(\text{NO}_3)_2$ solution is solved in 3.95 ml water and rotated in rotary vacuum evaporator for 15 minutes without applying any heating or vacuum.
- Metal solution and 5 g of $\text{Ce}_{0.8}\text{Zr}_{0.2}\text{O}_2$ are mixed together and rotated in the water bath kept at 80 °C under vacuum at ~450 mbar .
- When all the liquid is evaporated, products are dried at 150 °C for 12 h.
- Powder samples together are grounded together and calcined in the muffle furnace under dry air at 500 °C for 3 h.

B2. Solution Combustion Method

For the synthesis of 15 g of $\text{Ce}_{0.79}\text{Zr}_{0.2}\text{Pd}_{0.01}\text{O}_2$ catalyst:

- 31.76 g of $\text{CeN}_3\text{O}_9 \cdot 6\text{H}_2\text{O}$, 4.28 g of $\text{N}_2\text{O}_7\text{Zr} \cdot \text{aq}$ and 3.09 ml of PdCl_2 solution are dissolved in 50 ml deionized water
- 12.09 g of $\text{CH}_4\text{N}_2\text{O}$ is added to the mixture as the fuel and the mixture vigorous stirring is applied
- The mixture is introduced to the muffle furnace maintained at 450°C

- Combustion occurs with a burning flame and foamy product is formed within 5 min.

For the synthesis of 15 g of $\text{Ce}_{0.80}\text{Zr}_{0.1}\text{Mn}_{0.1}\text{O}_2$ catalyst:

- 32.83 g of $\text{CeN}_3\text{O}_9 \cdot 6\text{H}_2\text{O}$, 2.18 g of $\text{N}_2\text{O}_7\text{Zr} \cdot \text{aq}$ and 2.37 g of $\text{Mn}(\text{NO}_3)_2 \cdot 4\text{H}_2\text{O}$ are dissolved in 50 ml deionized water
- 12.30 g of $\text{CH}_4\text{N}_2\text{O}$ is added to the mixture as the fuel and the mixture vigorous stirring is applied
- The mixture is introduced to the muffle furnace maintained at 450°C
- Combustion occurs with a burning flame and foamy product is formed within 5 min.

For the synthesis of 20 g of $\text{Ce}_{0.79}\text{Zr}_{0.1}\text{Mn}_{0.1}\text{Pd}_{0.01}\text{O}_2$ catalyst:

- 43.32 g of $\text{CeN}_3\text{O}_9 \cdot 6\text{H}_2\text{O}$, 2.92 g of $\text{N}_2\text{O}_7\text{Zr} \cdot \text{aq}$, 3.17 g of $\text{Mn}(\text{NO}_3)_2 \cdot 4\text{H}_2\text{O}$ and 4.22 ml of PdCl_2 solution are dissolved in 50 ml deionized water
- 16.23 g of $\text{CH}_4\text{N}_2\text{O}$ is added to the mixture as the fuel and the mixture vigorous stirring is applied
- The mixture is introduced to the muffle furnace maintained at 450°C
- Combustion occurs with a burning flame and foamy product is formed within 5 min.

B3. Preparation of the Wascoating Slurry

Preparation of washcoating slurry with 10 g of catalyst:

- 10 g of catalyst and 23 g of $\gamma\text{-Al}_2\text{O}_3$ are mixed in 48.91 ml of deionized water and ballmilled with 3 mm diameter alumina chips at 275 rpm for 24 hr in HDPE mortar.
- Product is dried at 150°C for 12 h, grounded and calcined at 550°C for 1 h.
- 2.3 g of pseudoboehmite is added and the mixture is solved in 52.36 ml deionized water and ballmilled for 30 min at 275 rpm.

- 2.28 ml of nitric acid is added and slurry is ballmilled at same speed for 3 h.

B4. Preparation of Pseudoboehmite

To synthesize 100 g of pseudoboehmite:

- 103.1 g of $\text{Al}(\text{OC}_4\text{H}_9)_3$ hydrolyzed with 730 ml double distilled water.
- 9 ml HCL is added to the beaker.
- The mixture is stirred vigorously for 1 h while keeping at 80 °C.
- Product as gel is dried at 150 °C for 48 h .
- The powder sample is grounded and calcined in the muffle furnace for at 300 °C for 5 h with a heating rate of 5 °C/min.

APPENDIX C

CALCULATIONS FOR CATALYTIC ACTIVITY TEST

C.1. Calculation of Total Gas Flow Rate

For selected gas hourly space velocity (GHSV) of 50000 h⁻¹, total flow rate of the simulated exhaust gas mixture is calculated using equation C.1. (Fogler, 2006)

$$GSHV = \frac{v_0}{V_{eff}} \quad (C.1)$$

Effective volume, V_{eff} is calculated for a catalytic monolith with dimensions of 1.3 cm height, 2.2 cm width and having an open frontal area of 0.69% (Kaspar, et al., 2003)

$$V_{eff} = \left(\pi * \left(\frac{(0.022m)^2}{4} \right) * (0.013m) \right) * (0.69) = 3.41 * 10^{-6} m^3$$

$$50000 h^{-1} = \frac{v_0(L/h)}{(3.41 * 10^{-6}m^3) * (1L / 10^{-3}m^3)}$$

$$v_0 = 170.5 L/h$$

$$v_0 = (170.5 L/h) * (1000 mL/L) * (1 h/60 min) = 2841.5 ml/min$$

C.2. Simulated Exhaust Gas Composition

Gas mixture composition in order to obtain the simulated exhaust gas is shown in Table 44. Composition of the oxygen gas is calculated to have stoichiometric number 1.

Table 44 Simulated exhaust gas mixture composition

Species	Gas Mixture	
	Composition (ppm)	Composition (%)
H ₂	2300	0.23
CO	10000	1.00
C ₃ H ₆	375	0.0375
C ₃ H ₈	125	0.0125
CO ₂	100000	10.00
NO	1500	0.15
SO ₂	20	0.002
O ₂	7700	0.77
N ₂	Balance	Balance

Composition of oxygen for stoichiometric number *S* of 1.0 is calculated as 0.77 % by using the definition below:

$$S = \frac{2[O_2] + [NO]}{[H_2] + [CO] + 9[C_3H_6] + 10[C_3H_8]}$$

$$[O_2] = \frac{1.0 * [0.23] + [1.00] + 9[0.0375] + 10[0.0125] - [0.15]}{2}$$

$$[O_2] = 0.77 \%$$

Five cylinders are used in order to obtain desired flow rate for each species. Compositions of the gas cylinders are shown in Table 45.

Table 45 Compositions of gas cylinders

Cylinder	Species	Cylinder Composition	Cylinder Composition (%)
1	H ₂	20400	2.04
	CO	88700	8.87
	C ₃ H ₆	3300	0.33
	C ₃ H ₈	1100	0.11
	CO ₂	886500	88.65
2	NO	500000	50.00
	N ₂	500000	50.00
3	SO ₂	100	0.01
	N ₂	999900	99.99
4	O ₂	995000	99.50
5	N ₂	999980	99.998

Flow rate of each gas cylinder is calculated using the cylinder compositions, as shown below :

$$\text{Flow rate} = \frac{v_0(\text{ml/min}) * (\text{Gas Mixture Composition (\%)})}{(\text{Gas Cylinder Composition (\%)})}$$

For cylinder 1 (using CO values) :

$$\text{HC Mixture Flow rate} = \frac{2841.5(\text{ml/min}) * 1.00}{0.087} = 320.52 \text{ ml/min}$$

For cylinder 2:

$$\text{NO Mixture Flow rate} = \frac{2841.5(\text{ml/min}) * 0.00150}{0.0050} = 8.52 \text{ ml/min}$$

For cylinder 3 :

$$\text{SO}_2 \text{ Mixture Flow rate} = \frac{2841.5(\text{ml/min}) * 0.00002}{0.0001} = 8.52 \text{ ml/min}$$

For cylinder 4 (for S = 1.0):

$$\text{O}_2 \text{ Mixture Flow rate} = \frac{2841.5(\text{ml/min}) * 0.0077}{1} = 21.92 \text{ ml/min}$$

To provide oxygen gas oscillation around stoichiometric numbers of 0.77 and 1.21, necessary O₂ flow rates are calculated as 16.67 ml/min and 27.17 ml/min respectively. Consequently, with an additional oxygen flow of 10.5 ml/min exhaust gas can be oscillated between reducing and oxidizing conditions.

To calculate N₂ flow rate, flow rates of the four cylinders are added to one tenth of total flow rate which is water vapor, and subtracted from 2841.5 ml/min.

Flow rates and compositions of each gas cylinder under three conditions are shown in Table 46 and Table 47 below:

Table 46 Gas cylinder flow rates for reducing, stoichiometric and oxidizing conditions

Cylinder	Flow Rate (ml/min)		
	Reducing	Stoichiometric	Oxidizing
1	320.52	320.52	320.52
2	8.52	8.52	8.52
3	568.30	568.30	568.30
4	16.67	21.92	27.17
5	1638.09	1638.09	1638.09
Total	2836.25	2841.5	2846.75

Table 47 Compositions of simulated exhaust gas mixture for reducing, stoichiometric and oxidizing conditions

Cylinder	Gas Mixture Compositions (%)		
	Reducing	Stoichiometric	Oxidizing
H ₂	0.231	0.230	0.230
CO	1.002	1.001	0.999
C ₃ H ₆	0.037	0.037	0.037
C ₃ H ₈	0.012	0.012	0.012
CO ₂	10.018	10.000	9.981
NO	0.150	0.150	0.150
SO ₂	0.002	0.002	0.002
O ₂	0.586	0.767	0.949
N ₂	57.754	57.648	57.541

C.3. Water Content of Simulated Exhaust Gas

Antoine Equation is employed to compute the saturation temperature of the water vapor for 1638.2 ml of N₂ gas as carrier (Equation B.2.) (Perry & Green, 1997)

$$\log P^{sat} = A - \frac{B}{C+T} \quad (C.2)$$

In the equation, P^{sat} is in torr and T in °C. It is applicable for water in the temperature range of 1-100°C. with $A = 8.07131$, $B = 1730.63$, $C = 233.426$

To calculate P^{sat}, atmospheric pressure is taken as 1 atm. Partial pressure of the vapor is taken as the ratio of required water vapor flow rate to flow rate of water vapor and N₂ gas together. Consequently, P^{sat} is calculated as follows:

$$\frac{H_2O}{N_2 + H_2O} = \frac{284.15}{2841.5 + 1638.1} = 0.1478$$

$$P^{sat} = (1 \text{ atm}) * 0.1478 = 0.1478 \text{ atm}$$

$$P^{sat} = (0.1478 \text{ atm}) * \frac{760 \text{ torr}}{1 \text{ atm}} = 112.344 \text{ torr}$$

$$T = \frac{B}{A - \log P^{sat}} - C$$

$$T = \frac{1730.63}{8.07131 - \log(112.344)} - 233.426$$

$$T = 54 \text{ }^\circ\text{C}$$

Therefore, it is found that the heating room where dry nitrogen gas will be humidified should be kept at a temperature of 54°C.

C.4. Analysis of MAS-SOFT data

For the gases other than CO, concentration data from MS is received as signal. To obtain conversion values from the data, firstly signal is converted to concentration value by using calibration equation of the gaseous species and then conversion is computed by equation C.3. below (Fogler, 2006)

$$X = \frac{C_{A0} - C_A}{C_{A0}} * 100\% \quad (C.3)$$

As an example, an initial MS data of 4.91E-08 and an instant data of 4.5 E-09 for H₂ are taken. Both signals are converted to concentration values with corresponding calibration equation.

$$H_2 \text{ Calibration Equation : } y = (6E + 10)x - 251.51$$

$$C_{A0} = (6E + 10) * (4.91E - 08) - 251.51 = 2694 \text{ ppm}$$

$$C_A = (6E + 10) * (4.5E - 09) - 251.51 = 19 \text{ ppm}$$

$$X = \frac{C_{A0} - C_A}{C_{A0}} * 100\% = \frac{2694 - 19}{2694} * 100\% = 93.15$$

Conversion corresponding to the data is calculated as 93.15%

For CO conversion calculations, value read from the analyzer in ppm unit is used directly. Taking the initial concentration as 9999 ppm, which is the maximum value that CO analyzer can read, for an instant concentration of 3500 ppm conversion is calculated as

$$X = \frac{C_{A0} - C_A}{C_{A0}} * 100\% = \frac{9999 - 3500}{9999} * 100\% = 65.10$$

Conversion corresponding to the data is calculated as 65.10%

APPENDIX D

CALIBRATIONS FOR MASS SPECTROMETER

Mass Spectrometer (MS) calibration data and graphs for H₂, C₃H₆, C₃H₈, NO, SO₂ and O₂ are given in Table and Figure

Table 48 MS calibration data for H₂

H₂	
Concentration (ppm)	Signal
0	3.13E-09
553	1.50E-08
1106	2.49E-08
1658	3.42E-08
2211	4.33E-08
2764	5.24E-08

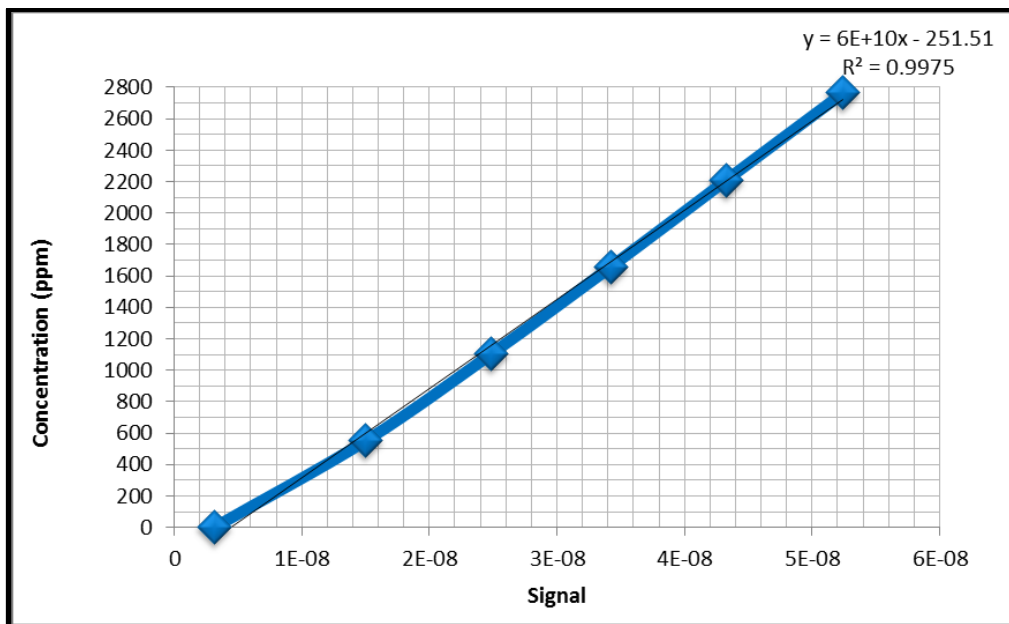


Figure 49 MS calibration plot for H₂

Table 49 MS calibration data for C₃H₆

C ₃ H ₆	
Concentration (ppm)	Signal
0	1.72E-11
89	4.08E-09
179	7.47E-09
268	1.07E-08
358	1.38E-08
447	1.73E-08

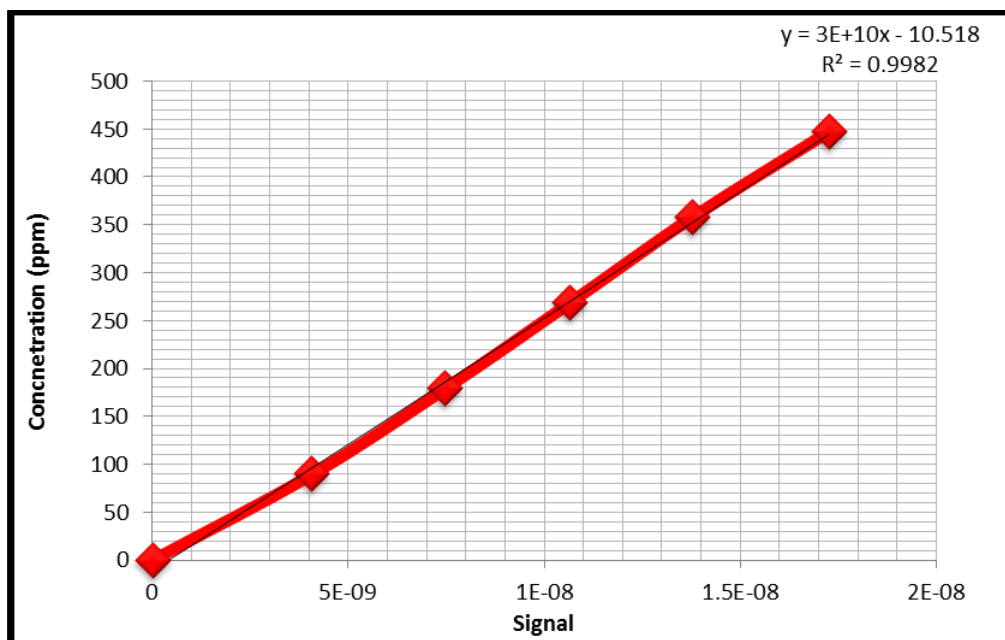


Figure 50 MS calibration plot for C₃H₆

Table 50 MS calibration data for C₃H₈

C ₃ H ₈	
Concentration (ppm)	Signal
0	4.10E-10
30	3.30E-09
60	5.69E-09
89	8.05E-09
119	1.05E-08
149	1.40E-08

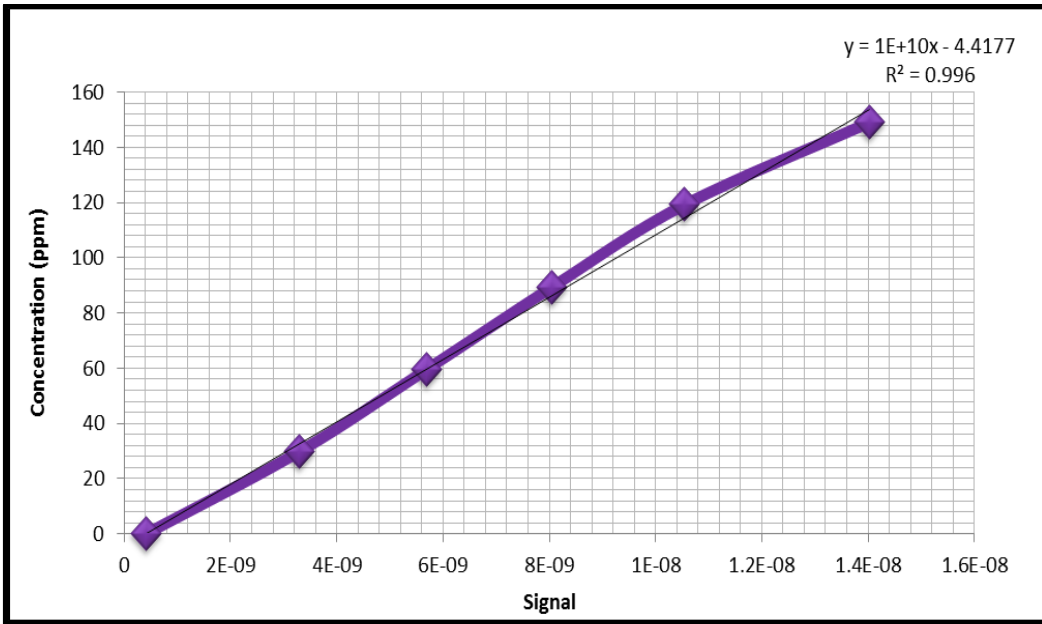


Figure 51 MS calibration plot for C₃H₈

Table 51 MS calibration data for NO

NO	
Concentration (ppm)	Signal
0	6.05E-08
360	1.34E-08
720	2.41E-08
1080	3.26E-08
1440	3.90E-08
1800	4.91E-08

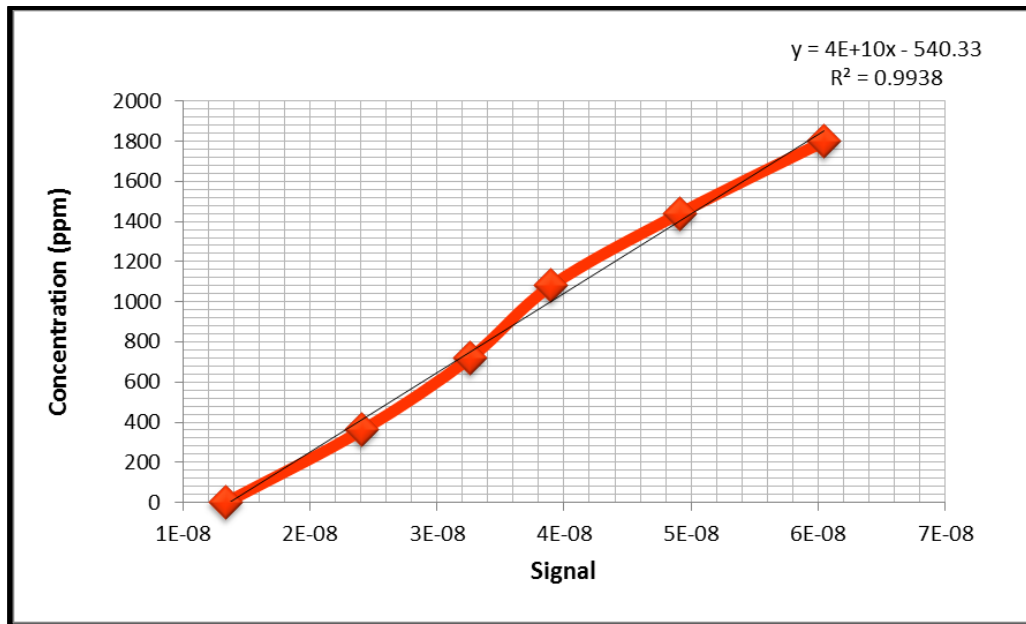


Figure 52 MS calibration plot for NO

Table 52 MS calibration data for SO₂

SO ₂	
Concentration (ppm)	Signal
0	1.32E-10
5	1.90E-10
10	2.50E-10
14	3.50E-10
19	4.34E-10
24	5.17E-10

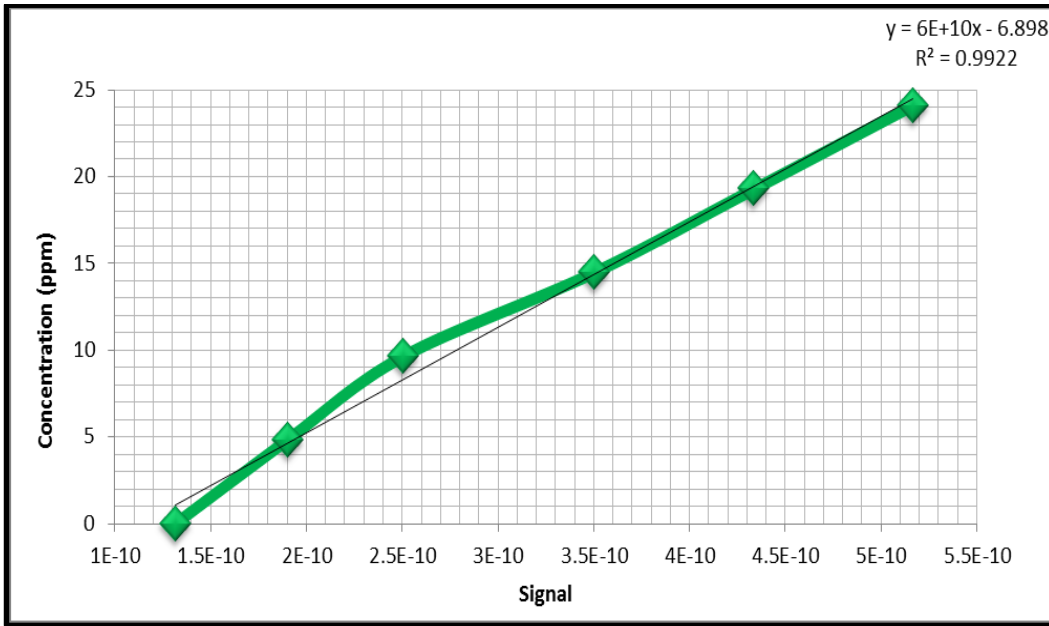


Figure 53 MS calibration plot for SO₂

Table 53 MS calibration data for O₂

O₂	
Concentration (ppm)	Signal
0	1.53E-08
1842	4.93E-08
3684	8.47E-08
5526	1.28E-07
7369	1.72E-07
9211	2.23E-07

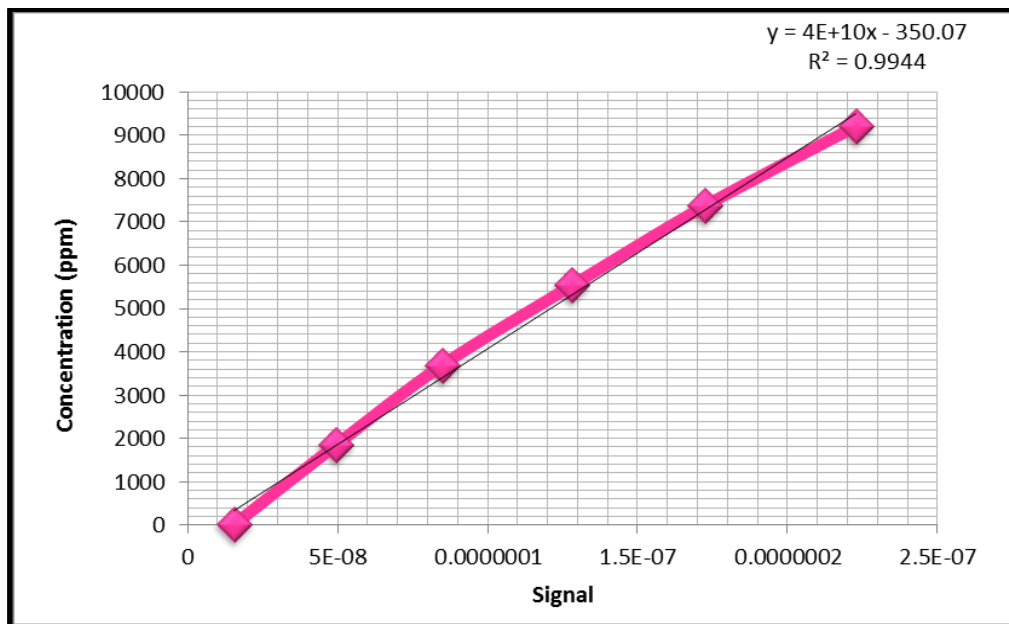


Figure 54 MS calibration plot for O₂

APPENDIX E

CONVERSION VERSUS TEMPERATURE PLOTS OF ACTIVITY TESTS

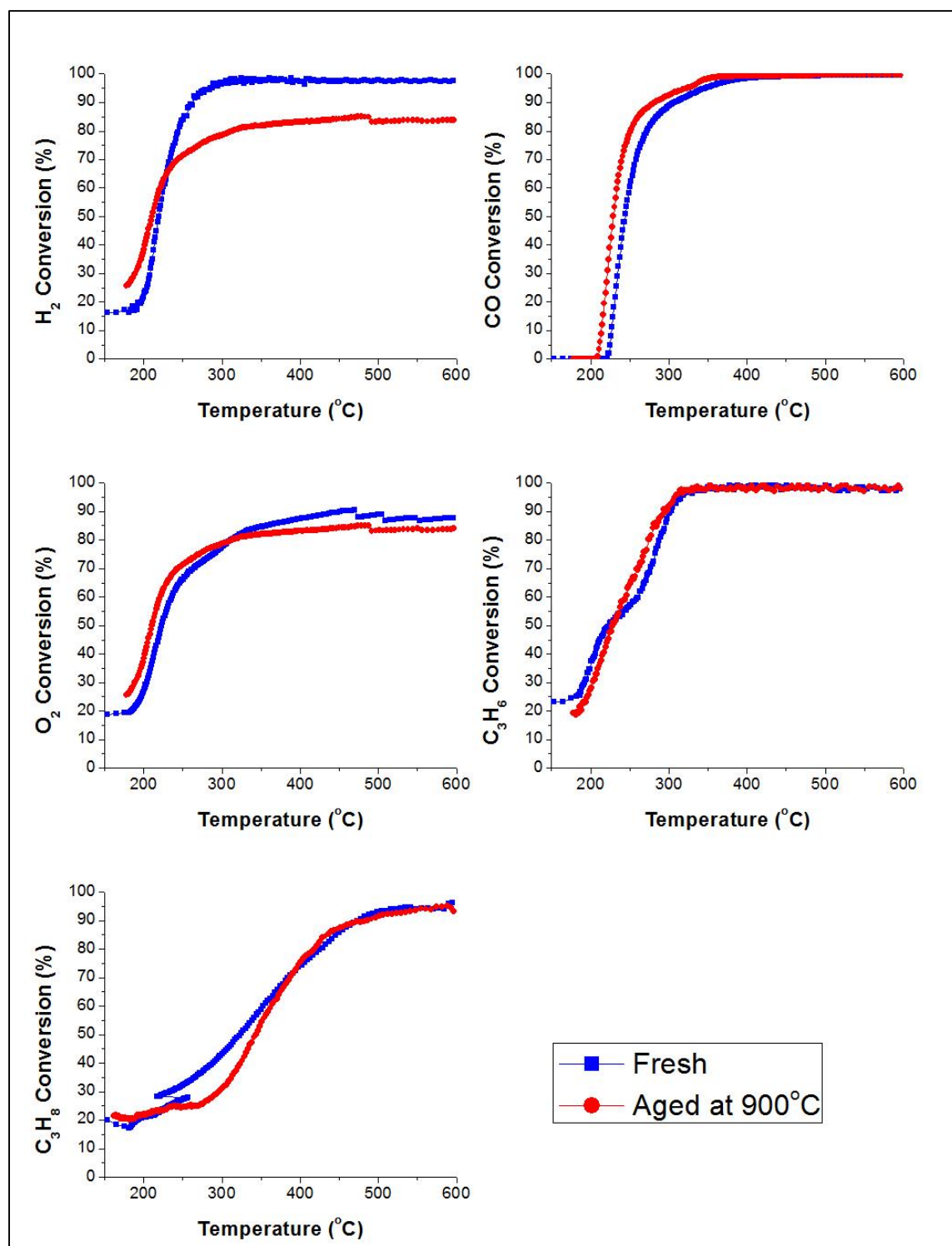


Figure 55 Conversion versus temperature curves of IMP1-M1 in thermal aging (no SO₂)

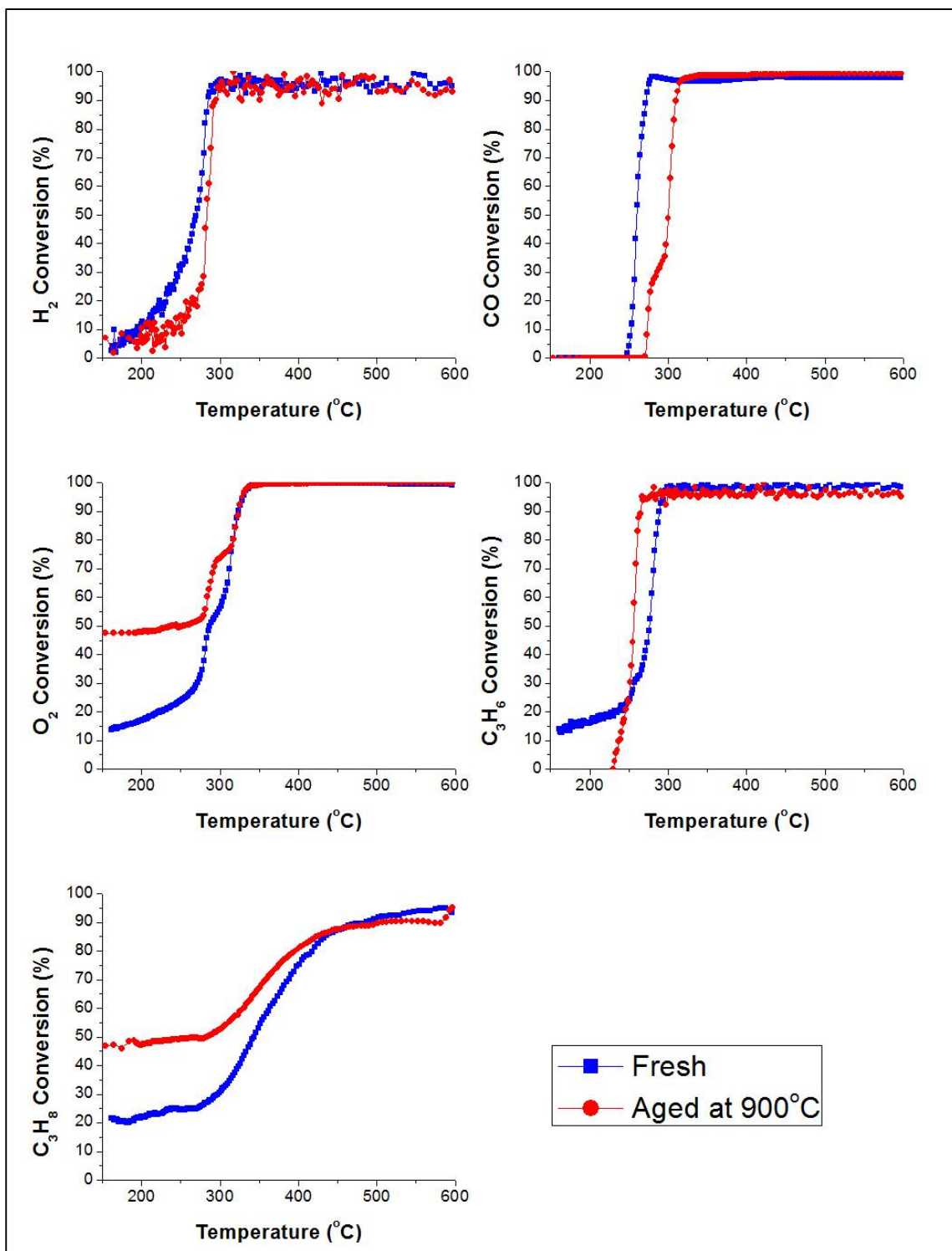


Figure 56 Conversion versus temperature curves of IMP1-M2 in thermal aging (with SO₂)

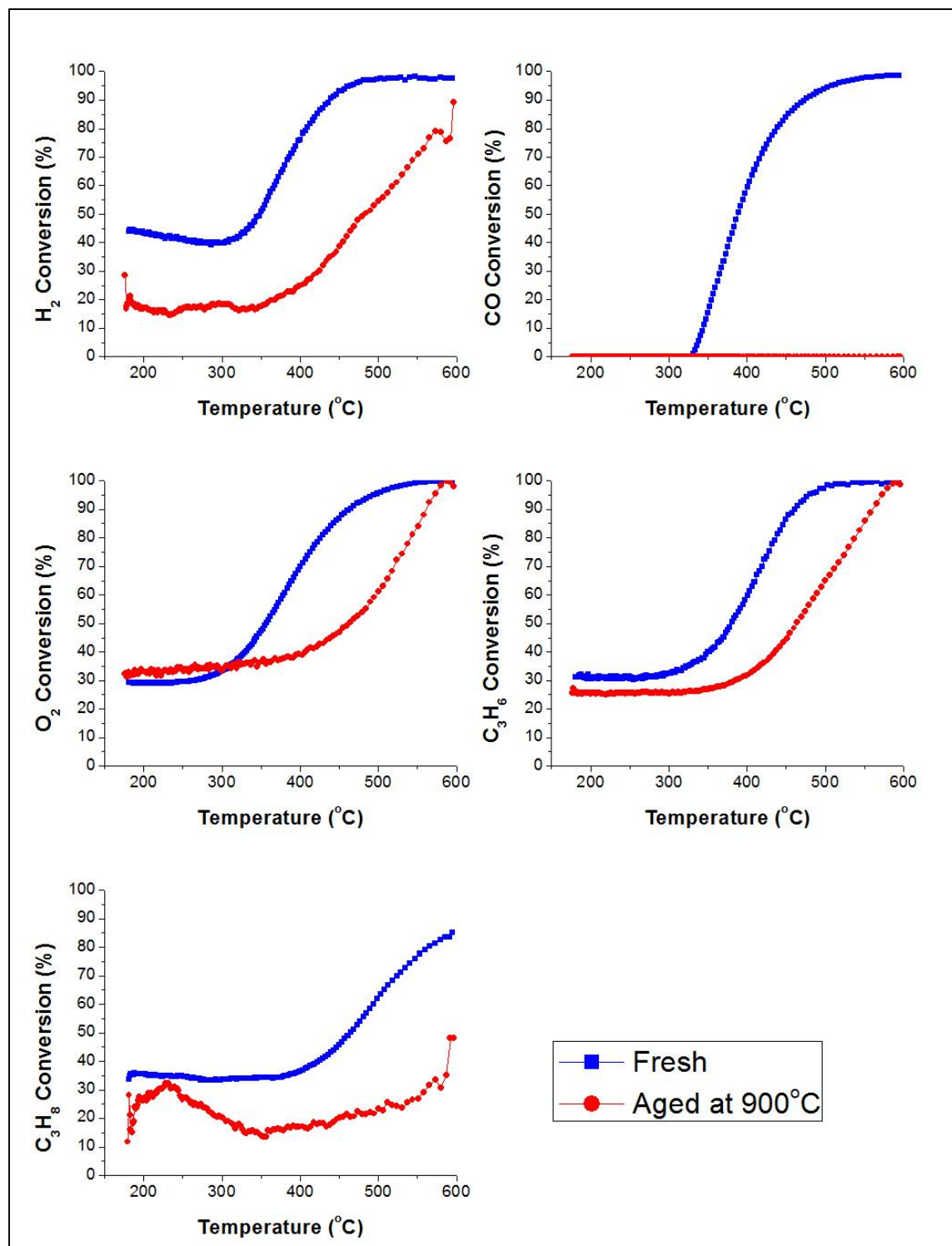


Figure 57 Conversion versus temperature curves of IMP2-M1 in thermal aging (no SO₂)

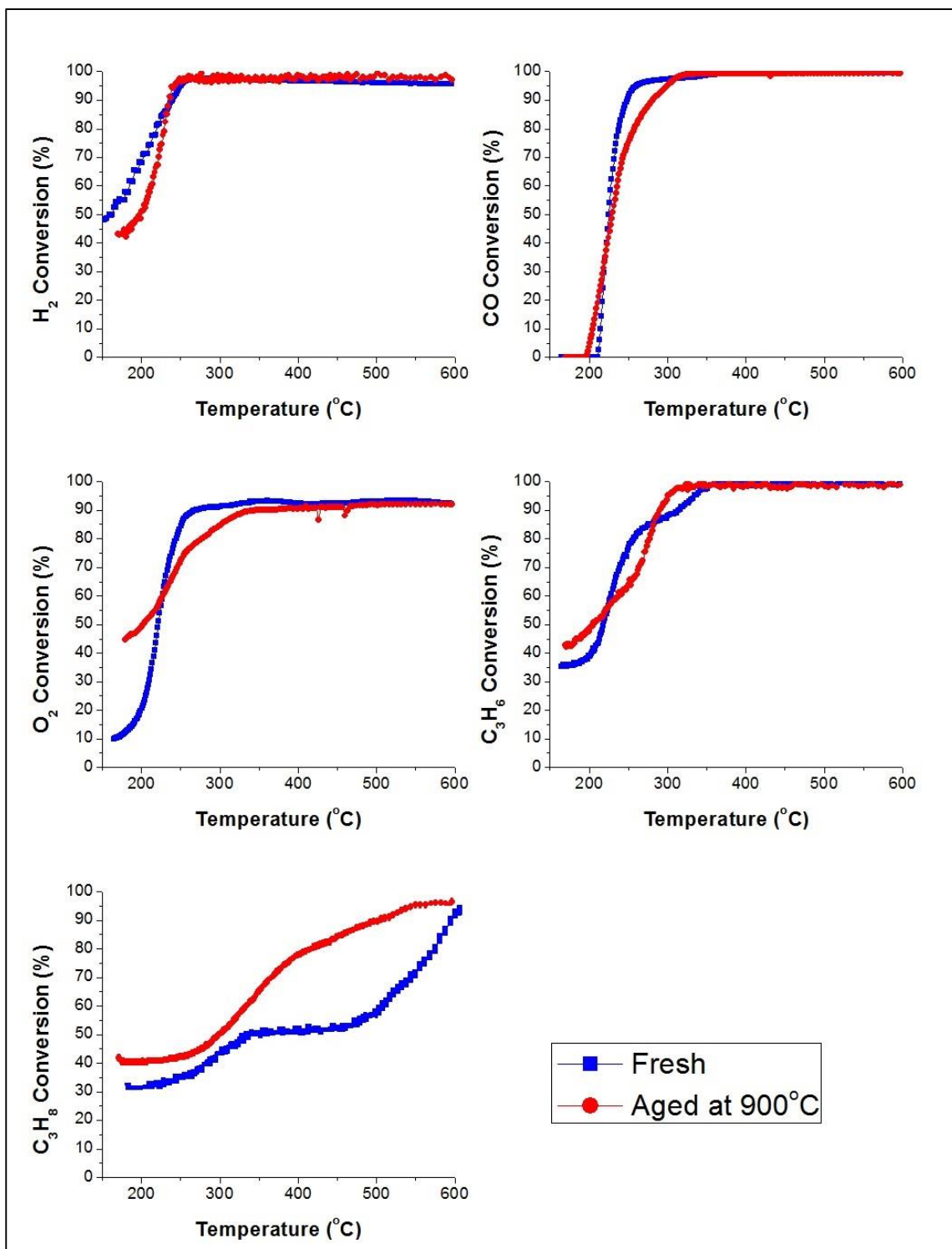


Figure 58 Conversion versus temperature curves of IMP3-M1 in thermal aging (no SO₂)

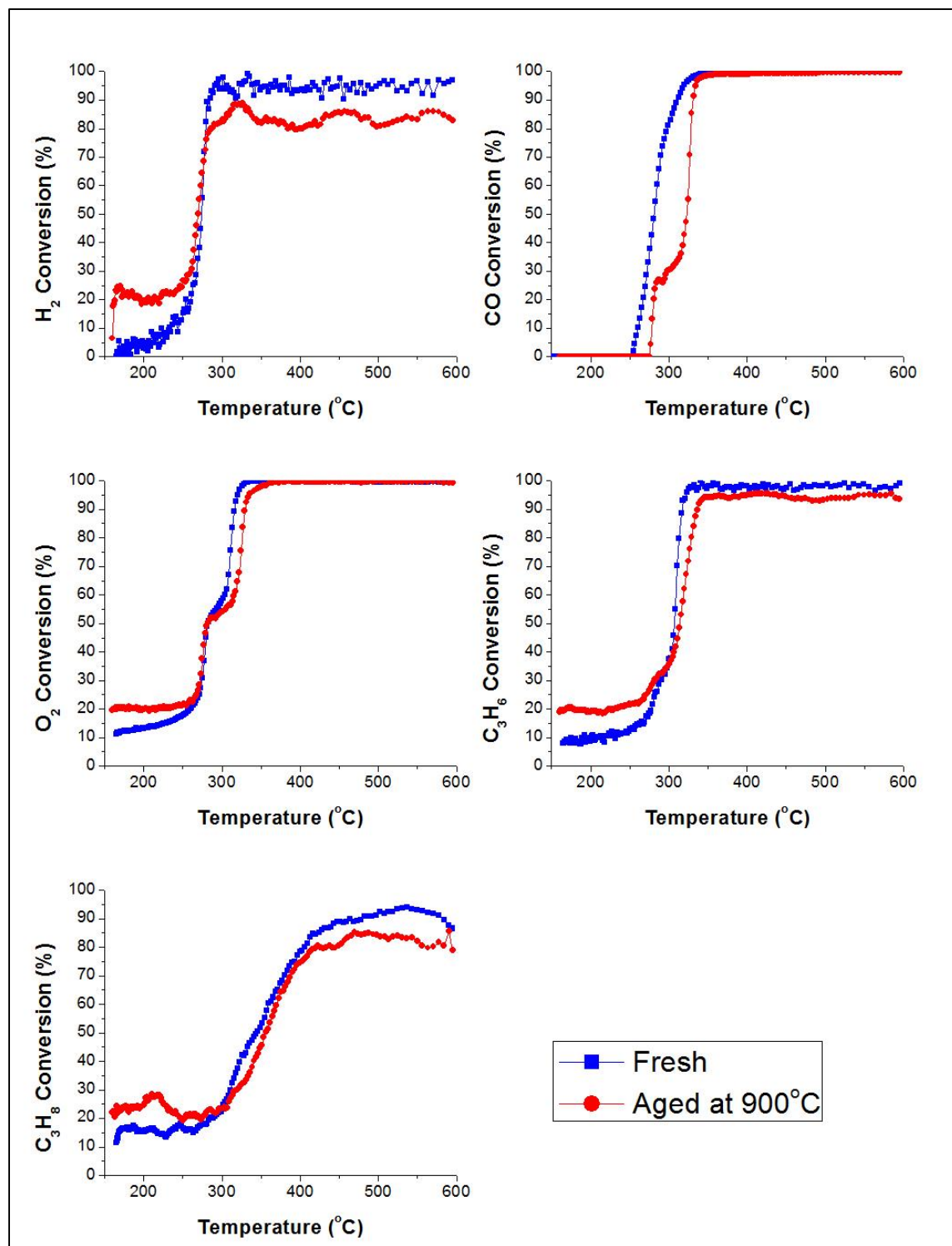


Figure 59 Conversion versus temperature curves of IMP3-M2 in thermal aging (with SO₂)

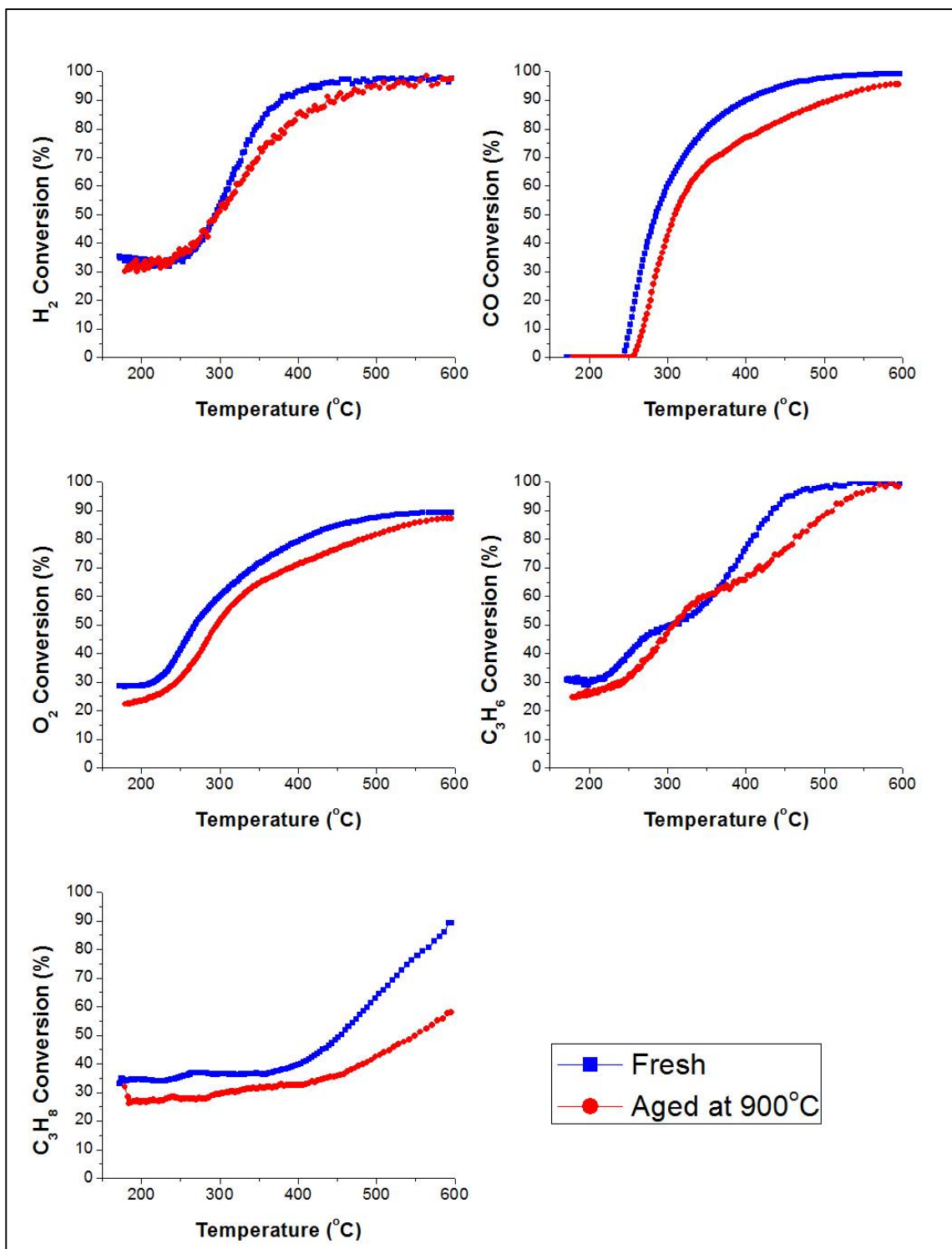


Figure 60 Conversion versus temperature curves of IMP4-M1 in thermal aging (no SO₂)

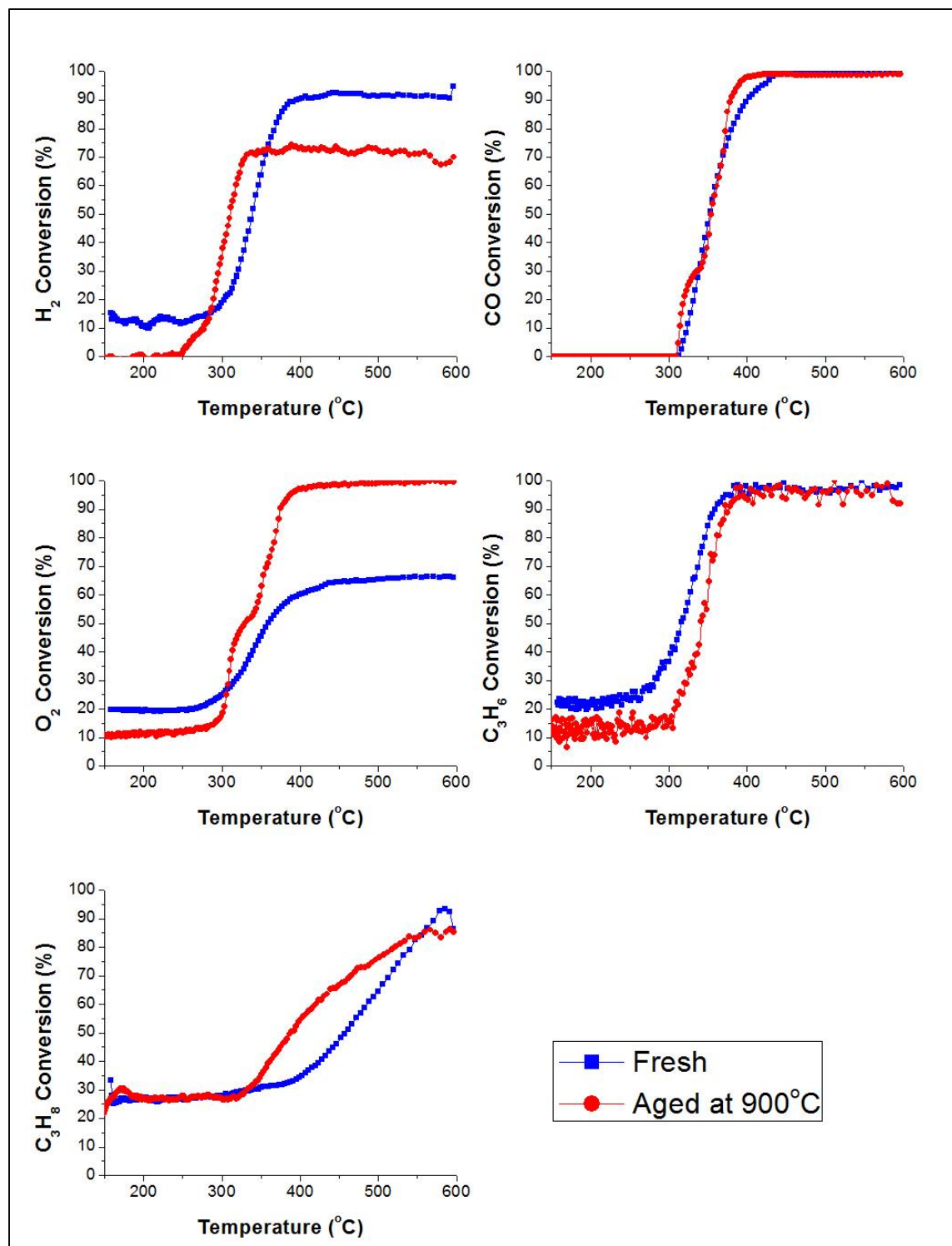


Figure 61 Conversion versus temperature curves of IMP4-M2 in thermal aging (with SO₂)

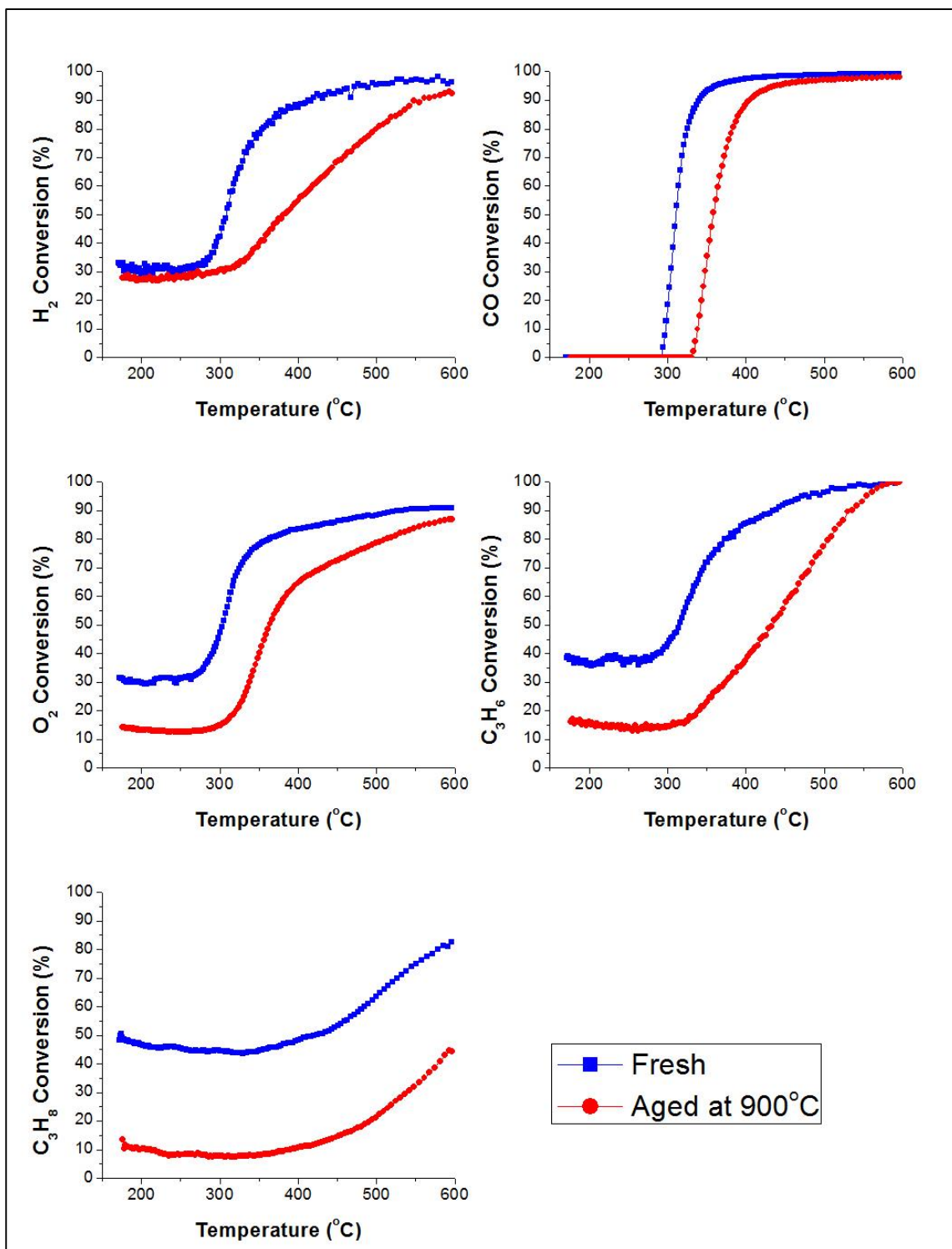


Figure 62 Conversion versus temperature curves of IMP5-M1 in thermal aging (no SO₂)

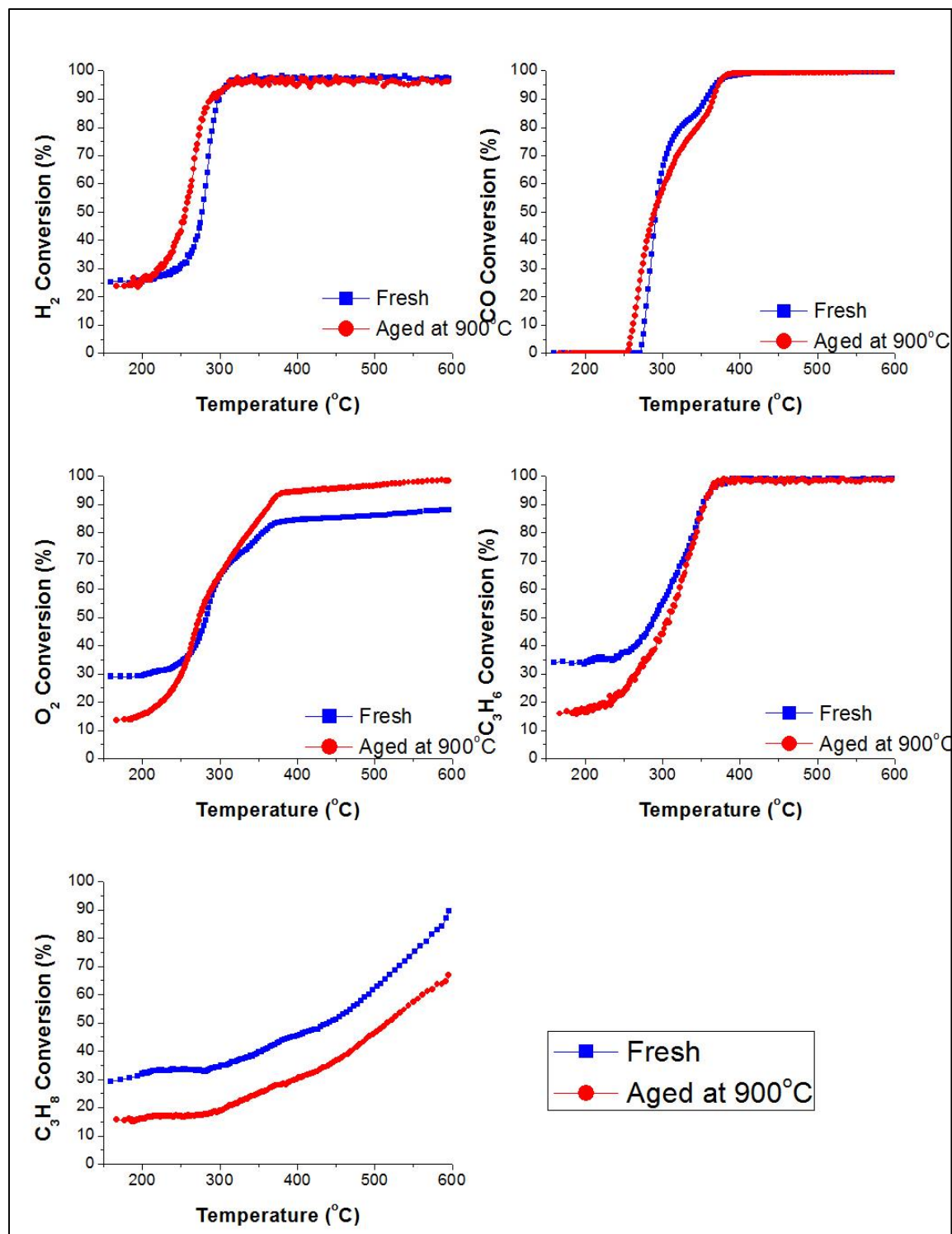


Figure 63 Conversion versus temperature curves of SC1-M1 in thermal aging (no SO₂)

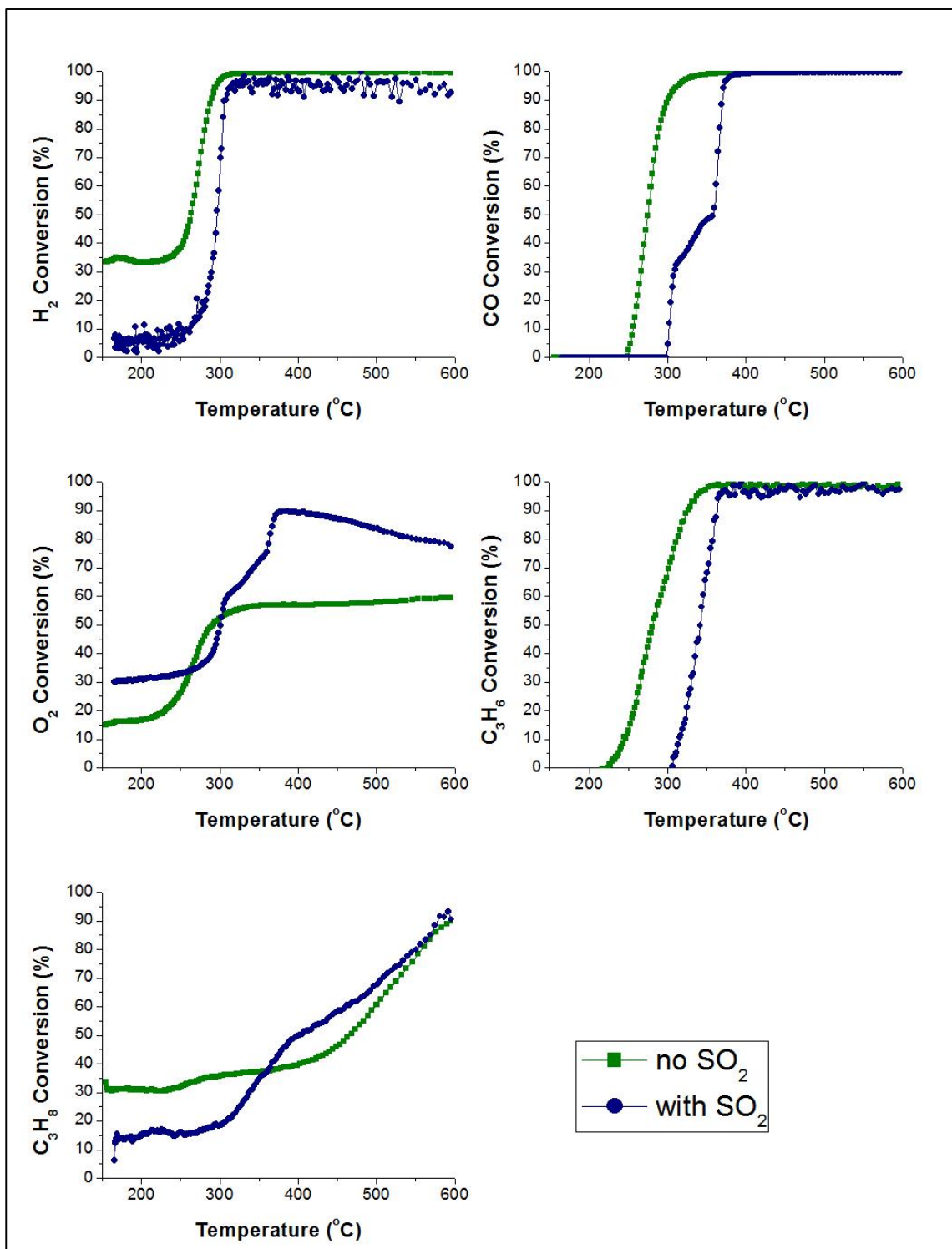


Figure 64 Conversion versus temperature curves of SC1-M2 in SO₂ exposure

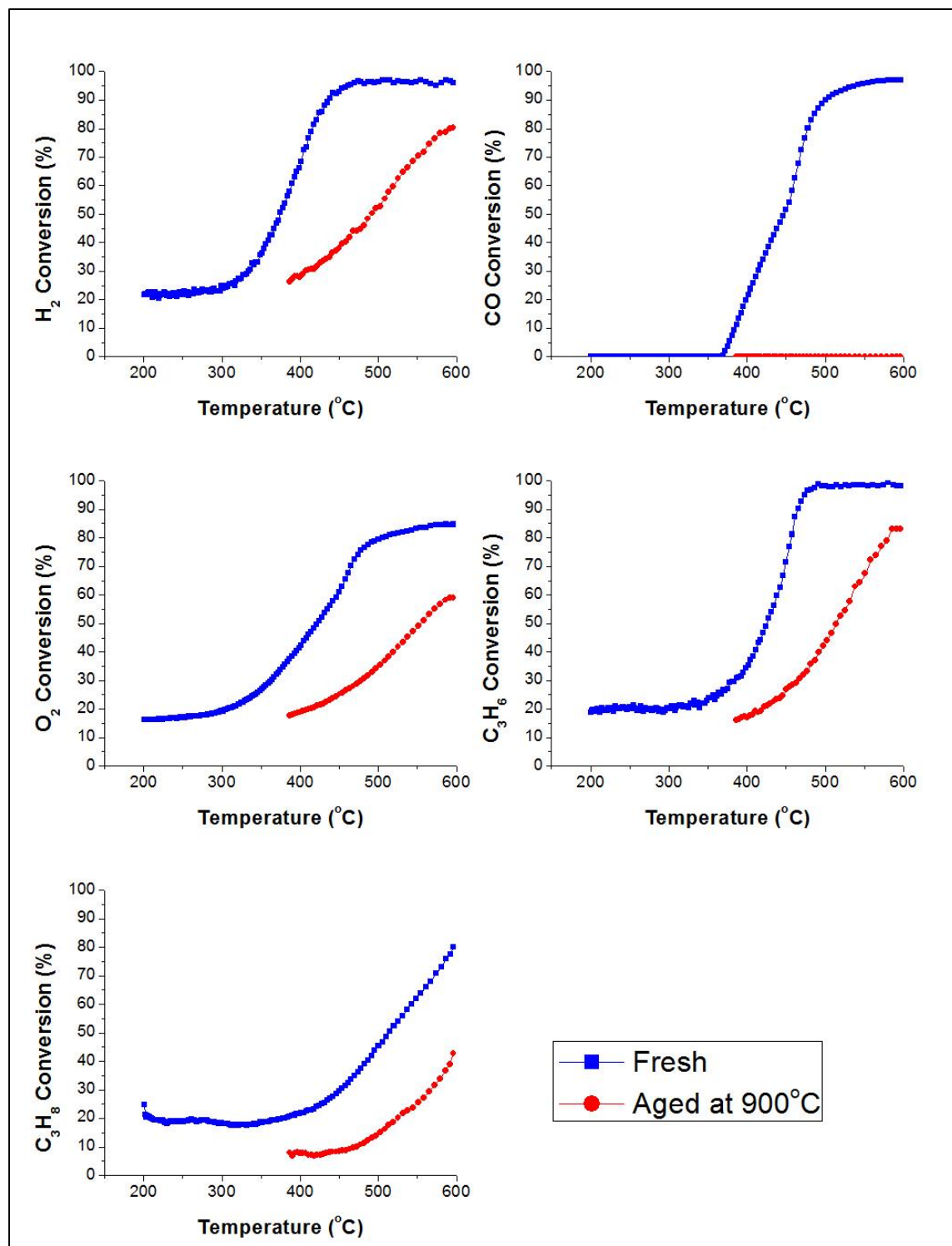


Figure 65 Conversion versus temperature curves of SC2-M1 in thermal aging (no SO₂)

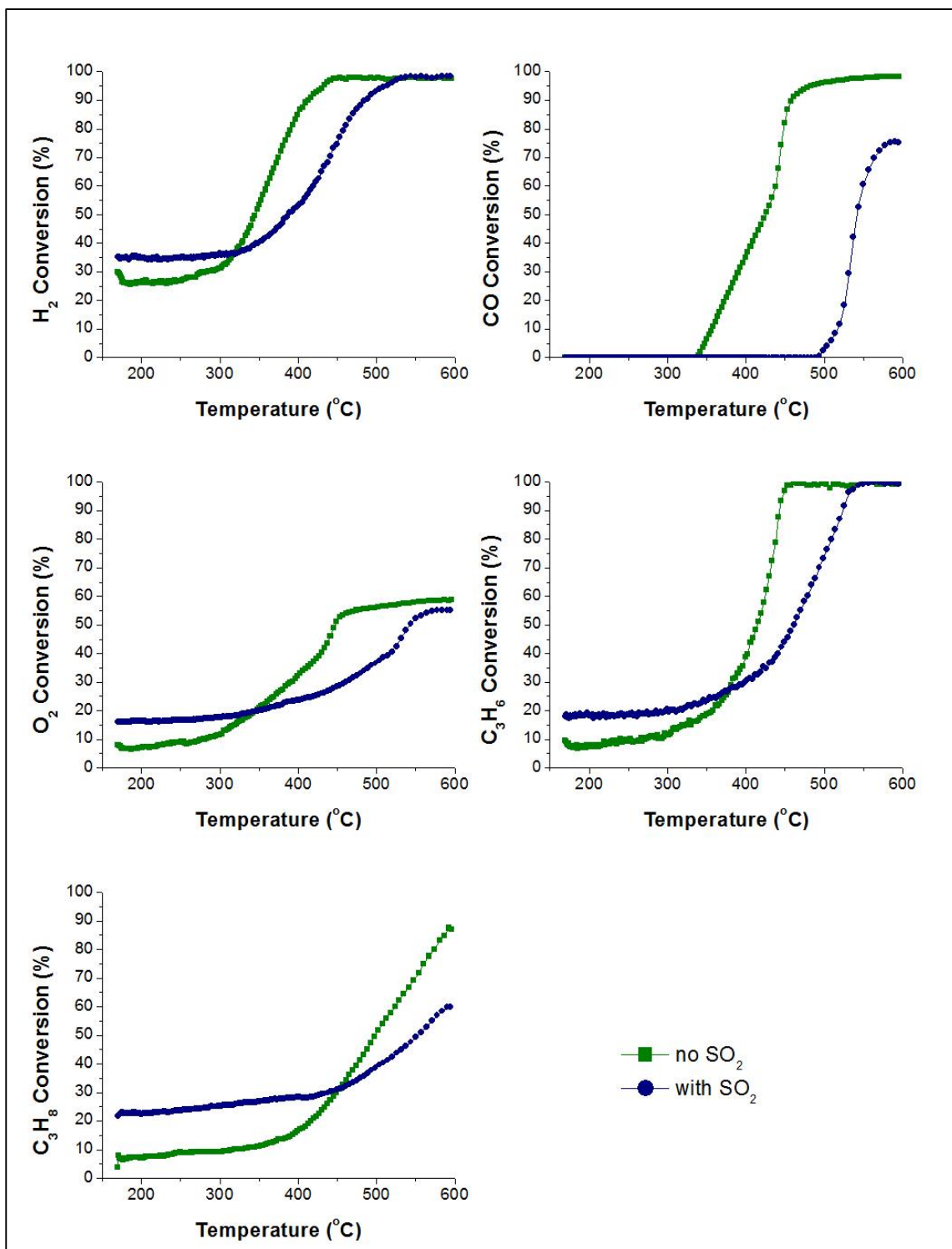


Figure 66 Conversion versus temperature curves of SC2-M2 in SO₂ exposure

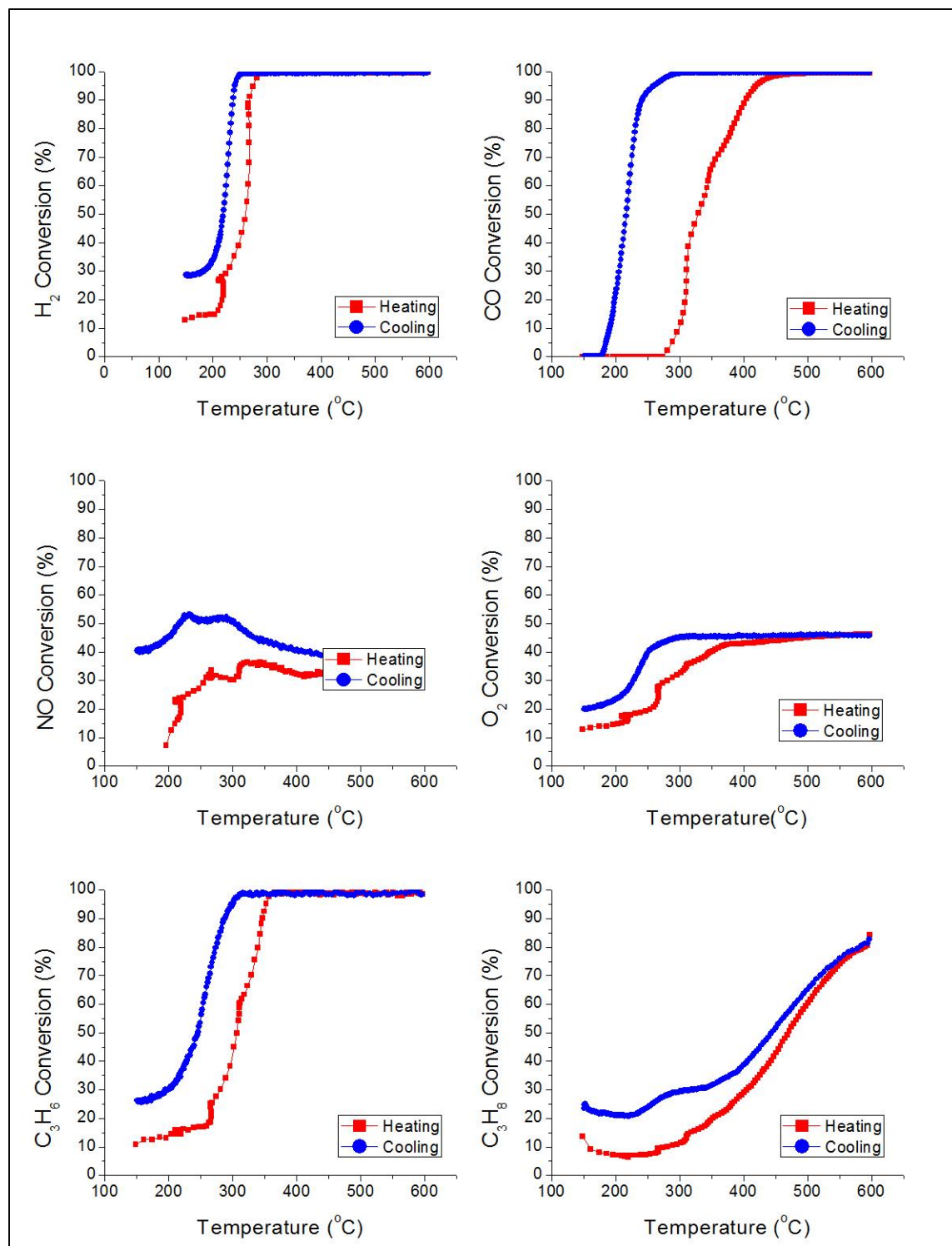


Figure 67 Conversion versus temperature curves of SC3-M1 in thermal aging (no SO₂)

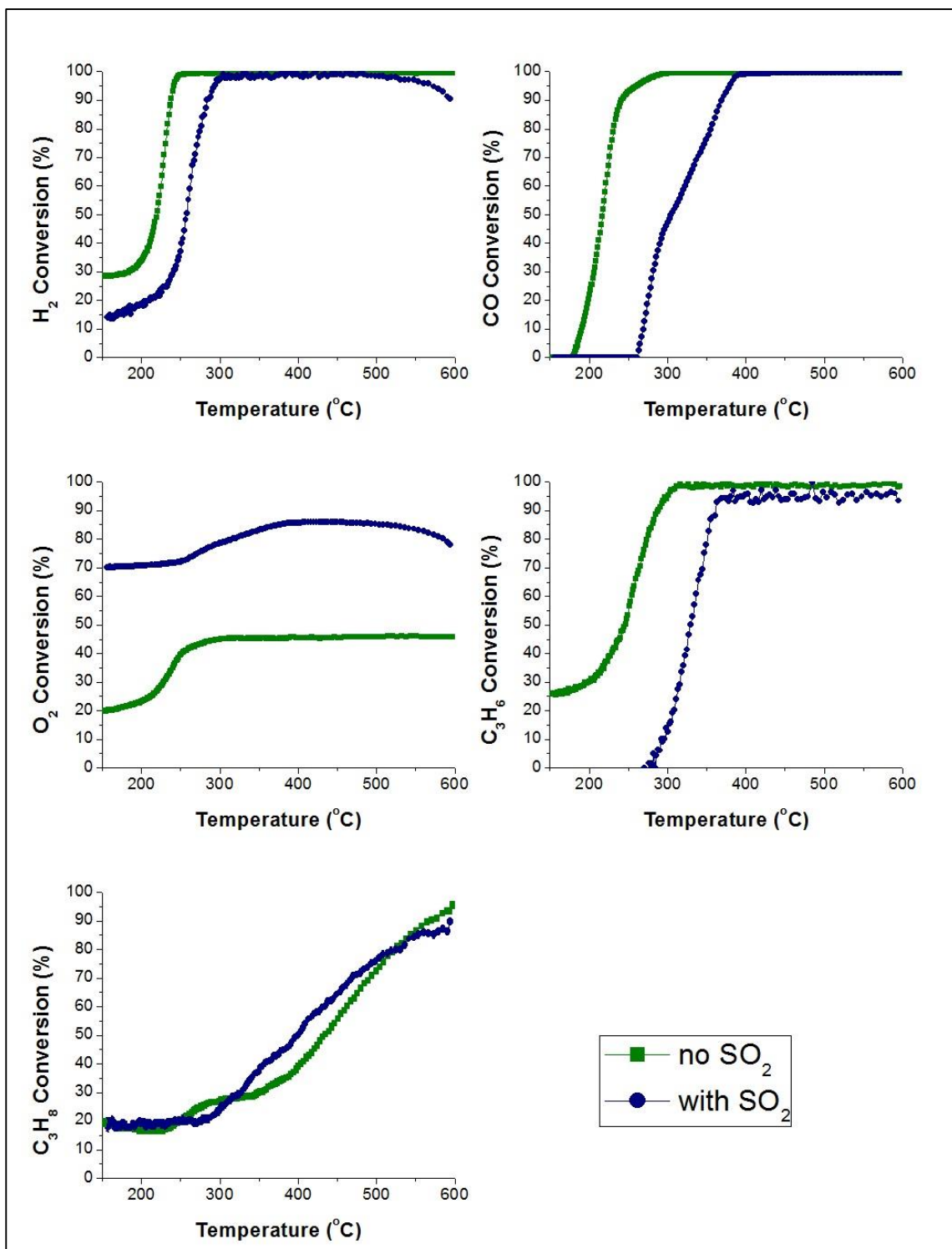


Figure 68 Conversion versus temperature curves of SC3-M2 in SO₂ exposure

APPENDIX F

X-RAY DIFFRACTOGRAMS & PARTICLE SIZE ESTIMIZATION

F1. XRD Patterns of the Catalysts Synthesized via Impregnation Method

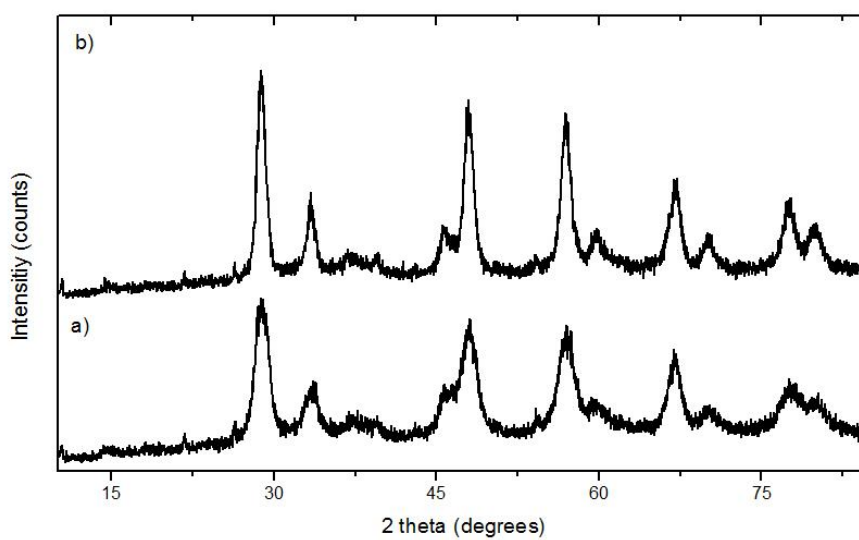


Figure 69 XRD of a) Fresh IMP1 powder b) IMP1 powder aged at 900°C

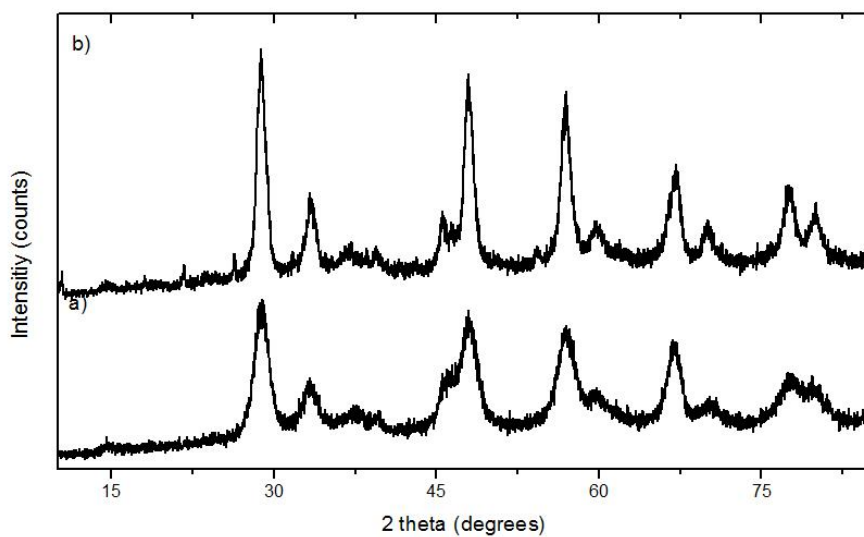


Figure 70 XRD of a) Fresh IMP2 powder b) IMP2 powder aged at 900°C

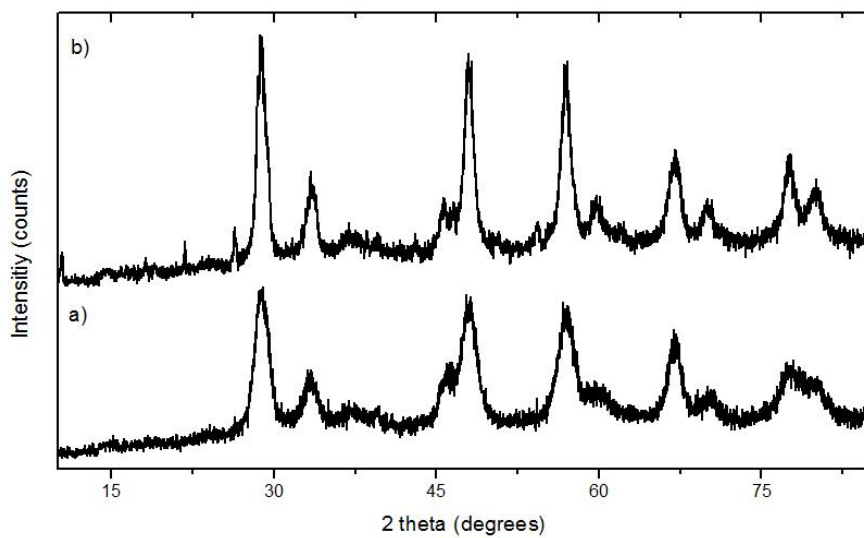


Figure 71 XRD of a) Fresh IMP3 powder b) IMP3 powder aged at 900°C

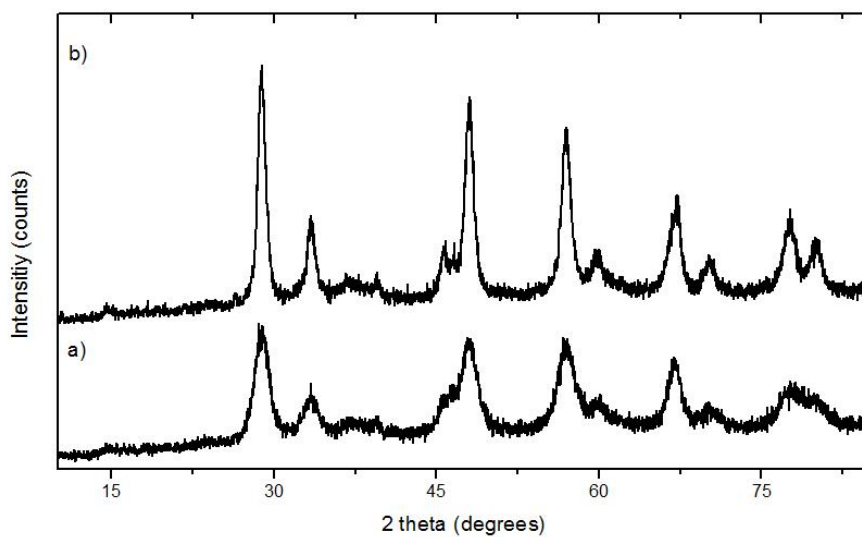


Figure 72 XRD of a) Fresh IMP4 powder b) IMP4 powder aged at 900°C

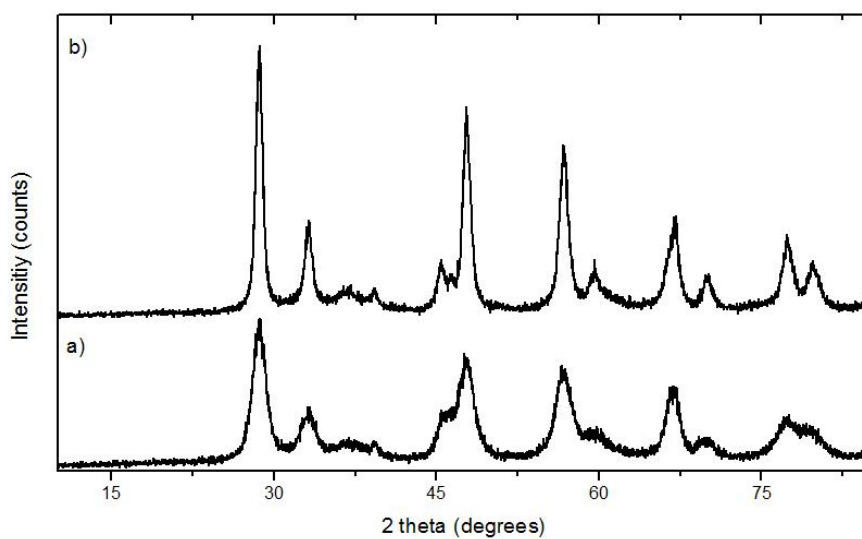


Figure 73 XRD of a) Fresh IMP5 powder b) IMP5 powder aged at 900°C

F2. XRD Patterns of the Catalysts Synthesized via Solution Combustion Method

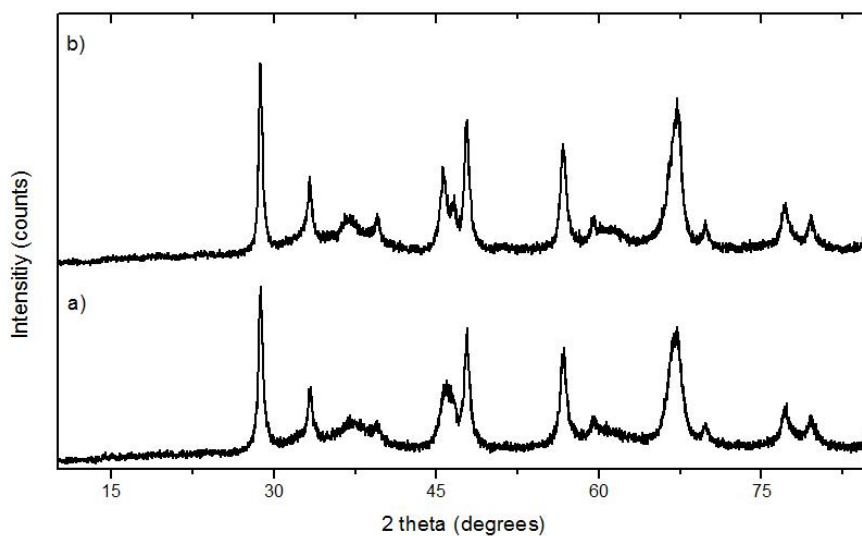


Figure 74 XRD of a) Fresh SC1 powder b) SC1 powder aged at 900°C

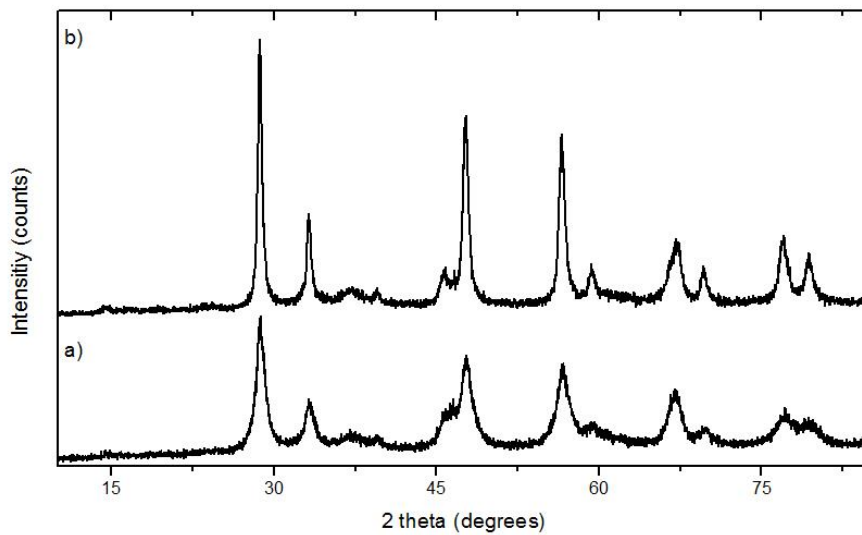


Figure 75 XRD of a) Fresh SC2 powder b) SC2 powder aged at 900°C

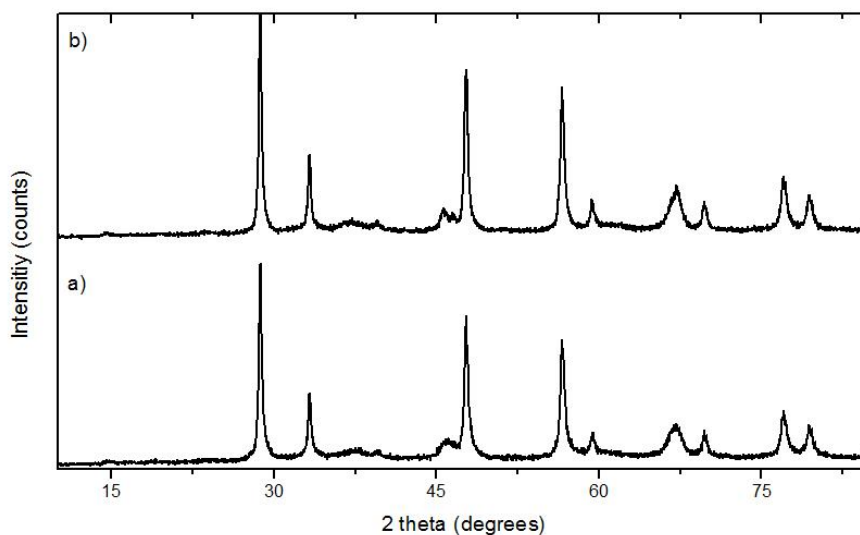


Figure 76 XRD of a) Fresh SC3 powder b) SC3 powder aged at 900°C

F3. Particle Size Estimation Using XRD

Particle sizes of the catalyst samples were estimated using Scherrer equation (Cullity & Stock, 2001) below:

$$t = \frac{0.9 \times \lambda}{B \times \cos(\theta_B)} \quad (\text{F.1})$$

where

t : particle size in nm

λ : wavelength in nm (0.154 nm for Cu K α X-ray)

B : full width of the peak at half of maximum Bragg peak in radians

θ_B : Bragg angle

Using the highest peak ($2\theta_B$: 28.63) in Figure 41 particle size is calculated in the following steps:

$$\theta_1: 27.98$$

$$\theta_2: 29.15$$

$$B = \frac{(29.15 - 27.98) \times 3.14}{180} = 0.2041 \text{ radians}$$

$$\cos(\theta_B) = \cos \left[\frac{14.32 \times 3.14}{180} \right] = 0.969$$

$$t = \frac{0.9 \times 0.154}{0.2041 \times 0.969} = 7.01 \text{ nm}$$